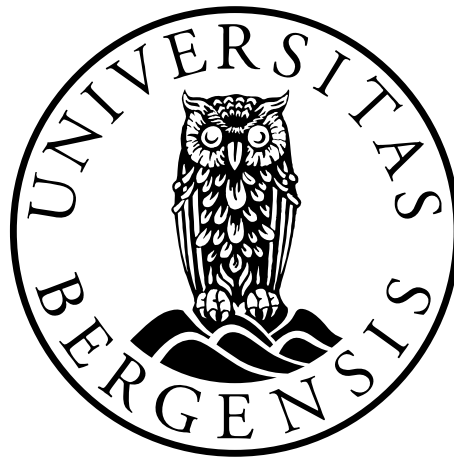# The Role of Axl in Cancer and Stem Cell Plasticity: *in vivo* Lineage Tracing and Imaging Mass Cytometry Analysis

Austin James Rayford

This thesis is submitted in partial fulfilment of the requirements for the degree of Master in Biomedical Sciences

Department of Biomedicine

University of Bergen, Norway

September 2019

Acknowledgements

"þetta reddast…" -Icelandic saying

roughly translated: "Things always have a way of working out in the end."

First and foremost, I'd like to thank my supervisor Jim Lorens for single-handedly convincing me to quit my job and move to Norway. It's been a wild ride and I couldn't have done it without his support.

I'd also like to thank my cosupervisor Agnete Engelsen for stepping up right when my morale was the lowest and getting me fired up about research again. Her countless hours of support along with Maria Kolnes Lie were essential in the writing process.

I sincerely appreciate my other colleagues in the lab: Sturla, Seb, Kjersti, Stacey, Sushil, and Endre from Lorens' group, Dr. A Hoel and Dr. F Hoel, and the whole FLOW core crew

Finally, I'd like to thank my friends both in Bergen and the States as well as my family for providing me with such a great support system!

Table of Contents

Abbreviations

abbreviation	term
AML	acute myeloid leukemia
CAR-T-cells	chimeric antigen receptors T-cells
CTL	cytotoxic T lymphcytes
CTLA4	cytotoxic T-Lymphocyte-associated antigen 4
CyTOF	time-of-flight mass cytometry
DCs	dendritic cells
ECM	Extracellular matrix
EGFR	epidermal growth factor receptor
EMT	epithelial-to-mesenchymal transition
ER	estrogen receptor
ES	embryonic stem cells
FACS	fluorescence-activated cell sorting
FDG	fluorescein di-β-galactopyranoside
FFPE	formalin fixed parafin embedded
FOXP3	forkhead box P3
GAS6	growth arrest-specific 6
GFP	green fluorescent protein
GGCX	γ-glutamyl carboxylase
GLA-domain	γ-carboxylglutamic acid-rich domain
HET	heterozygous, *Axltm1Dgen*(LacZ)+/+
HMEC	human mammary epithelial cell
IMC	Imaging Mass Cytometry
KO	knockout, or *Axltm1Dgen*(LacZ)+/+

LEP	luminal epithelial progenitor
LGR5	leucine-rich repeat-containing G-protein coupled receptor 5
MaSC	mammary stem cells
MEP	myoepithelial progenitor
NSCLC	non-small cell lung cancer
NCS	Neighboring channel spillover
PBS	phosphate-buffered saline
PD1	programmed death receptor 1
PDL1	programmed death receptor ligand 1
PtdSer	phosphatidylserine
ROI	region of interest
RTK	receptor tyrosine kinase
SHGB domain	sex hormone-binding globulin
SMC	suspension mass cytometry
TAM	TYRO3, AXL, MERTK family of RTKs
TCR	T cell receptor
TEBs	terminal end buds
TM	transmembrane domain
TMA	tumor microenvironment
TNBC	triple-negative breast cancer
tSNE	t-distributed stochastic neighbor embedding, specifically the Barnes-Hut implementation known as BH-SNE
WT	wild type
β-gal	β-galactosidase

Summary

Axl receptor tyrosine kinase is correlated with epithelial-mesenchymal plasticity, immune evasion, metastatic potential and therapeutic resistance. However, its mechanism of action and function in normal epithelial cells is unknown. Recent results suggest that Axl is expressed in rare mammary and lung epithelial stem cells. In order to study the role of Axl in epithelial stem cells we conceived and generated a genetically-engineered Axl lineage-tracing mouse model in consultation with an external company.

The primary objective of the study is to elucidate the role of Axl in normal epithelial stem and progenitor cells and determine how this function is coopted during malignant transformation. To this end, we planned a lineage tracing study with the novel strain that could determine whether Axl was a *bona fide* multipotent stem cell marker in mammary epithelia or induces dedifferentiation in committed progenitor cells. In preparation for this study, fluorescence-based detection approaches for measuring Axl-positive stem cells from the lineage tracing strain were evaluated. During these experiments, the strain was extensively genotyped and found to not carry the secondary lineage reporter gene due to a strategical error made by said company. In addition to standard approaches, an imaging mass cytometry (IMC) panel of metal conjugated antibodies was developed for high dimensional spatio-temporal and phenotypic tissue analysis. By incorporating many previously reported unipotent and multipotent stem cell markers into a single IMC panel, a more definitive stem cell hierarchy and mechanism of organ remodeling can be derived in relation to Axl signaling.

1. Introduction

1.1 Cancer: Prevalence, Origins and Characteristics

As society continues to advance in terms of both socioeconomic development and global health, the incidence and mortality of cancer are rapidly growing worldwide. In countries at both ends of the economic spectrum, factors that correlate with reduced prevalence of other causes of death, such as increased life expectancy, also correlate with increased cancer incidence. Preventative treatment of infectious diseases in third-world countries has resulted in a shift towards non-infectious causes of death [1]. In developed countries, increasing levels of health awareness combined with advances in treatment and prevention have significantly reduced the risk of death from cardiovascular disease; in the United States, cancer is predicted to become the leading cause of death within the next five years [2], and has already become the leading cause of death in Norway [3]. Globally, cancer is currently the first or second leading cause of premature mortality in over half of all countries, and is expected to become the overall leading cause of death within the 21st century [4]. Concerning cancer type, the most common cancer in females is breast cancer, while lung cancer is the most common cancer in males and is responsible for the highest number of cancer-related deaths when both sexes are combined (Figure 1.1) [5].
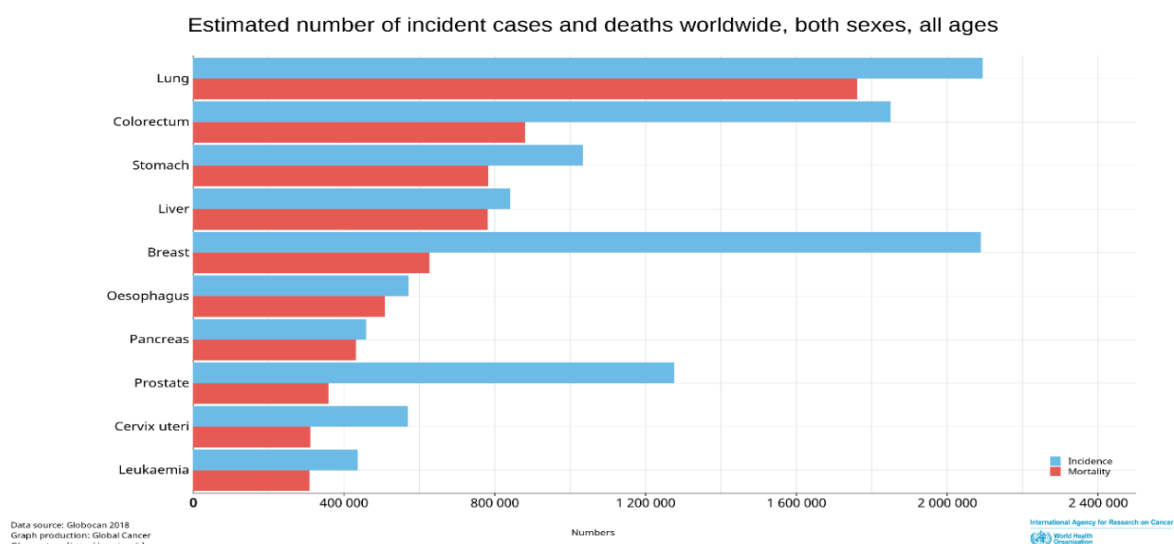

Figure 1.1: Age-standardized cancer incidence and mortalities worldwide in 2018 estimated by WHO. Both sexes and all ages are included. Data source: Globocan 2018. Graph produced by: Global Cancer Observatory (http://gco.iarc.fr/) [5]

While the risk factors for other diseases can be mitigated, the primary risk factor for cancer is inherently unavoidable; although environmental and lifestyle factors such as smoking, obesity, and chronic infections as well as heritable gene mutations can significantly contribute to the lifetime risk of some types of cancer, the majority (65%) of variation in the lifetime risk of being diagnosed with different cancers can be explained by the number of stem cell divisions within the particular tissue in which it arises, which invariably accumulate with age [6]. This reflects the widely accepted notion that cancer is caused by the accumulation of genetic and epigenetic alterations in cells, the majority of which arise from the endogenous error rate in DNA replication during cell division [7]. The cellular characteristics enabled by these genetic alterations can be categorized based on six hallmark capabilities of all cancers proposed by Hanahan and Weinberg in 2000: sustaining proliferative signaling, evading growth suppressors, activating invasion and metastasis, enabling replicative immortality, inducing angiogenesis (blood vessel growth), and resisting cell death [8]. In 2011, two additional emerging hallmarks (not yet observed in all cancers): deregulating cellular energetics and avoiding immune destruction, and two enabling characteristics (not directly acquired by cancer cells but present in cancer-prone tissue environments): tumor-promoting inflammation and genome instability, were proposed by the same authors (Figure 1.2B) [9]. Taken together, these qualities roughly encapsulate the barriers that cancer cells must overcome to reach malignancy. However, the process by which cancer cells acquire and exhibit these traits varies both within and between cancer types. As such, cancer should be considered as a heterogenous collection of different diseases rather than a single disease.

1.2 Cancer Development and the Tumor Microenvironment

Despite the heterogeneity of the underlying molecular mechanisms of tumorigenesis, most solid tumors (namely carcinomas, which are cancers derived from epithelial cells) develop in a similar fashion, which is depicted in Figure 1.2.
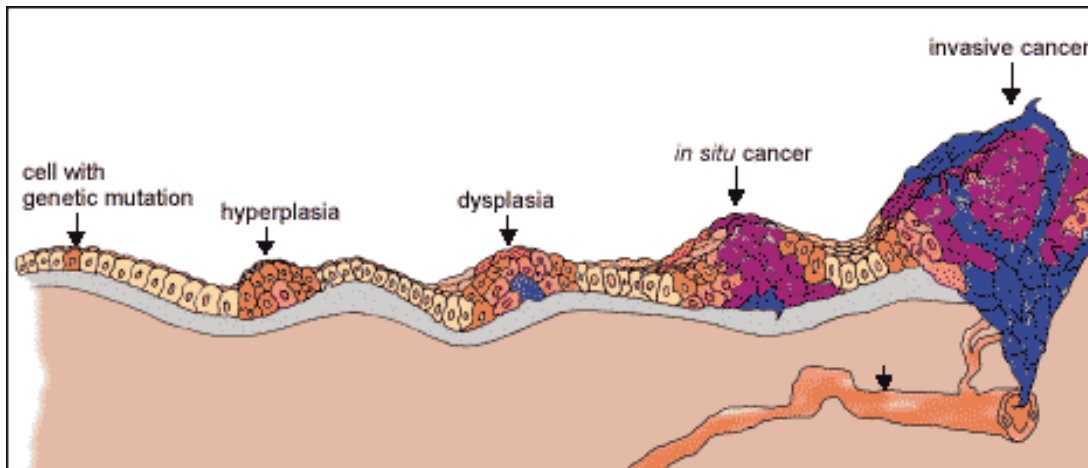
Figure 1.2: Stages of tumor development. A single cell gains a mutation that causes it to abnormally divide. The cell and its progeny continue to divide faster than the surrounding cells (hyperplasia) until one of these cells acquires another mutation that causes it to divide even more rapidly (dysplasia). The gain of additional hallmarks from genetic or epigenetic alterations of cells in the dysplasia result in a cancer, which is described as *in situ* so long as it is contained within its tissue of origin. The *in situ* cancer can modulate its surrounding microenvironment and acquire additional mutations in order to recruit blood vessels, invade neighboring tissues (becoming malignant), and shed cells into the lymph or blood which can establish metastases elsewhere in body. Taken from [10].

Human tumors develop over years and decades. As a dormant abnormal cell develops into an *in situ* cancer, the rate of growth increases exponentially between each stage. In addition to intracellular changes within the cancer cells themselves, they must also enact changes in the surrounding tissue environment, which is normally tumor suppressive in that it maintains differentiated cell states and tissue boundaries. Once altered, the complex network of normal (non-mutated) cells, extracellular matrix (ECM) proteins, and circulatory and lymphatic structures becomes a supportive "niche" referred to as the tumor microenvironment (Figure 1.3). Cancer cells participate in a bidirectional exchange of signaling factors with the tumor microenvironment, coined *dynamic reciprocity* by M. Bissell, that drives the hallmarks of cancer, including angiogenesis (recruitment of blood vessels), sustained growth signaling (by secretion of growth factors, hormones and cytokines), invasion and metastasis (through degradation of ECM and chemotactic signaling), and immune evasion (by secretion of immunosuppressive cytokines), as well as therapy response by modulating the uptake and availability of cancer drugs [11].
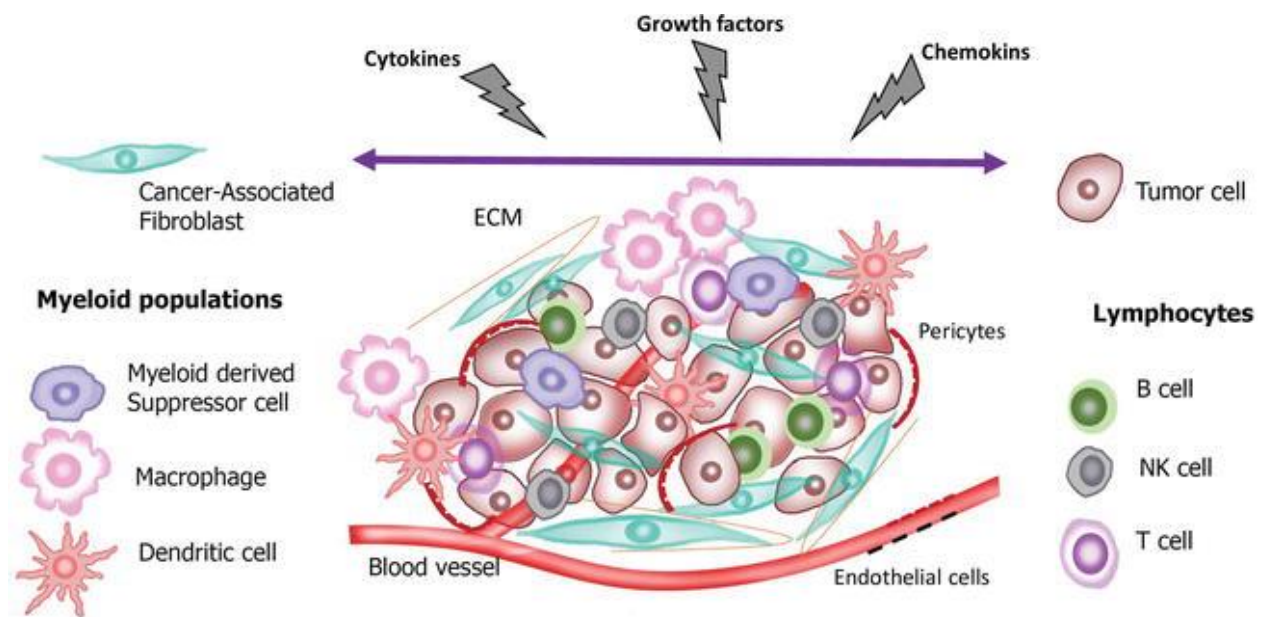
Figure 1.3: The tumor microenvironment. The various constituents include extracellular matrix (ECM), stromal cells (cancer-associated fibroblasts, endothelial cells and pericytes) and immune and inflammatory cells (T, B, and natural killer 'NK' lymphocytes, dendritic cells, macrophages and myeloid-derived suppressor cells). Taken from [11].

1.3 The evolution of cancer therapy

The increasing pace of technological development and modern biomedical research has spurned a plethora of new cancer therapies, although traditional treatment modalities still comprise the backbone of current multimodal treatment regimens for many cancer types. A brief chronological overview of these therapies and their relationship to tumor biology is given below.

Surgery

Up until only a century ago, the only treatment option for cancer was surgery. Typically, these surgeries were radical in nature and sought to completely eradicate all traces of tumors to prevent relapse. However, tumors were often already too advanced upon diagnosis for surgery to be curative. Surgery is a first-line treatment for many cancers and is effective in either debulking or completely removing cancerous tissue, particularly when detected at an early stage [12].

Radiotherapy

Marie and Pierre Curie first discovered that X-ray radiation was harmful to cells and suggested its use in the treatment of tumors in 1899 [13]. Ever since, targeted radiation therapy has proved to be an effective treatment for shrinking or eradicating solid tumors before, in place

of, or after surgery. Toxicity to adjacent normal tissue limits the dose of radiation that can be safely administered, and the resulting tissue inflammation elicits both an anti-tumor immune response that can be limited by radioresistant suppressor cells and a tumor-promoting wound healing response from cells in the tumor microevironment [14].

Chemotherapy

The accidental discovery that mustard gas specifically targets rapidly dividing cells in the bone marrow after the Second World War beckoned in the era of chemotherapeutics [15]; cytotoxic agents that target cancer cells based on their rapid proliferation. These agents cause DNA damage (by alkylating agents), inhibition of DNA, RNA or protein synthesis (via incorporation of antimetabolites or targeting by antibiotics), inhibition of mitosis (by fungi-derived antimitotic compounds), or iron deficiency (by iron chelators), and are still widely used as first-line treatments for lymphomas, leukemias, and inoperable, advanced or metastatic solid tumors [16]. A wide range of chemotherapy combinations have been shown to target a broader range of cancer cells at lower doses than single chemotherapeutics while also increasing the window in which the treatment is effective before resistance develops. Chemotherapy is also particularly useful as a neo-adjuvant or adjuvant therapy (therapy administered before or after primary therapy to debulk tumors prior to surgery or reduce the risk of recurrence, respectively).

Targeted Therapy

Significant strides in the field of molecular biology at the end of the 20th century enabled the discovery of the soluble signaling molecules and associated downstream intracellular signaling pathways responsible for many of the hallmarks of cancer. Synthetic and antibody-based molecules targeting components of these pathways that are dysregulated in cancer cells marked a revolution in cancer therapy. Often cancer cells are "addicted" to these aberrantly activated pathways, relying on them for sustained growth and proliferation, and making them ideal therapeutic targets. Signal transduction can be upregulated by overexpression of the receptor, activating mutations in the receptor or its downstream signaling proteins, or inactivating mutations in negative feedback regulators of a given pathway.

In 1970, tamoxifen became the first FDA-approved targeted therapy. Tamoxifen selectively binds the estrogen receptor (ER), which prevents it from binding estrogen and acting as a proliferation-inducing transcription factor in ER+ breast cancer cells. This paved the way for a class of drugs targeting hormone receptors in both breast and prostate cancer [17]. Receptor

tyrosine kinases (RTKs) are a large family of transmembrane signaling molecules that are activated by dimerization and autophosphorylation upon ligand binding, and regulate many important cellular processes including migration, proliferation, dedifferentiation, and survival through the recruitment of intracellular signaling cascade proteins to their active sites [18]. Although there is significant crosstalk between the signaling pathways activated by these receptors, monoclonal antibodies and small-molecule inhibitors targeting specific signaling proteins have succeeded in clinical trials for a broad range of cancers, particularly in locally advanced or metastatic stages where surgery, chemotherapy, and/or radiation had failed (Figure 1.4). Importantly, the clinical efficacy of many of these treatments could only be realized when patients were stratified into treatment groups based on molecular testing of their cancer status (companion diagnostics), such as fluorescent in-situ hybridization (FISH) to select HER2+ breast cancer patients to receive trastuzumab treatment, endothelial growth factor receptor (EGFR) mutation assays to select non-small cell lung cancer (NSCLC) patients for erlotinib treatment and BRAF-V600E mutation assays to select melanoma patients for dabrafenib treatment [17]. For all of the aforementioned drugs, the efficacy of the therapies, although initially significant, is eventually thwarted by various resistance mechanisms, some of which have yet to be fully understood. In NSCLC, EGFR inhibitor resistance occurs by several mechanisms; secondary mutations in the EGFR gene, which has prompted second- and third-generation EGFR inhibitors to be developed; activation of alternative survival pathways, which has prompted the use of other targeted therapies; and reprogramming of surviving cells from a proliferative to quiescent state, facilitated by epithelial-to-mesenchymal transition (EMT).
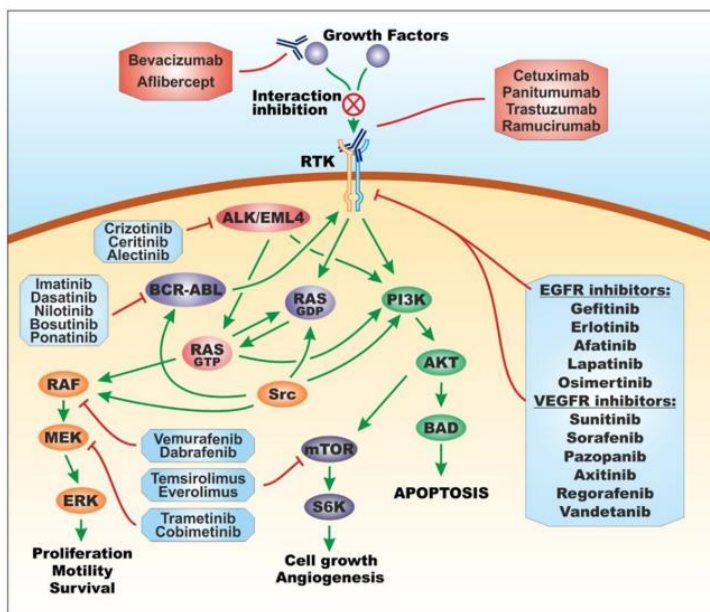

Figure 1.4: Targeted therapies against growth factor signaling cascades in cancer. Includes both monoclonal antibodies and small molecule inhibitors. Taken from [16].

Cancer immunotherapy

In the past decade, the ability of the host immune response to eradicate cancer cells has entered the spotlight of cancer therapy. Due the vast number of genetic and epigenetic changes in cancer cells that result in the presentation of abnormal protein fragments (neoantigens) on their cell surface, they can be recognized and destroyed by host immune cells (anti-tumor immunity). In particular, cytotoxic T lymphcytes (CTLs) initiate a lethal granzyme-mediated attack on cells when a neoantigen binds its T cell receptor (TCR)**.** However, there are several immune checkpoint signaling pathways that mitigate immune destruction of normal tissue which are upregulated by cancer cells in order to thwart the recruitment, activation, and attack of CTLs. By blocking these inhibitory checkpoint molecules with selective antibodies, anti-tumor immunity can be unleashed on neoantigen-expressing cancer cells.

The first FDA-approved immune checkpoint inhibitor, ipilimumab, which was approved in 2010 for advanced melanoma and targets cytotoxic T-Lymphocyte-associated antigen 4 (CTLA4), an inhibitor of CTL activation. The success of the drug was only acheived when administered with multiple doses of a cancer vaccine (melanoma-specifc gp100) that promoted an endogenous antitumor immune response particularly in patients whose tumors were not inflamed before treatment [19]. Following the success of this treatment, antibodies targeting the immune-inhibitory programmed death receptor 1 (PD1) and its ligand (PDL1), which are expressed by various immune cells including CTLs and cancer cells, respectively, were approved for various indications including melanoma, NSCLC, triple-negative breast cancer (TNBC), and gastric, colon, kidney and liver cancers [20]. An alternative approach in which T cells are engineered to express artificial chimeric antigen receptors (CARs) that target specific tumor neoantigens has also shown considerable success in the treatment of hematological cancers [21]. Combined, over 2,000 immuno-oncology agents are currently being tested or used in the clinic, including a plethora of combinations between immune checkpoint modulators, cancer vaccines, CAR-T cell therapy, targeted therapy, chemotherapy, and radiotherapy [21]. A major challenge to the success of these treatments is the identification and stratification of patients whose tumors either suppress, exclude, or completely lack infiltrating immune cells, and the treatment of these patients with existing or novel therapies that alter the tumor microevironment in a way that reverses these phenotypes [21].

AXL receptor tyrosine kinase

In the context of targeted therapy resistance and immuno-oncology, the AXL receptor tyrosine kinase (RTK) has emerged as a promising new target to enhance the efficacies of these treatments. AXL was initially identified in 1991 as part of the TYRO3, AXL, MERTK (TAM) family of RTKs, the last family of RTKs to be discovered [22]. Like many RTKs, the structure of the TAM family proteins consists of an extracellular immunoglobulin-1 (Ig1) and Ig2 binding domain, followed by two fibronectin type III repeats (FN1/2), a transmembrane (TM) domain, and an intracellular tyrosine kinase domain (Figure 1.5A). Although AXL activates similar downstream signaling pathways as the RTKs in conventional targeted therapy (Figure 1.4), several properties of AXL differentiate it from other cancer-associated RTKs and its TAM family members. First, the two ligands of the TAM family, growth arrest-specific 6 (GAS6) and protein S (PROS1), contain a γ-carboxylglutamic acid-rich (GLA) domain, and EGF and sex hormone-binding globulin (SHGB) domains (Figure 1.5A). The GLA domain, when carboxylated by vitamin K-dependent γ-glutamyl carboxylase (GGCX), binds phosphatidylserine (PtdSer) in a calcium-dependent manner. PtdSer is a ubiquitous phospholipid membrane component which is normally actively sequestered in inner leaflet of the plasma membrane but is exposed on apoptotic cells and their resulting vesicles, stressed cells, aggregating platelets and signaling exosomes [23]. PROS1 only binds TYRO3 and MERTK, while GAS6 has the highest affinity for AXL (mainly at the Ig1 site) and evidence suggests that AXL is consituitively bound to GAS6 as a heterodimer *in vivo* [24]. Thus, AXL/GAS6 serves as a unique sensor for PtdSer-presenting membranes, unlike other RTKs which respond directly to their ligands, and is robustly activated by receptor clustering when PtdSer is localized in high concentrations, namely on apoptotic vesicles (Figure 1.5B). This clustering effect has a significant impact on the strength and duration of the signaling input, due to the stability of the multimeric PtdSer/GAS6/AXL complex and the spatial exclusion of inhibitory phosphatases that otherwise limit the activation of phosphotyrosine signal transduction docking sites [25].
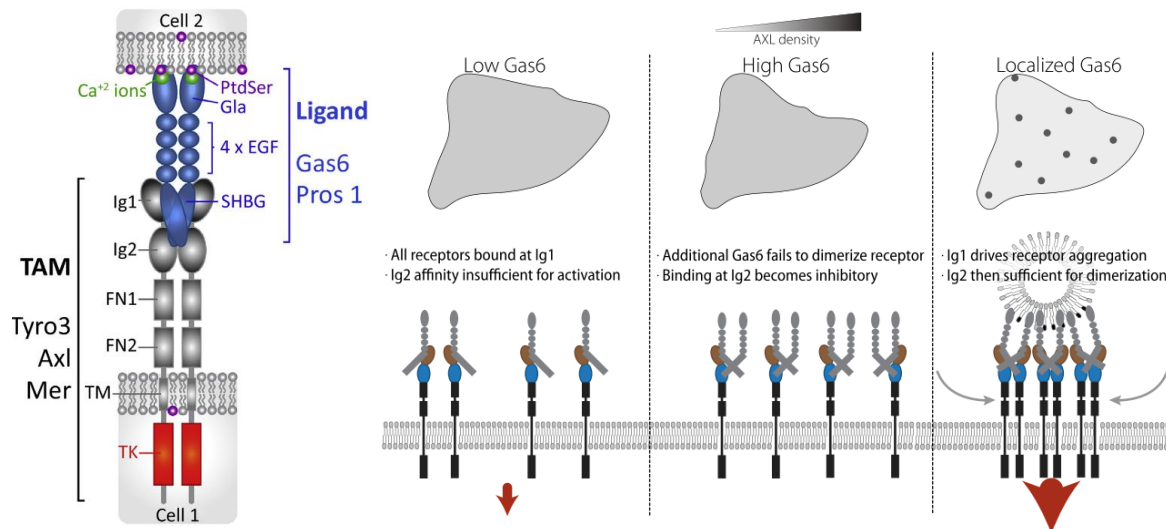
Figure 1.5: Schematic of TAM receptor/ligand complex (A) and Model of GAS6/AXL clustering and activation (B). (A) The TK domains of the TAMR/Gas6 tetramer are strongly activated when GAS6 binds PtdSer presented on cell membranes. (B) AXL signaling activation is not correlated with the concentration of its ligand GAS6, but is robustly activated when Gas6 is localized to PS-rich membrane surfaces. (A) taken from [26] and (B) taken from [24].

Second, AXL mutations are rarely detected in cancers and it is not considered an oncogenic driver, unlike most targeted RTKs. However, its (over)expression in many human cancers is associated with poor prognosis, metastasis, and therapy resistance [27]. This can be attributed to the cellular characteristics granted by AXL signaling in epithelial cells being more related to plasticity (the ability of cells to reversibly alter their phenotype and associated epigenetic and proteomic composition) and quiescence (the ability of cells to temporarily enter a non-replicative, long-lived state), which manifest later in the course of cancer progression and treatment relative to the oncogenic signaling aberrations that typically take place during tumor development. Additionally, the strength of the signaling stimulus from AXL-GAS6-PtdSer clustering, particularly in the context of therapy-induced cell death where large numbers of apoptotic bodies are present, means that even ectopic expression of AXL in surviving tumor cells is likely sufficient to transform some of them to a resistant and/or invasive state [28].

Lastly, GAS6/AXL is also employed by a variety of immune cells as a sensor of cell stress and apoptotic debris, and consistently acts as an immunosuppressive modulator of antitumor immunity; notably, GAS6/AXL has been shown to enhance the suppressive activity of regulatory T cells by upregulating forkhead box P3 (FOXP3) and CTLA4 expression [29], while AXL was found to be upregulated in cytokine-antagonized dendritic cells (DCs) and act an essential negative feedback regulator of toll-like receptor-mediated inflammatory responses [30]. Because of its dual function in immunosuppression in the tumor microenvironment and

therapy resistance, targeting AXL in combination with chemotherapy, targeted therapy and immune checkpoint inhibitors is a novel and promising strategy to increase their efficacy (Figure 1.6).
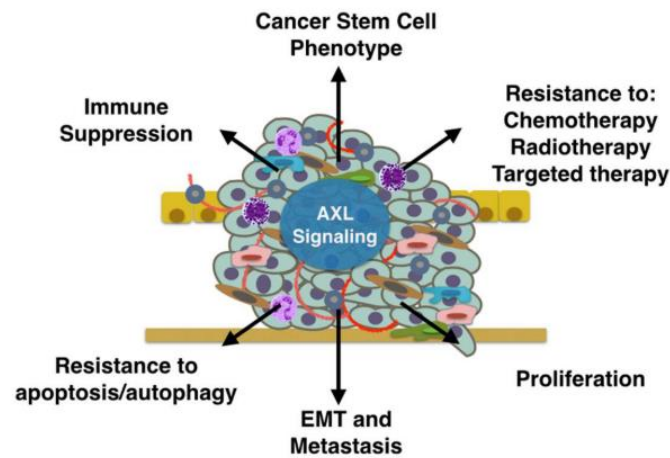
Figure 1.6: Effect of Axl signaling in both the tumor and its microenvironment. Taken from [31].

As such, several AXL-targeting therapeutics have emerged and are in various phases of clinical development. The most noteworthy of these, the small molecule tyrosine kinase inhibitor Bemcentinib, is currently in phase 2 clinical trials for NSCLC (in combination with anti-PD1, anti-EGFR, or chemotherapy), TNBC (in combination with anti-PD-1), melanoma (in combination with anti-PD1 and chemotherapy), acute myeloid leukemia (AML) and pancreatic cancer (in combination with chemotherapy), and recurrent glioblastoma [32-39].

Although there is a logical explanation for AXL expression in immune cells based on a growing body of research, much less is known about the biological function of AXL signaling in normal tissues, which is pivotal to understanding how carcinoma cells can coopt these mechanisms of plasticity and quiescence to ultimately evade even the most modern cancer therapies.

1.4 AXL and cellular plasticity

In order to contemplate the role of AXL signaling in normal epithelial tissues, one must consider how the characteristics granted by AXL signaling in cancer cells could benefit cells during endogenous physiological processes. All of the AXL-related properties illustrated in Figure 1.6 are also exhibited by a unique and hotly-debated cell type that is present in various forms throughout the body: stem cells.

1.1.1.   Stem cells in development

The general consensus on the definition of a stem cell is that it must fulfill two overarching properties: the ability to self-renew, and the ability of its progeny to differentiate into one, two or multiple restricted lineages or cell types (unipotency, bipotency, or multipotency, respectively). The concept of potency is not novel; we have known for centuries that a single, totipotent zygote gives rise to the roughly 200 somatic cell types postulated to exist in the body [40]. The discovery of receptors, signaling pathways, and transcription factors responsible for lineage differentiation and plasticity during embryonic development has been significantly aided by mouse models, in which knockouts of individual proteins resulting in developmental defects implicated that protein's essential role in morphogenesis. Strikingly, neither *Axl*-null mice nor any combination of TAM receptor knockouts show any developmental defects and only exhibit phenotypes associated with the inability to clear apoptotic cells and reduce inflammation and autoimmunity (mediated by *Axl* and *Mertk* expression in immune cells), decreased blood vessel integrity (mediated by *Axl* expression in vascular smooth muscle cells), and defects in platelet aggregation (mediated by expression of all three TAMRs in platelets) [27]. This knowledge constitutes the vast majority of the accepted physiological roles of AXL, and many research papers often extrapolate from this limited knowledge directly into the prognostic and therapeutic indications of AXL in malignant cells, neglecting that there must be a biological purpose for AXL signaling in adult epithelial tissue even though it is typically only expressed at low levels [31, 41-43].

1.1.2.   Adult stem cells

As an organism develops, multipotent cells with an undecided fate differentiate into specialized lineages with more restricted fates based on spatiotemporal inputs from surrounding cells, growth factors, and ECM components. This can be modeled by Waddington's "epigenetic landscape", in which the gradual acquisition of epigenetic changes guides multipotent cells over the course of many divisions to their specific functions and creates an increasingly steep epigenetic barrier between differentiated cells of different lineages [44]. However, a small subset of cells in some organs remain fixed at various branching points of this hierarchy throughout adulthood, and serve as "hard-wired" stem cells that repopulate specialized cell types during normal tissue homeostasis and repair. The canonical example is that of hematopoiesis (mature blood cell formation), where progenitor cells have been isolated and characterized at nearly every branching point of the differentiation hierarchy, from unipotent precursor cells, which divide frequently, to rare multipotent

hematopoietic stem cells, which remain in a quiescent state in the bone marrow and divide on average only once every two months [45]. Interestingly, AXL is abundantly expressed in both physiological and malignant hematopoiesis, providing a rationale for its role in AML pathophysiology, therapy resistance and subsequent targeting in combination clinical trials [46]. Other diverse examples of well-characterized stem cells include satellite cells, which lie dormant for years until recruited to regenerate muscle fibers upon damage, and leucine-rich repeat-containing G-protein coupled receptor 5 (LGR5)-expressing intestinal crypt cells, which divide frequently (up to 1,000 divisions per lifetime) to feed the rapid tissue turnover rate of intestinal epithelium [45]. In this case, however, it was shown that quiescent, differentiated +4 crypt cells can dedifferentiate when LGR5+ stem cells are ablated, regaining the LGR5+ multipotent phenotype [47]. This raises the notion that differentiation is not necessarily unidirectional; in conditions such as organ regeneration and remodeling where resident stem cells cannot meet the demands of repopulation, lineage-restricted cells can be reprogrammed to act as facultative stem cells [48]. This reprogramming potential is referred to as cellular plasticity.

1.1.3. Plasticity versus committed progenitors

Two pivotal examples of plasticity-induced dedifferentiation superseding and/or contradicting the established hierarchy of committed stem/progenitor cells can be found in the mammary and lung epithelia. The mammary gland is comprised of two distinct epithelial lineages: luminal and basal. Luminal cells line the interior of the mammary ducts and differentiate into ductal and alveolar cells during pregnancy to secrete water and nutrients, respectively, in the form of milk, while basal cells are highly-elongated and in direct contact with the basement membrane, forming an outer myoepithelial layer around the luminal cells that contracts in order to stimulate secretion and milk flow throughout the ductal tree [49, 50]. During puberty, mammary ducts undergo a massive hormone-induced expansion, where branching terminal end buds (TEBs) penetrate into the underlying mammary mesenchyme (fat pad). Two opposing hypotheses exist concerning the nature of mammary stem cells (MaSCs) and their role in mammary gland remodeling and homeostasis based on evidence from classical mouse model experiments. On one hand, a lineage tracing study independently tracking unipotent basal and luminal progenitors and their progeny *in vivo* demonstrated that each lineage is maintained independently throughout puberty and pregnancy (Figure 1.7A) [50]. On the other hand, *ex vivo* transplantation of putative bipotent basal MaSCs into cleared mammary fat pads

has demonstrated that they can reconstitute the entire dual-lineage structure of the mammary gland (Figure 1.7B). Crucially, our group has shown that Axl serves as a putative bipotent MaSC stem/progenitor marker in mice using the same experimental strategy (Figure 1.7C) [51].
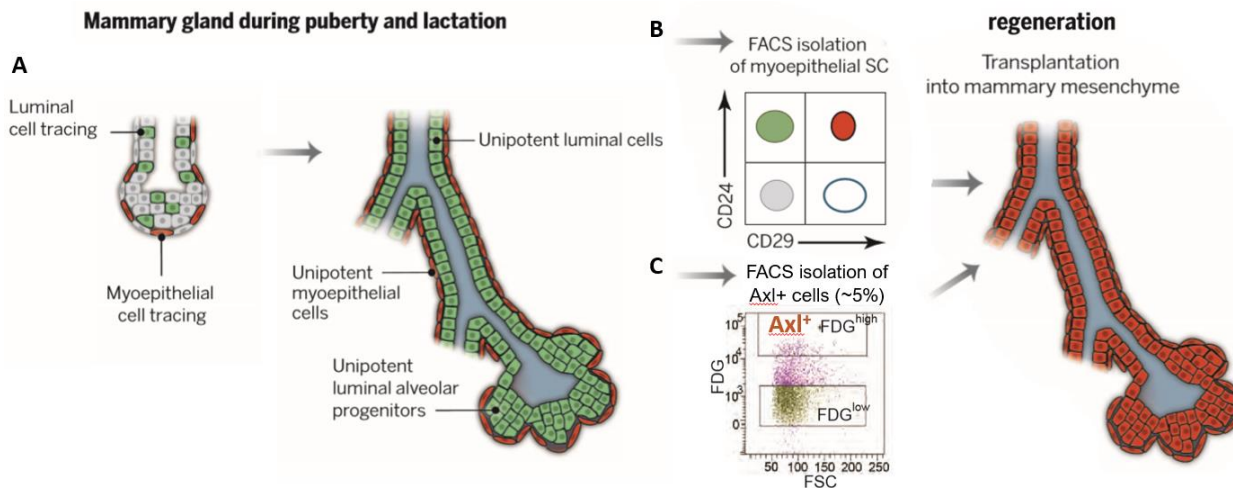
Figure 1.7: Conflicting experiments regarding the nature of mammary stem cells in homeostasis and remodeling. (A) Lineage tracing of unipotent myoepithelial (basal) and luminal progenitors through puberty and lactation suggests they independently maintain their respective lineages. Fluorescence-activated cell sorting (FACS) of putative myoepithelial mammary stem cells based on surrogate marker expression (B) or AXL expression (C) demonstrates their multipotency through their ability to reconstitute the entire mammary gland structure in cleared mammary mesenchyme. FDG: fluorescein di-β-galactopyranoside, a reporter molecule for Axl+ cells in Axl/LacZ heterozygous mice. A and B adapted from [52] and C taken from [51].

One critique of the *ex vivo* reconstitution assay is that it removes cells from their *in situ* niche, which may apply novel environmental pressures not normally encountered *in vivo* that induce dedifferentiation. However, our group has also shown that AXL+ myoepithelial cells are poised at the apex of the human mammary epithelial cell (HMEC) hierarchy *in vivo* based on flow cytometric analysis of isolated primary HMECs stained with markers for AXL and various lineage-specific cell surface receptors (Figure 1.8A) [51]. Additionally, a functional *Axl*-knockout mouse model generated by our group showed significantly reduced ductal branching and morphogenesis and a pro-luminal phenotype compared to wild-type mice [51]. Paradoxically, another group recently reported that *Gas6*-knockout mice showed no impairment of ductal morphogenesis [53]. Returning to Waddington's epigenetic landscape, it is unclear whether AXL+ multipotent cells permanently reside in a specialized niche, arise from dedifferentiation of AXL+ basal cells, or some combination of the two (Figure 1.8B), while the role of AXL signaling in mammary gland remodeling and homeostasis has yet to be determined.

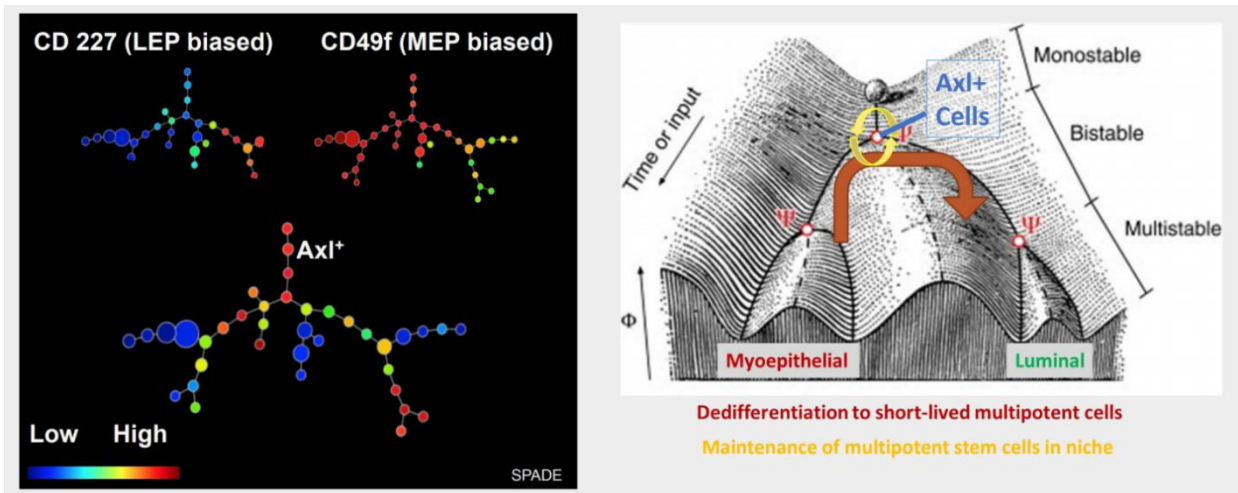**Figure 1.8: AXL in the mammary stem cell hierarchy.** (A) Spanning-tree progression analysis of density-normalized events (SPADE)-generated hierarchical trees from multicolor flow cytometry data of primary HMECs isolated from patient reduction mammoplasty tissue samples and stained with CD326/CD49f/CD227/CD10/Axl markers. Each circle represents a distinct cell subpopulation that is most related to its nearest neighbors and whose size is proportional to the relative number of cells. Relative expression of CD227, a luminal epithelial (LEP) marker, CD49f, a myoepithelial (MEP) marker, or Axl in each subpopulation is shown on a blue to red (low to high expression) scale. Differentiated LEP and MEP cell populations comprise the left and right lineage branches, respectively, while Axl is expressed primarily in the putative bipotent MaSC populations found at the apex of the hierarchical tree. (B) Two possible scenarios for Axl expression in bipotent MaSCs imposed on Waddington's epigenetic landscape. Axl+ cells are either maintained in a niche at the apex of the hierarchy (yellow), arise from dedifferentiation of committed Axl+ myoepithelial cells (red), or some combination of the two. Φ corresponds to the level of epigenetic differentiation and lineage commitment from a multipotent state, while Ψ corresponds to deterministic splits between two cell fates in the hierarchy, and also correlates strikingly well with the branching points in (A). A taken from [51] and B adapted from [44].

In the mammalian lung, cellular plasticity has been observed in both the airway and alveolar epithelia during non-homeostatic conditions. Mucus-producing club cells in the airway ducts serve as bipotent progenitors of their own lineage and that of ciliated cells, which move mucus and particles out of the lung. Quiescent, multipotent basal cells can give rise to all airway lineages in response to tissue damage, but when these cells were experimentally ablated, it was shown that fully mature club cells could actually dedifferentiate into basal stem cells [54]. Similarly, among the two cell types of the alveolar epithelium, type 2 cells, which steadily secrete surfactant to prevent alveolar collapse, were shown under homeostatic conditions to generate both type 2 and type 1 cells, which participate in gas-exchange and form the thin lining of the alveolar sacs. During injury-induced lung regeneration, type 1 cells have also been inversely shown to generate bipotent type 2 stem cells [55]. Although AXL has not been explicitly implicated in either of these dedifferentiation processes thus far, its role in plasticity-induced resistance to anti-EGFR therapy in NSCLC has been clearly demonstrated by our group and others [28, 56], and suggests that AXL may play a role in normal lung epithelial plasticity.

1.5 Current Research Focus

AXL RTK serves as a unique sensor of apoptosis and cell stress and its signaling pathways are clearly employed by both tumor and associated immune cells to thwart various cancer therapies. While the clinical data from targeting AXL in cancer appears promising, it is also important to understand the role of AXL-induced cellular plasticity in normal epithelia by finding and characterizing rare AXL+ cells during normal homeostasis as well as organ remodeling and repair. In our group in particular, in accordance with the clinical trials of bemcentinib in TNBC and NSCLC, we seek to build on our existing evidence that AXL is a *bona fide* MaSC marker and explore the possibility that this is also the case in lung epithelia.

2. Methodological Considerations

In this section, the unique methods employed in the scope of this work are discussed in detail. All standard techniques as well as the detailed protocols of the applications mentioned below can be found in Section 3.

2.1 Mouse Models

Animals can serve as useful model systems to study disease pathology as well as normal physiological processes. Mice are ideal for these studies because they provide an optimal balance between genetic/physiological similarity to humans and ease of maintenance due to their small size and rapid maturation rate. Various disease models in animals use standardized approaches to induce disease via exposure to pathological agents or genetic manipulation. Recent advances in the fields of genetics and genetic engineering have enabled many elegant transgenic systems that can target specific genes in mice. Two such systems utilized in the current work are described below.

2.1.1 Gene targeting by homologous recombination

Insertion or deletion of genetic material can be achieved by homologous recombination in mouse embryonic stem (ES) cells, producing transgenic mice. Homologous recombination is a naturally occurring process that is observed most frequently in meiosis of gamete cells, and is responsible for the randomization of inherited alleles. Human somatic cells contain two distinct copies of their genome per cell (2N), one from each parent. Variations at specific points along the genome are referred to as alleles, and when taken together, comprise the genetic diversity of a given species. When gamete cells divide, chromosome pairs from each parental genome overlap randomly at various matching points, where conserved homologous sequences align with each other and recruit enzymes that break, swap and recombine the ends of the chromosome pairs. When the gamete cells divide again in meiosis, the resulting daughter cells contain a unique 1N genome that does not match that of either parent due to various homologous recombination events. This process also occurs sporadically in normal cells, which can sometimes result in aberrant activation of oncogenic signaling pathways through the generation of fused proteins. By exogenously introducing high concentrations of linearized, double-stranded synthetic DNA constructs containing sequences homologous to

the specific genetic locus of interest, homogenous recombination can be induced in mouse ES cells [57]. Insertion or "knock-in" of genetic material (flanked by homologous sequences) through this process is generally more efficient than deletion, and enables a diverse arsenal of transgenic expression systems when executed correctly.

2.1.2 Axl-LacZ knock-in model

The *Axl* gene consists of 20 exons (protein coding regions), which sequentially code for each domain of the receptor starting at the extracellular ligand binding domain. Inserting the *LacZ* gene, which encodes bacterial β-galactosidase (β-gal), into exon 11 of the mouse *Axl* gene using homologous recombination interrupts normal expression of *Axl*, serving as a functional knockout in homozygous B6.129P2-AXLtm1Dgen/Jmice, hereafter referred to as *Axl-LacZ* mice (Axl-LacZ-KO, Figure 1.9). It also produces functional β-gal under control of the *Axl* promoter, which can be used to detect Axl+ cells in heterozygous *Axl-LacZ/Wt* mice (Axl-LacZ-HET) since they still have a functional copy of *Axl* in the wild-type allele. β-gal+ cells are detected by addition of β-gal substrates; the X-gal enzymatic product can be detected colorimetrically in tissue sections, while addition of fluorescein di-β-galactopyranoside (FDG) produces a fluorescent product measurable by flow cytometry. As mentioned in the introduction, *Axl* knockout mice are viable but have been shown by our group to exhibit reduced cellular plasticity and remodeling in the mammary gland, however a deeper interrogation of this and other epithelial tissue is required to solidify Axl's role in these processes.
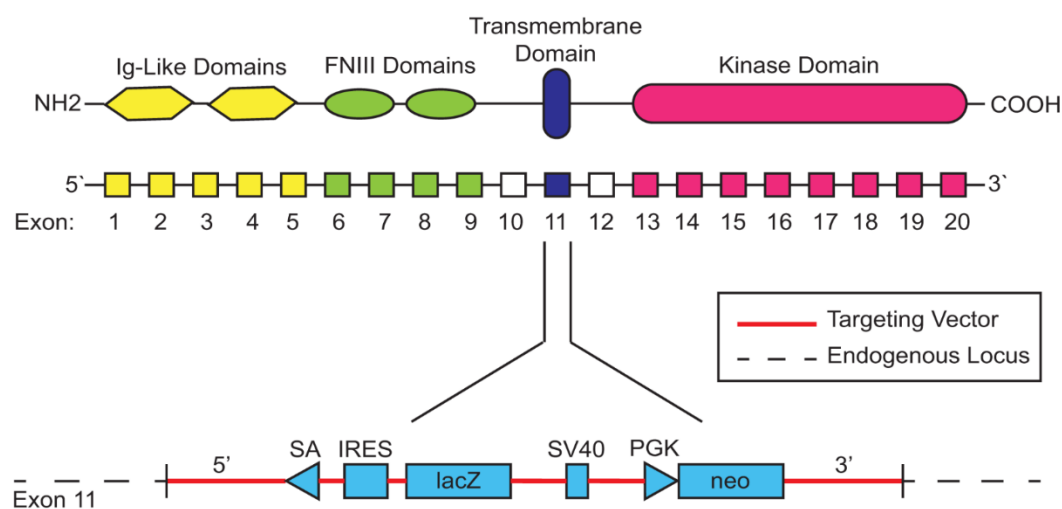

Figure 1.9: **Description of the AXL-targeting mutation in** B6.129P2-AXLtm1Dgen/Jmice. Schematic illustration of theLacZ-Neocassette insertion site in exon 11 of the murine AXL gene, disrupting AXL protein expression. A 5' splice acceptor ensures that the LacZ open reading frame is spliced into the endogenous AXL mRNA under control of the murine AXL promoter.

2.1.3 Axl-Cre lineage tracing model

The ability to permanently mark cells expressing a given marker at a specific timepoint such that their progeny can be detected independently of the original marker expression *in situ* is known as lineage tracing. Although this technique has proven useful in identifying professional, hard-wired stem cells in other organs (Section 1.4.2), numerous lineage tracing mouse models targeting putative MaSC markers have failed to identify a multipotent progenitor population [58]. However, considering our existing evidence from normal mammary epithelia and the propensity of Axl to regulate plasticity in breast carcinomas, we believe that an Axl lineage tracing model could significantly advance our understanding of MaSC plasticity.

The most common inducible lineage tracing approach involves co-expression of an exogenous DNA recombinase with the marker of interest. This recombinase, when expressed as a fusion protein with the binding domain of a hormone receptor, is sequestered in the cytoplasm and can only enter the nucleus when the receptor moiety binds an exogenously administered hormone. Once inside the nucleus, the recombinase binds specific sites and excises a stop codon sequence from a transgenic reporter gene located near a ubiquitously expressed promoter region. (A wide variety of transgenic reporter strains possessing different recombinase-activated or silenced fluorescent reporter proteins are commercially available that can be crossed with the customized lineage-tracing strain.) The stop codon is permanently excised in all cells expressing the marker of interest at the time of hormone administration, meaning that those cells and their progeny will continue to express the reporter protein as long as their lineage persists. A diagram depicting the Axl-Cre lineage tracing system proposed in this study is shown in Figure 2.1.
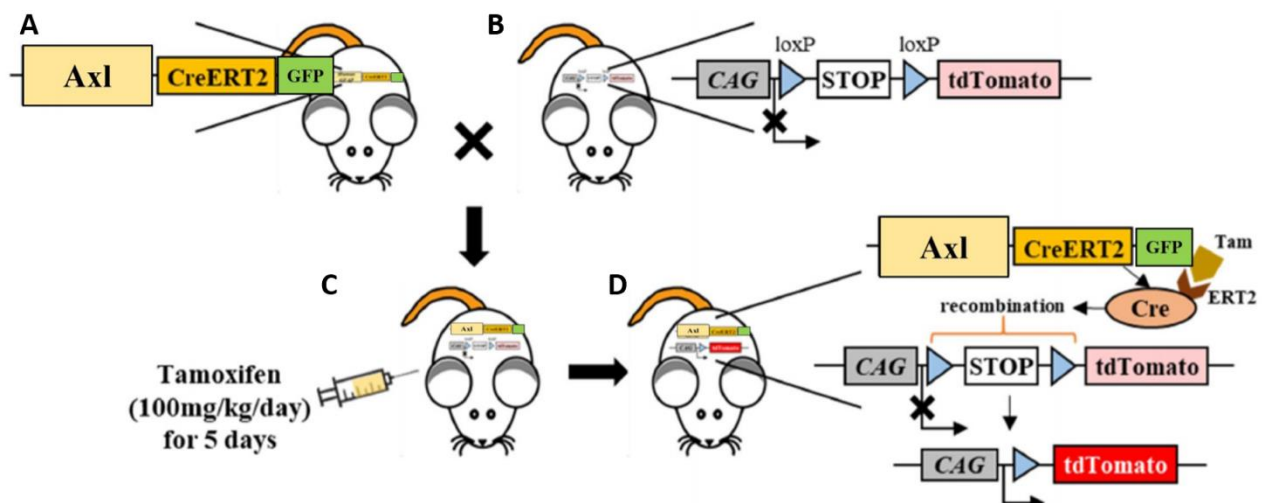
Figure 2.1: *Axl-CreERT2-GFP/Rosa26-CAG-tdTomato lineage tracing system.* A specialized knock-in strain coexpressing Axl, CreERT2 fusion protein, and GFP under control of the Axl promoter (A) is crossed with a reporter strain containing the tdTomato fluorescent protein coding sequence preceded by a loxP-flanked stop codon under control of the ubiquitously-expressed *CAG* protomer at the *Rosa26* locus (B) to produce mice that are homozygous for both transgenic alleles. When these mice are administered tamoxifen (C), it binds the ERT2 receptor domain, allowing the CreERT2 fusion protein to enter the nucleus and excise the stop codon, irreversibly activating tdTomato reporter expression (D). loxP: exogenous recognition sequence for Cre recombinase.

As an added feature, GFP is coexpressed with Axl in this system, allowing us to differentiate Axl-GFP-tdTomato+ cells from their tdTomato+ progeny. However, the expression of three separate proteins from a single promoter requires dedicated genetic engineering using expression elements from viral systems. A schematic of the Axl-CreERT2-GFP knock-in construct is shown in Figure 2.2, and the purpose of each component in the construct is summarized in Table 2.1.
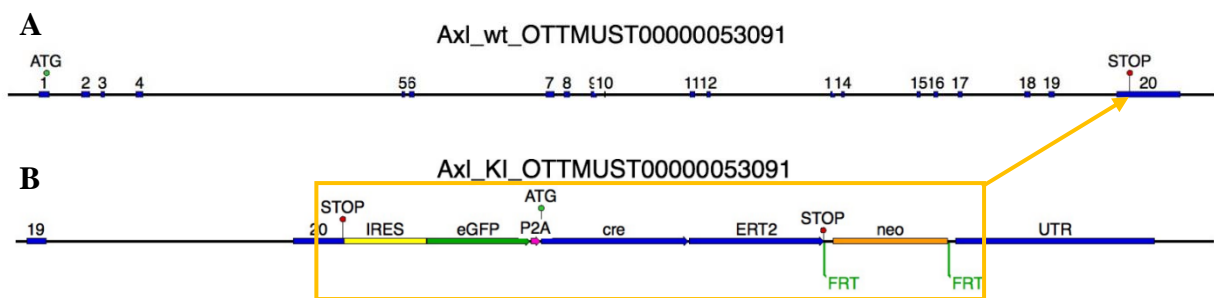
Figure 2.2: (A) Mouse Axl wild-type (Wt) gene. (B) *Axl-CreERT2-EGFP* knock-in (KI) construct. The homologous recombination vector sequence is indicated by the orange box, while the entire length of the segment represents the Axl gene targeted locus after recombination. The arrow indicates the insertion site of the vector on the Axl gene. Blue boxes: exons of the Axl receptor gene; IRES: Internal Ribosome Entry Sequence; cre: Cre recombinase protein coding region; eGFP: enhanced Green Fluorescent Protein coding region; ERT2: Estrogen Receptor Transferase 2 protein coding region; neo: neomycin selection cassette; FRT: Flp Recombinase Target sequence; UTR: untranslated region (of Axl gene).

Table 2.1: List of components in the Axl knock-in construct and their purposes.

Sequence Identifier	Purpose
IRES	Forms secondary mRNA structure that allows ribosome binding and 5'cap-independent expression of additional proteins from a single mRNA [59]
eGFP	Fluorescent protein coexpressed with Axl to distinguish Axl+ cells
P2A	Self-cleaving peptide sequence that allows synthesis of multiple proteins from a single open reading frame [60]
ATG	Start codon (methionine), helps continue translation past P2A sequence
Cre	Recombinase that excises stop codon from transgenic reporter gene locus
ERT2	Domain of estrogen receptor, restricts translocation of fusion proteins to nucleus until binding tamoxifen
FRT	Flp recombinase recognition sequence for excision of neo cassette
Neo	Confers resistance to neomycin to allow for selection of transgenic ES cells

The question of whether Axl+ cells in the mammary epithelium are true MaSCs that differentiate into the unipotent basal and luminal progenitors postulated to maintain their respective lineages throughout adulthood, or are facultative stem-like progenitor cells that dedifferentiate to assist in organ remodeling can be addressed by administering tamoxifen to female Axl lineage tracing mice both before and at the start of puberty (Figure 2.3).
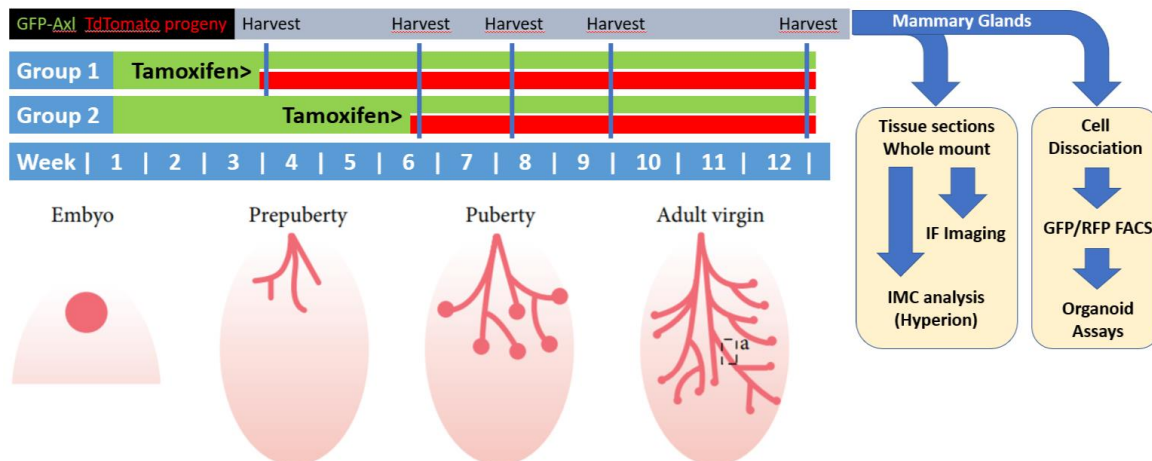
Figure 2.3: Proposed Axl lineage tracing study in mammary development. Two groups of mice are administered tamoxifen to induce tdTomato (RFP) expression of Axl+ MaSC and their progeny at different timepoints relative to the start of puberty. Mammary glands are harvested from sacrificed mice at different timepoints in development and interrogated by multiple complimentary analytical methods. IF, immunofluorescence; IMC, imaging mass cytometry; FACS, fluorescence-activated cell sorting. Mammary development illustration taken from [61].

If Axl+ cells are indeed the precursors of unipotent luminal and basal progenitors and sit at the apex of the mammary stem cell hierarchy, then more tdTomato-expressing cells should be visible in group 1 than in group 2. If Axl+ cells are quiescent and are only recruited as multipotent progenitors during organ remodeling, then the number of tdTomato-expressing cells should be roughly equivalent between the groups. Although standard fluorescence imaging techniques provide the core conclusions from the study, much more insight can be gained by examining these mammary glands using organoid assays and highly multiplexed image analysis, which are described below.

2.1.4 Organoid assays

When studying a subpopulation of cells based on their marker expression *in situ*, clonal heterogeneity can cause these seemingly similar cells to exhibit different traits. In order to examine the behavior of single cells *in vitro*, they can be isolated from tissues, seeded into an ECM-rich gelatin and grown into 3D organoids. This technique provides a succinct advantage over 2D cell culture techniques by allowing cells to coordinate their growth and differentiation in 3D space, which more accurately reflects the *in vivo* environment. Organoids also serve an

ethical purpose by displacing the use of animal models, and are much easier to upscale, monitor, analyze, and treat directly with various biological agents. They often are employed as a powerful complimentary approach in lineage tracing studies, where putative stem cells and their progeny can be isolated and sorted into organoid cultures to observe lineage heterogeneity and multipotency *in vitro*.

2.2 Imaging mass cytometry

Imaging mass cytometry (IMC) is a novel technique that enables highly multiplexed imaging of tissue sections by staining them with heavy metal-conjugated antibodies. It was first conceived by Bodenmiller et al. as a complimentary method to suspension mass cytometry (SMC) a.k.a. time-of-flight mass cytometry (CyTOF) [62], which has already gained significant popularity (particularly in the field of immunology) upon the launch of commercially available mass cytometers from Fluidigm starting in 2009 (originally DVS Sciences, acquired by Fluidigm). While standard immunofluorescence imaging methods can detect a maximum of 5-7 different fluorophore-conjugated antibodies due to overlap of emission spectra, the resolution of mass cytometry currently enables the detection of over 40 heavy metal-conjugated antibodies simultaneously with minimal signal spillover. The platform has the potential to be expanded to up to 100 markers as more isotopes of rare earth metals continue to be isolated and made available for antibody conjugation [62].

2.2.1 Applications in stem cell and cancer research

Observing stem cell plasticity in various states of differentiation or dedifferentiation is an enormous challenge; the use of a single lineage-specific marker per cell type plus one or two candidate stem cell markers and a nuclear stain already pushes the upper limits of standard fluorescence imaging approaches, and is usually insufficient to identify subpopulations of cells within lineages or in a transient state. By incorporating many lineage-specific and previously proposed uni/multipotent progenitor markers as well as the reporter proteins from our lineage tracing model into tissue-specific IMC panels, single cells can be much more accurately mapped to the epigenetic landscape in relation to our proposed model of AXL-induced stem cell plasticity, all within the spatial context of a single tissue section. Furthermore, the addition of signaling markers in the form of phosphotyrosine antibodies can eludicate the intracellular mechanisms of Axl signaling in different contexts. Finally, the ability to simultaneously stain

ECM components and other cell types including immune cells and fibroblasts may reveal novel interactions indicative of a supportive stem cell niche.

All of these metrics are also valuable in the context of the tumor microenvironment, where similar processes are thought to occur as cancer stem cells remodel the surrounding cells and tissue into a supportive niche [63]. In this case, marker emphasis should be shifted from subtyping of epithelial lineages (which are already highly dysregulated in tumors) to subtyping of immune cells and their degree of infiltration, which plays a major role in prognostic outcome and sensitivity to modern therapies.

2.2.2 Sample workflow and technological overiew

The workflow for a typical IMC experiment is shown in Figure 2.4.
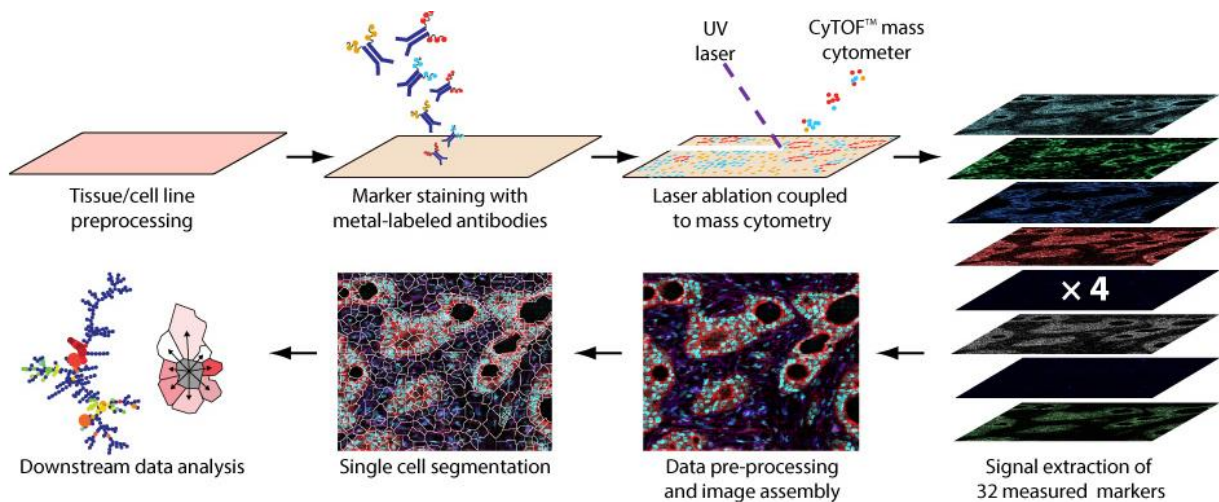
Figure 2.4: Workflow of a typical IMC experiment. At the time of publication of this figure in 2014 (taken from [62]), only 32 metals were available for antibody conjugation, but now up to 40 metals are available.

In a typical IMC experiment, a solid tissue sample (either frozen or FFPE) is sectioned (standard thickness of 5 µm), mounted on glass slides, deparaffinized and rehydrated (FFPE only), subjected to antigen retrieval conditions to expose masked/crosslinked antigens, blocked with serum proteins to reduce nonspecific binding, and stained with a cocktail of metal-conjugated antibodies followed by a heavy metal DNA intercalator. Regions of interest (ROIs) on stained sections are ablated and analyzed by the IMC instrument, which measures the heavy metal content in each ablated segment of tissue (approximately 1 µm^2) and corresponds to individual pixel intensities in the greyscale output images for each metal/marker channel. These multiplexed images are then subjected to cell segmentation using DNA staining images to identify nuclei and structural marker images to identify cytoplasm and cell boundaries (when applicable), and exported with an accompanying cell segmentation mask to various data analysis pipelines (described in section 2.2.5).

As of August 2019, there is only one commercially available IMC instrument, the Hyperion Imaging System, which is sold by Fluidigm and couples with either of their two most recent CyTOF systems (CyTOF2 and Helios). A schematic of the Hyperion system coupled to the Helios along with a detailed explanation of its function is shown in Figure 2.4.
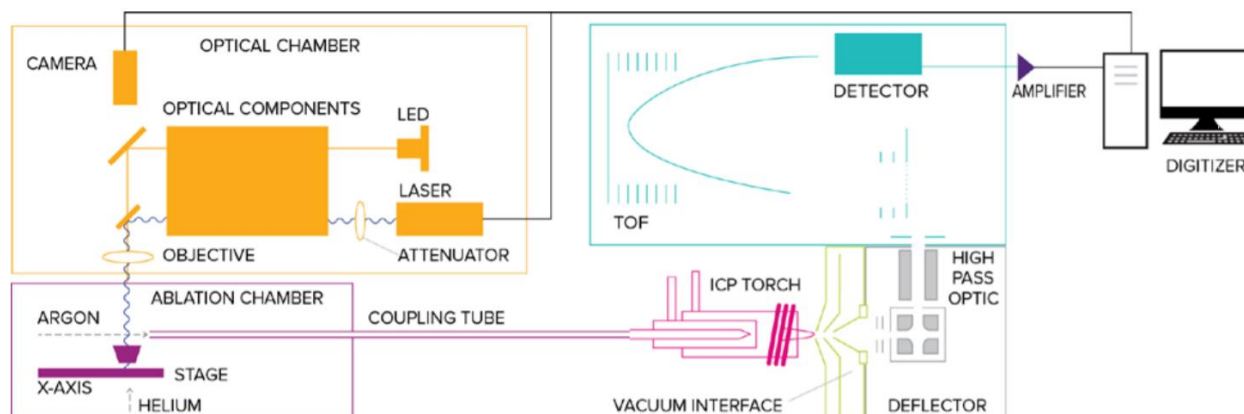
Figure 2.4: Schematic of the inner workings of the Hyperion and Helios. A sample slide with a mounted section stained with a cocktail of metal-tagged antibodies is loaded in the ablation chamber (purple) of the Hyperion system. An LED-based optical imaging system acquires a panorama of the sample and can also monitor sample ablation by an attenuator-pulsed laser focused through the same objective lens (yellow) that rasters along the tissue. Each laser pulse that strikes the sample produces a plume of ablated material, which is collected into a coupling tube and transferred to the Helios using an inert Argon carrier gas. The the ablated sample material in the plume is vaporized, atomized, and ionized in the inductively coupled plasma (ICP) torch (pink). Uncharged atoms and low mass elemental ions are consecutively filtered out with a deflector and high pass optical filter, respecitvely (grey), and the resulting ion plume is accelerated in discrete slices into the time-of-flight (TOF) chamber (blue), where ions are separated by their mass (momentum) according to the time it takes them to reverse direction in an electromagnetic field. The mass-separated ions hit a detector which produces an analog signal that is amplified, digitized, and converted to individual counts of each heavy metal isotope in the plume slice (black). The counts are summed from all slices in the plume to yield a pixel intensity for each metal, which are assembled into the final output images. Schematic taken from the Hyperion Imaging System user guide (Fluidigm PN 400311 A2).

2.2.3 Antibody conjugation

In order for antibodies to be used to detect various proteins in IMC, they must be conjugated with heavy metals. The most commonly used strategy (although others exist) is to partially reduce the disulfide bridges between the heavy and light chains, breaking some of the bonds and reducing them to thiol groups. A chelating polymer containing maleamide groups that readily react with the thiols is pre-loaded with lanthanide (heavy metal) ions, and when combined with the partially-reduced antibody, catalyzes a covalent bond permanently linking the heavy metal to the antibody though a maleamide-sulfide bridge (Figure 2.5). The polymer and residual metals are washed away via spin column purification. Both the metal conjugation and the antibody recovery from the spin column have varying efficiencies, and partial reduction of some antibodies can eliminate their antigen binding capabilities; therefore,

antibodies must ideally be tested for metal content (by running through a the CyTOF at a diluted concentration) and binding specificity by IMC or before using in regular experiments.
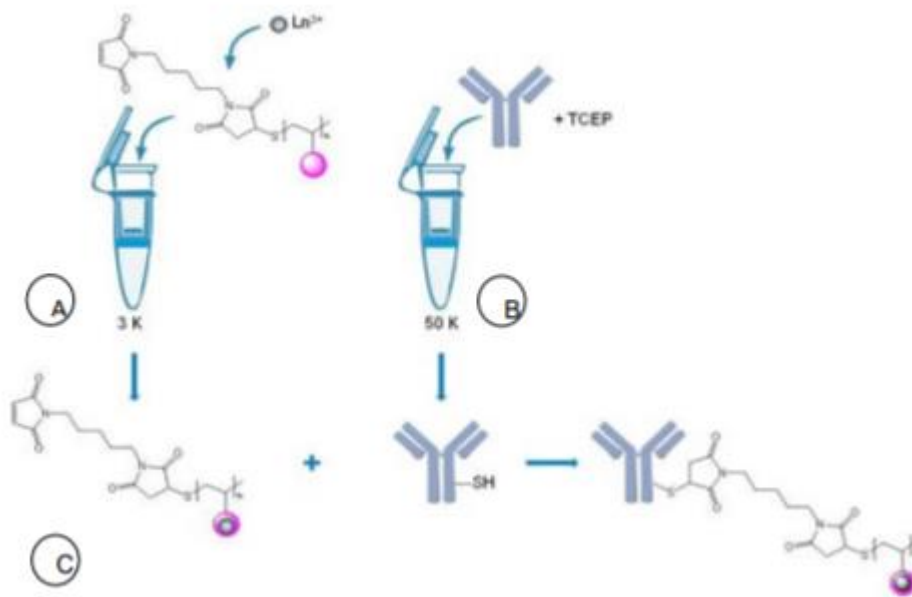
Figure 2.5 Conjugation chemistry of the MaxPar polymer-mediated antibody conjugation process. Taken from the MaxPar Antibody Labeling Kit protocol (Fluidigm, PRD002 Version 11)

2.2.4 Panel Development Strategy

Many considerations must be factored into the design and development of an IMC panel; foremost is the selection of markers and corresponding targeting antibodies to test and include, as well as which heavy metal channel a particular marker should be detected in if there are conjugates (pre-conjugated antibodies) available in multiple channels or if the antibody must be conjugated in-house. Priority is given to markers central to the research goals being addressed, which in this case is Axl/GFP and tdTomato (RFP), followed by markers that can assign an approximate phenotype to every cell type expected to exist in the given tissue (LEP, MEP, fibroblasts, and immune cells in the mammary), then pan-structural markers for the identification of cytoplasm for cell segmentation and ECM components to denote tissue compartments and cell-ECM interactions, and finally other research markers of interest that can further segregate various cell types (including epithelial lineages and immune cells) into smaller subpopulations or elucidate signaling mechanisms. For markers with relatively low abundance in the tissue of interest, it is recommended by Fluidigm to use metals within the 153-176 Da range, where the instrument is most sensitive (Fluidigm Panel Design Guidelines, PN 13-01_150711). In our group, a large inventory of existing conjugates were already available from our ongoing CyTOF experiments, which provided the advantage of not having

to build a panel completely from scratch. The general strategy employed in this study for the testing and inclusion of antibodies into epithelial stem cell-oriented panels for mammary and lung tissue is shown in Figure 2.6.

Figure 2.6: Antibody conjugation strategy for this study. The majority of the experiments focused on the first two steps, where a large inventory of existing suspension mass cytometry antibodies were tested in IMC and more Hyperion-validated antibodies were acquired and added to a backbone of pre-tested antibodies from the first step. Finally, tissue specific markers were conjugated and incorporated into the panel. If unique detection modalites are desired, some channels can be devoted to other techniques that expand on the platform, such as protein colocalization or mRNA detection.

3. Project Aims

Overall Aim: Elucidate the role of Axl in normal stem epithelial cells and determine how this function is coopted during malignant transformation.

Central Hypothesis: Axl signaling induces cellular plasticity in normal epithelia in response to non-homeostatic conditions, specifically in those of the mammary gland ducts during puberty and lung alveoli during regeneration and repair, which provides an evolutionary and mechanistic link to Axl signaling in cancer.

Specific Aims:

1) Breed and characterize *Axl-CreERT2-GFP* and *Axl-CreERT2-GFP/Rosa26-tdTomato* mouse strains to study the functional properties of Axl+ stem cells *in vivo* and *in vitro*

This aim focuses on the genotyping and selective breeding of mice generated by Ozgene in order to establish homozygous transgenic strains for use in *in vivo* lineage tracing studies and *in vitro* functional studies using cell culture and organoids. Standard fluorescence-based imaging and flow-cytometry approaches are performed using the *Axl-CreERT2-GFP* strain for eventual application in a *Axl-CreERT2-GFP/Rosa26-tdTomato* mammary stem cell lineage tracing study.

2) Develop an IMC panel for interrogation of stem cell dynamics in breast and lung tissue and *in vitro* organoid sections

This aim endeavours to establish an IMC panel of up to 40 metal-conjugated antibodies to allow measurement of stem cell dynamics *in situ* in various epithelial tissues and their derived organoids at a high spatiotemporal resolution. The IMC panel is designed and iteratively tested on the Hyperion imaging system using an existing CyTOF antibody inventory and new antibodies conjugated commercially or in-house.

3) Establish an IMC analysis pipeline and repository of antibody testing data to enable the use of the platform to study Axl+ stem cells

This objective of this aim is to synthesize all of the troubleshooting issues, antibody feasibility testing and data analysis pipeline optimizations addressed in the current work into actionable recommendations and strategies that empower other users and future experiments.

4. Materials and Methods

4.1 Mouse Models

The generation, breeding, and experimental use of all mice listed in this paper was approved by the Norwegian Food Safety Authority and performed in accordance with the Regulation on Animal Experimentation (Norecopa). The background of all mice was C57BL/6J.

4.1.1 Generation of *Axl-CreERT2-EGFP* knock-in mice

This work was performed by a commercial vendor (Ozgene Inc., Perth, Australia) in consultation with our group. Embryonic stem (ES) cells isolated from C57BL/6J mice were transfected with the linearized gene targeting vector previously illustrated in Figure 2.2. Upon transfection, the gene targeting vector is sporadically incorporated into the target locus during cell division by homologous recombination due to its sequence overlap with exon 20 of the Axl gene on its flanking ends. The small fraction of resulting transgenic ES cells were then selected from wild type cells by exposure to neomycin, as they express a resistance cassette, and injected into proprietary goGermLine blastocysts. The resulting male offspring produced only ES cell-derived transgenic offspring that were heterozygous for the Axl knock-in allele, which were subsequently crossed with homozygous *Rosa26-Flp* mice. The ubiquitously expressed flp recombinase excises the FRT-flanked neomycin resistance cassette from the knock-in construct in the resulting offspring, since it can have unintended effects on the target gene or surrounding genes [64]. A final round of breeding was performed to select for homozygous *Axl-CreERT2-EGFP* mice (all heterozygous *Rosa26-Flp/Wt*) which were shipped to our animal facility. In addition, some of these mice were crossed with homozygous *Rosa26-TdTomato* mice (Jackson labs, stock number 007905) and the offspring were inbred. From this litter, homozygous *Axl-CreERT2-EGFP* mice that were heterozygous for *Rosa26-TdTomato* were selected and shipped to our animal facility. All mice were selected using a real-time-PCR (rt-PCR) genotyping assay designed in-house by the vendor.

4.1.2 Genotyping and breeding of mice received from Ozgene

Once the mice arrived from Ozgene, two breeding objectives needed to be completed before any experiments could take place: (1) Cross the homozygous *Axl-CreERT2-EGFP Rosa26-Flp/Wt* mice to selectively breed out the Flp allele and establish a long-term stock colony that could be bred to other Cre-based reporter strains in future experiments, and (2) cross the homozygous *Axl-CreERT2-EGFP Rosa26-TdTomato/Wt* mice to selectively breed out the Wt allele so that these mice could be used in lineage tracing experiments. When establishing a transgenic strain, it is ideal to select and maintain mice that are homozygous for each transgenic allele so long as heterozygotes are not required for experiments since homozygous mice can be bred with impunity and require less genotyping surveillance. Additionally, having two copies of each reporter gene in the lineage tracing mice maximizes their expression and subsequent fluorescent signal in experiments, which is particularly relevant considering the rarity of Axl-expressing stem cells in the tissues being interrogated. Consistent with our concurrent genotyping of other strains, endpoint PCR was used to genotype the *Axl-CreERT2-EGFP* mice, and all primers used are shown in Table 4.2.

Target allele	Forward (F) and Reverse (R) primer sequences (5'-3')	Product length	Source
Axl-CreERT2-EGFP knock-in	F: CATGGACTGCATCTGAGAAGGG R: CCTAAGGATTCCTGTAGCTGTCTC	440 base pairs	Designed by Ozgene specifically for this strain
Axl-Wt	F: CATGGACTGCATCTGAGAAGGG R: ATGGAGCATCTGTACAGCATGAAG	286 base pairs	
Rosa26-Flp	F: TAGAACAGCTAAAGGGTAGTGC R: TTACACCTGTTCAATTCCCCTG	538 base pairs	Ozgene stock genotyping assay
Rosa26-Wt	F: AAGGGAGCTGCAGTGGAGTA R: CCGAAAATCTGTGGGAAGTC	297 base pairs	Jackson labs genotyping assay (recommended by Ozgene)
Rosa26-TdTomato	F: GGCATTAAAGCAGCGTATCC R: CTGTTCCTGTACGGCATGG	196 base pairs	
Rosa26-TdTomato	F: AACTGCCCGGCTACTACT R: GCTCGTACTGTTCCACGATG	87 base pairs	Ozgene RT-PCR assay

Table 4.2 Primer sequences used to genotype *Axl-CreERT2-EGFP* mice

Genotyping assay optimization

Since the original mice from Ozgene had already been genotyped at their facility before being sent to us, DNA samples taken from these mice served as positive controls for our genotyping assays. DNA was extracted from mouse ear punches as follows: 2mm ear punch biopsies were added to 75µl of a solution containing 25mM NaOH and 0.2mM EDTA, pH ~12 and incubated for 95°C for 30 minutes, cooled to 4°C, then quenched with 75µl of 40mM Tris-HCl, pH ~5. This crude lysate was used as DNA template for the subsequent PCR assays. A list of all reagents and all thermal cycle conditions used in the genotyping assay optimization can be

found in Tables 4.3 and 4.4, respectively. All runs in our lab were performed on an Eppendorf 950000015 Mastercycler Gradient thermal cycler and analyzed on 1% (w/v) agarose gels.

Reagent	Supplier	Product Number
KlearKall (enzyme/mastermix, 2X)	Biosearch Technologies	KBS-1001-001
Phusion HF polymerase kit (+5X HF buffer, MgCl2)	Thermo Fisher	F530S
Q5 High-Fidelity DNA polymerase	NEB	M0491S
Q5 High-Fidelity 2X Master Mix	NEB	M0492S
dNTP solution mix	NEB	N0447S
Betaine	Merck	B2629
AmpliTaq Gold DNA Polymerase with Gold Buffer	Applied Biosystems	4311806
Primers, lyophilized (see table 3.2)	Merck	Custom order
O'GeneRuler 1kb DNA ladder and 6X loading dye	Thermo Fisher	SM1163

Table 4.3 Reagents used in PCR genotyping assay optimization.

Protocol name	Standard	Jackson	Alternate	Ozgene	JHN
source	in-house	Jackson labs	in-house	Ozgene	Oslo lab
lid temp	95	95	100	100	105
activation temp	95	94	94	98	94
time	7 min	2 min	3 min	30 sec	10 min
denaturation temp	94	94	94	98	94
time	30 sec	20 / 15 sec	20 sec	10 sec	20 sec
annealing temp	gradient 54-69	65-0.5 first 10 cycles, then 60	55	gradient 54-69	61
time	30 sec	15 sec	30 sec	30 sec	30 sec
extension temp	68	68 / 72	72	72	72
time	90 sec	10 sec	30 sec	2 min	30 sec
# cycles	35	10 / 30	35	30	35
final extension temp	68	72	72	72	72
time	7 min	2 min	2 min	10 min	2 min
	4C hold	4C hold	4C hold	4C hold	4C hold

Table 4.4: Thermal cycle conditions used in PCR genotyping assay optimization. All temperatures are in degrees Celsius. Gradient represents a range of annealing temperatures across 8 wells. The Jackson protocol uses a "touchdown" strategy where the annealing temperature starts at 65°C and decreases by 0.5°C per cycle until it reaches 60°C for the rest of the cycles.

Once the genotyping assays had been optimized to detect the *Rosa26-Flp/Wt* and *Axl-CreERT2-/Wt* alleles, they were used to selectively breed out the *Flp* allele and establish the *Axl-CreERT2-EGFP* stock strain. This strain was then used in Axl-GFP characterization experiments.

4.1.3 Characterization of Axl-GFP expression in *Axl-CreERT2-EGFP* mice

In order to evaluate experimental methods crucial to the *Axl-CreERT2-EGFP/Rosa26-TdTomato* lineage tracing study and observe the distribution of Axl-GFP expression in various

organs, two approaches were pursued: (1) observe spatial distribution of Axl-GFP+ cells via fluorescence imaging of tissue cryosections and whole-mounted mammary glands, and (2) determine the frequency of Axl-GFP+ cells in lung and mammary gland by dissociating the tissue and measuring cells via flow cytometry.

Axl-CreERT2-EGFP 12-week-old female mice were placed in an isoflurane chamber until unconscious, sacrificed via neck dislocation, and transcardially perfused with ~5 mL phosphate-buffered saline (PBS). Various organs, including lung, kidney, spleen, and mammary glands, were dissected and harvested. One inguinal mammary gland was whole mounted to SuperFrost Plus microscope slides (Thermo) while the other glands were placed in a petri dish for dissociation. One lung was also placed in a petri dish for dissociation, while the other was submerged in Tissue-Tek OCT compound (VWR) and flash-frozen in liquid nitrogen along with the rest of the harvested organs. *For the remainder of all experiments using these organs, samples were protected from light to preserve fluorescent protein signal.*

Fluorescent Imaging

Fresh-frozen organs were sectioned on a cryotome with a thickness of 3-5 µm, mounted to Superfrost Plus microscope slides and fixed for 30 min in 4% paraformaldehyde (PFA) at room temperature (RT) followed by three washes in PBS. At this point, some samples were set aside for IMC staining and imaging on the Hyperion system (Run 4 in section 5.3, protocol described in section 1.2.3). For cryosections undergoing fluorescence imaging, slides were stained with 10 µg/mL Hoescht 33342 (Thermo) in PBS for 30 minutes at RT, then destained in PBS for 30 min at RT, before being mounted with glass coverslips using Fluoromount AG and imaged on an Olympus VS120 slide scanner at 10X resolution (0.6493 µm pixel diameter), using the DAPI (blue) and FITC (green) channels to measure DNA (Hoescht stain) and eGFP, respectively.

Whole-mounted mammary glands were immediately fixed in 4% PFA for 1.5h at 4°C, then cleared in 50% (v/v) glycerol/PBS for 4 hrs at room temperature (RT). Samples were then placed in 50% glycerol/PBS containing 10 µg/mL Hoescht 33342 (Thermo) and stained overnight at RT with mild agitation. The next day, samples were destained for 1h each in 50%, 75%, and 100% glycerol in PBS, respectively, with mild agitation. A coverslip was mounted on each sample slide with glycerol and the sample was compressed to flatten out the tissue as

much as possible before imaging. Fluorescent images of the cleared and stained whole-mounted mammary glands were immediately acquired on an Olympus VS120 slide scanner at 10X resolution, using a 50 µm EFI scan depth and the same fluorescence channels mentioned above. Since there were many blurry areas in the first acquisition, a second acquisition was performed that used the FITC channel instead of the DAPI channel for autofocusing.

In order to capture more spatial information from the 3D structure of the whole mounted glands, the instrument software (VS-AWS) utilizes a technique known as extended focal imaging (EFI) which acquires images from multiple focal planes (z-depth) above and below the autofocus plane, extracts the most in-focus areas from each focal plane using an edge-finding algorithm, and stiches them together into a single image. This is done separately for each field of view, called a "tile", and the resulting tiles are stitched together into the final output image. Due to the resolution and size of the stitched 10X image, it is too large to be viewed in its entirety on most computers (requires too much RAM). Thus, images are exported as a virtual slide image (.vsi file format), which uses an indexed hierarchy of image stacks at compressed resolutions so that the highest resolution is only loaded when zooming into a small area. Among the few open-source programs that can handle and interpret these files, QuPath (v0.2.0-m1) was chosen due to its speed and cell detection modules [65]. QuPath was used to estimate the number of GFP+ cells in lung and spleen cryosections and whole mounted mammary gland as a proportion of the total number of cells. First, all cells were detected by their Hoescht-stained nuclei (in the DAPI channel) using the cell detection molecule (default parameters) and a nucleus expansion of 5 µm to mark the cell membrane boundary. Next, positive cells were detected using the "select objects by measurement" module, excluding cells in regions near autofluorescent artifacts (hairs and bubbles). The measurement parameters were empirically determined based on the ability to discriminately select a subset of manually-identified positive cells, and set as "Cytoplasm: FITC channel max > 800 AND Cytoplasm: FITC channel mean > 400".

Lung and mammary dissociation and flow cytometry

Mammary gland and lung samples from the aforementioned dissection were thoroughly minced in PBS and subjected to specialized dissociation protocols that were previously established in-house. Minced lung lobes were transferred to a gentleMACS C tube (Miltenyi Biotech) containing 2.6 mL of dissociation buffer (5 mL Hank's buffered salt solution (HBSS) with 10mM HEPES, 75 µg/mL Liberase (Roche), and 20 µg/mL DNase I (Stem Cell

Technologies)) and dissociated on the gentleMACS Dissociator (Miltenyi Biotech) with the program "m_lung_01", followed by a 30 min incubation at 37°C with inversion every 5 min and the program "m_lung_02". The dissociated cell/tissue solution was strained through a 70 µm filter which was then rinsed with an additional 2.5 mL dissociation buffer. The cells were washed twice with 5 mL PBS by centrifuging at 300 g for 10 minutes and resuspended in 3 mL MilliQ water for flow cytometric analysis. Minced mammary glands were transferred to a 50 mL falcon tube containing 2 mL of 12.5 mg/mL collagenase and 13 mL Epicult-B Mouse medium with supplements (StemCell Technologies, cat. #05610) and incubated for 4 hrs at 37°C with gentle shaking. The resulting slurry was vortexed and triturated with a pipette and cells were collected by centrifuging at 150 g for 5 min at RT and discarding the supernatant. The pellet was resuspended with 10 mL of a cold 1:4 mixture of HBSS with 2% FBS (HF buffer) and Ammonium Chloride Solution (StemCell, cat. #07850) to lyse residual red blood cells and centrifuged at 450 g for 5 min at RT. The supernatant was discarded and the pellet was resuspended in 2 mL pre-warmed 0.25% Trypsin-EDTA (Sigma) and mixed with a pipette for 3 min to release single cells, which were then washed by adding 10 mL HF buffer, centrifuging at 150 g for 5 min at RT, and removing the supernatant. The pellet was mixed for 1 min with 2.2 mL of prewarmed HBSS with 5 mg/mL Dispase with 0.1 mg/mL DNase I (StemCell, cat. #07913/07900) to digest free ECM proteins and DNA, respectively, and diluted in 10 mL cold HF buffer before filtering through a 40 µm cell strainer into a new 50 mL falcon tube. The single cell solution was centrifuged at 450 g for 5 min at RT, the supernatant was discarded and the pellet was resuspended in MilliQ water for flow cytometric analysis.

Dissociated lung and mammary cells were analyzed on an Accuri C6 flow cytometer (BD Biosciences), using the FL3 and forward and side-scatter detectors to detect GFP and single-cell events, respectively. One million events were collected per sample. To determine the stability of the fluorescent GFP signal, the remaining lung cells were split into two groups: one untreated and left in light, and another fixed in 4% PFA and protected from light, which were analyzed 4 hrs later. Flow cytometric data was analyzed in FlowJo software (v10.6.1).

4.1.4 Axl-LacZ mouse model

The B6.129P2-*Axltm1Dgen*/J mouse strain, which is homogenous for the *Axl-LacZ* insertion (from section 2.1.2) was purchased from the Jackson Laboratory (stock # 005777) for previous experiments in our group. The strain was originally generated by Deltagen, Inc. by introducing

the LacZ gene and an FRT-flanked neomycin resistance cassette into exon 11 of the mouse *Axl* gene using homologous recombination in ES cells in a similar fashion as the *Axl-CreERT2-EGFP* strain. Previously, organoids were grown from mammary cells isolated from Axl-LacZ HET and Axl-LacZ KO mice using the same dissociation protocol described above. Cells were labeled using a commercial FDG reporter kit (FluoReporter® 469 lacZ Flow Cytometry Kit, Molecular Probes cat. #F-1930) following the manufacturer's protocol and sorted by a FACS ARIA (Becton Dickinson) cell sorter into FDG-(Axl)-low and -high samples, which were then seeded in Matrigel and cultured into organoids for approximately 2 weeks. Sections of formalin-fixed paraffin embedded (FFPE) lung, mammary glands and organoids were IF stained (using antibodies against K5, K8 and/or β-gal with DAPI nuclear stain). X-gal staining was performed on some organs prior to FFPE, sectioning, Eosin counterstaining, and brightfield imaging. In the current work, these same FFPE samples were sectioned and analyzed with IMC (Run 2/5 in Section 5.3).

4.1.5 4T1 mammary tumorigenesis model

BALB/c mice were orthotopically injected with 4T1 breast cancer cells as part of another study. Tumors developed under the skin, and mice were monitored daily and sacrificed when their tumor volume reached the cutoff value set for the study. One FFPE tumor from this study was used in Run 3 of the IMC experiments.

4.2 IMC

4.2.1 Antibody Conjugation

All in-house conjugations were performed using MaxPar Antibody Labeling Kits (Fluidigm), which contain polymer, loading buffer (L-buffer), reduction buffer (R-buffer), conjugation buffer (C-buffer) and wash buffer (W-buffer), following the manufacturer's protocol. Unless otherwise mentioned, all centrifugation steps were performed at 12,000 g at RT and flow-through from the spin columns was discarded when necessary. MaxPar X8 polymer was equilibrated to RT, dissolved in 95 µl L-buffer and 5 µl of the specified lanthanide (heavy metal) ion solution and incubated for 30 min at 37°C in a heat block. Meanwhile, the concentration of the antibody to be conjugated was measured on a Nanodrop 2000 spectrophotometer (Thermo Scientific). If the antibody was originally in glycerol, the stock

solution was filtered through a 50 kDa spin filter (Amicon) and resuspended in the initial stock volume of PBS before measuring. A calculated volume of antibody equivalent to 100 µg (or the entire volume if <100 µg in total) was added to a 50 kDa filter along with 300 µL R-buffer and spun down for 10 min. The antibody was reduced by adding 100 µL of 8 mM TCEP (Thermo) in R-buffer and incubating for 30 min at 37°C. The metal-loaded polymer was transferred to a 3 kDa filter, diluted in 200 µL L-buffer and spun down for 25 min, and washed again by resuspending in 400 µL C-buffer and spinning down for 30 min. The antibody reduction was quenched by adding 300 µL C-buffer and spinning down for 10 min, and washed by resuspending in an additional 400 µL C-buffer and spinning down for 10 min. The metal-loaded polymer was resuspended in 80 µL C-buffer and transferred to the 50 kDa filter with the reduced antibody and incubated for 90 min at 37°C in a heat block to conjugate the antibody. Following conjugation, the antibody was washed and the polymer was removed by adding 200 µL W-buffer and spinning down for 10 min, with an additional three wash cycles of 400 µL W-buffer. The conjugated and purified antibody was resuspended in 100 µL of W-buffer and quantified via Nanodrop in order to calculate the volume of antibody stabilizer (CANDOR Bioscience) needed to elute the antibody at a concentration of 0.5 mg/mL. After removing the W-buffer by spinning down for 10 min, the calculated volume of antibody stabilizer was added and the filter was inverted, placed in a new collection tube and collected via centrifugation at 1000 g for 2 min. The conjugated antibody was stored at 4°C in the dark until use.

4.2.2 Generation of 4T1 control cell pellets

In order to produce mock tissue samples for IMC testing that served as positive controls for important markers such as Axl and GFP, cells were cultured, fixed and embedded in pellets. 4T1 BALB/c breast cancer cells were previously harvested, and the GFP gene was inserted into exon 11 of the Axl gene using CRISPR-Cas9 gene editing as previously described [66], serving as a functional Axl knockout while expressing functional GFP. All cell culture steps were performed in a sterile laminar airflow hood, and the incubator was always set to 37°C with 5% CO_2 and 21% O_2. One million 4T1 and 4T1 Axl-KO-GFP cells each were seeded in T75 flasks and cultured in 10 mL cell culture medium (RPMI1640 with 10% FBS, 2 mM L-glutamine, 100 U/mL penicillin and 100 µg/mL streptomycin, all from Sigma) in an incubator. When the cells reached 80-90% confluency, they were trypsinized with 5 mL pre-warmed 0.25% Trypsin-EDTA, quenched with 10 mL cell culture medium, centrifuged at 290 g for 7 min at RT, and split into 2 T175 flasks containing 20 mL cell culture medium. This process

was repeated again in order to grow 4 confluent T175 flasks each of the two cell types, which were trypsinized, pelleted by centrifugation (same settings) in a 50 mL conical tube, and resuspended and fixed in 5 mL 4% PFA for 1 hr at RT. After a brief (2 min) stain with 40 µL methyl green, cells were washed twice by adding 15 mL PBS, centrifuging and removing the supernatant. The resulting cell pellets were gently but thoroughly resuspended in 60 µL human blood plasma, to which 30 µL of 100U/ml thrombin was added and mixed. After incubating for 20 min at RT to allow coagulation to occur, the resulting pellets were carefully removed from the bottom of the tube and securely placed in plastic tissue embedding cartridges and submerged in 4% PFA until embedding in paraffin the next day. The resulting tissue blocks were sectioned for IMC analysis.

4.2.3 Sample preparation workflow

Fresh-frozen and FFPE tissue blocks were sectioned at 5 thickness on a cryotome or microtome, respectively, mounted on SuperFrost Plus microscope slides and stained with metal-conjugated antibodies per Fluidigm's suggested protocol for Hyperion analysis (Protocol ID PN 400322 A3). All solutions were made with MilliQ water and kept in plastic bottles to avoid heavy metal contamination, and all washes were performed in 50 mL conical tubes at RT with gentle agitation. Briefly, FFPE tissue slides were baked for 2 hrs at 60°C to remove as much wax as possible before dewaxing in consecutive xylene solutions for 2 x 10 min, followed by rehydration in descending grades of ethanol (100%, 95%, 80%, 70%) for 5 min each. Serial sections for H&E staining (if required for the experiment) were then separated, processed according to standard protocols [67], and imaged on the Olympus VS120 slide scanner at 10X resolution. Slides for IMC analysis were then washed in MilliQ water for inserted in 50 mL conical tubes containing preheated antigen retrieval (AR) solution (10mM Tris Base, 1mM EDTA, 0.05% Tween 20, pH 9.0) and incubated at 96°C for 30 min in a hot water bath. The tubes were removed from the bath and allowed to cool to 70°C before washing twice with MilliQ water and twice with PBS. To prevent nonspecific binding of antibodies to tissue or Fc receptors, tissue sections were encircled with an ImmEDGE hydrophobic barrier pen (Thermo) and covered with a solution of 3% BSA in PBS in a hydration chamber for 1 hr at RT. During this blocking step, a cocktail of metal-conjugated antibodies was prepared by adding the calculated concentration of each conjugate to a small volume of 3% or 10% BSA in PBS (depending on whether the total amount of antibody added was >83% of the desired cocktail volume) and diluting in PBS to a final BSA concentration of 0.5%. Detailed lists of all antibodies used in each experiment can be found in section 5.3. If the cocktail preparation

took longer than 1 hr, the BSA blocking step was ended by submerging the samples in PBS until the cocktail was ready. The sections were then covered with antibody cocktail solution (~50-75 µL per 10 mm^2 section) and stained overnight in a hydration chamber at 4°C. The next day, sections were washed twice in 0.2% Triton X-100 in PBS and twice in PBS for 8 min each for a total of 4 washes. The sections were then covered and stained with Iridium DNA intercalator (Cell-ID™ Intercalator-Ir, Fluidigm cat. #201192A) for 20-30 min in a hydration chamber at RT, washed for 5 min in MilliQ water, and air-dried for at least 20 min before analyzing on the Hyperion instrument. Fresh-frozen sections from section 1.1.3 were processed with the same protocol, starting at the AR step.

4.2.4 Hyperion instrument setup and operation

If the instrument was initially in SMC mode (Helios only), the Hyperion module was carefully positioned using an alignment tool such that the coupling tube fed orthogonally into the sample inlet (Fig 2.4). Next, the argon and helium gas valves were opened and the plasma coil was turned on. A 3-Element Full Coverage Tuning Slide (Fluidigm, PN 201088) was loaded onto the slide stage, the laser was turned on and autotuning was performed, which optimizes the xy calibration of the plume path and the flow of the helium gas that carries the plume to the detector and gives a general indication of the instrument sensitivity, which must be >500 Lu(175) counts/plume and ideally >1000 counts/plume. Next, a crude image of the sample slide was acquired on a smartphone and uploaded in the HTI acquisition module, and the slide was loaded onto the sample stage. Panoramas were taken of the sample slide based on the tissue locations of interest on the crude image, taking into account any potential xy offset between the crude image and the actual sample position. The laser intensity was then calibrated by choosing a non-relevant area of tissue to ablate at different intensities, and setting the laser intensity such that all of the sample was ablated but the glass underneath was not being burned. Next, ROIs were selected on the panorama images of the sample based on guidance from serial H&E/fluorescent images or a general indication of what tissue region was relevant. An acquisition template including all metals utilized in the panel along with their corresponding markers, the desired laser intensity and ablation frequency (always 200 Hz) was created and assigned to all ROIs, which were then ablated and the resulting multiplexed images were exported as an .mcd file.

4.2.5 Data analysis pipeline

Exported IMC data was opened in MCD Viewer software (Fluidigm, v1.0.560), and the staining quality of each antibody was subjectively evaluated and annotated for each ROI and tissue type based on the signal intensity (auto threshold max), presence of aggregates, +1/-1 channel spillover, and expected staining pattern inferred from the literature (IHC/IF applications) and colleagues. Based on this information, markers were chosen to export as .ome.tiff images for downstream analysis. The folder of exported images was then loaded into the data analysis pipeline in CellProfiler (Broad Institute Inc., v2.2.0). In some instances, thresholding was applied on channels containing aggregates to eliminate unnatural high-intensity pixels. The signal intensities of the two Iridium DNA intercalator isotopes and selected cytoplasm/membrane markers (if available) were combined and scaled for visibility using the ImageMath function into a "DNA" image and a "Cellular" image, respectively. Nuclei were identified using the IdentifyPrimaryObjects function with "DNA" as the input image and cells were identified using either the IdentifySecondaryObjects function with a 1 pixel (1 µm) expansion from the nucleus or, if structural markers were available, using the "Cellular" image in IdentifyPrimaryObjects. Cytoplasm was identified using the IdentifyTertiaryObjects function, which selects objects between the cell and nucleus outlines. The parameters affecting the performance of these functions were empirically determined for each sample type and are outlined in section 5.3. The nuclei, cell, and cytoplasm objects were each converted into image masks (uint16 color format) and saved in the same folder as the original images exported from MCD Viewer as .ome.tiff files. The folders containing staining images and masks for each ROI in an experiment were imported into histoCAT (Fluidigm/Bodenmiller Lab, v1.76). In histoCAT, the cells in each image were clustered and visualized based on their staining intensity values for each marker using phenograph and tSNE, respectively. Segmentation parameters were sometimes recursively adjusted based on these data. When applicable, neighborhood analysis was performed to characterize interaction frequencies between cells [68].

5. Results

5.1 Genotyping optimization and troubleshooting

run #	Variables tested (differences from previous run)	PCR protocol	Primer set 1	Primer set 2	mouse genotype	Gel result
1	Generic in-house assay conditions: KlearKall enzyme/MMX, 1uM primers and 10% template DNA input, gradient PCR cycle conditions	Standard	FLP		FLP/WT	VERY faint band at lowest 2 annealing temps
			TdT	R26-WT	Td/WT	Strong WT band, no TdT band
			Axl-KI	Axl-WT	KI/KI	Strong KI band at all annealing temps
2	Touchdown PCR cycle conditions	Jackson	FLP		FLP/WT	no visible bands
			FLP	R26-WT	FLP/WT	WT band, no FLP band
			TdT	R26-WT	Td/WT	WT band, no TdT band
			Axl-KI	Axl-WT	KI/KI	strong KI band
3	Phusion polymerase + HF buffer, extra MgCl2 (2.6mM), 0.5uM primers	Jackson	FLP	R26-WT	FLP/WT	Smeared NSPs, WT band, no FLP band
			TdT	R26-WT	Td/WT	Smeared NSPs, WT band, no TdT band
			TdT		Td/WT	Many discrete NSPs but no TdT band
			R26-WT		Td/WT	4 strong bands, one corresponding to WT product size
4	1M betaine, 0.1uM primers, Ozgene gradient PCR conditions	Ozgene	FLP		FLP/WT	Visible FLP band, faint NSP @ low temp
			TdT		Td/WT	No TdT band
5	Q5 enzyme/MMX (no betaine), 4-fold sample dilution series (to test for PCR inhibition by lysate)	Alternate	FLP		FLP/WT	Very faint FLP band @ 0.5-0.015 ul input
			R26-WT		Td/WT	Strong WT product band @ 2ul, NSPs @0.5-0.015 ul
			TdT		Td/WT	No TdT band

Table 5.1: Genotyping optimization of *Axl-CreERT2-EGFP Rosa26-Flp/TdTomato* mice. Each run is identical to the one above it except for the changes listed in the "variables tested" column. All mice were homozygous for the *Axl-CreERT2-EGFP* knock-in (Axl-KI) construct. Detailed thermal cycle conditions for each PCR protocol can be found in Table 3.4. The Standard and Ozgene protocols utilize a gradient PCR, meaning that each sample was tested over a range of annealing temperatures in 8 identical reactions. Each gel result represents testing of at least 2 mice with the same reported genotype (according to Ozgene). MMX: master mix; FLP: *Rosa26-Flp* allele; TdT: *Rosa26-TdTomato* allele; NSP: nonspecific PCR product.

The general strategy employed for genotyping assay optimization was to start with our current in-house genotyping protocol and modify various PCR conditions such as sample input volume, thermal cycle conditions, polymerase type or mastermix components until distinct PCR products matching the expected size could be amplified from the corresponding positive control samples and visualized by gel electrophoresis, using separate conditions for each target allele if deemed necessary. Typically this is not required for endpoint genomic PCR assays as they are quite robust, however in this case an extensive optimization was carried out due to the inability to initially detect the Flp and TdTomato transgenes. A summary of the initial PCR genotyping assay optimization experiments can be found in Table 5.1.

In summary, the *Axl-CreERT2-EGFP* knock-in allele was detected in all mice tested, across all PCR conditions, and no *Axl-wt* products were ever observed, since all mice were homozygous for the knock-in mutation. The *Rosa26-Flp* allele was only able to be detected when betaine was added to the mastermix, and thus required its own assay protocol. The *Rosa26-TdTomato* allele, however, was not detected in any of the optimization experiments performed, despite extensive testing of many different mastermix/enzyme formulations (e.g.

KlearKall, Thermo Phusion, NEB Q5) with both gradient and touchdown PCR protocols. One notable run using a very robust PCR protocol with Phusion polymerase (400-fold increased sensitivity over Taq polymerase) and touchdown PCR (cycles with incrementally lower annealing temperatures to ensure the target sequence is amplified) showed that the Jackson TdTomato primers could amplify many nonspecific products from the two Ozgene TdTomato/wt lysates but not TdTomato, strongly indicating that the target sequence was not present (Figure 5.1).
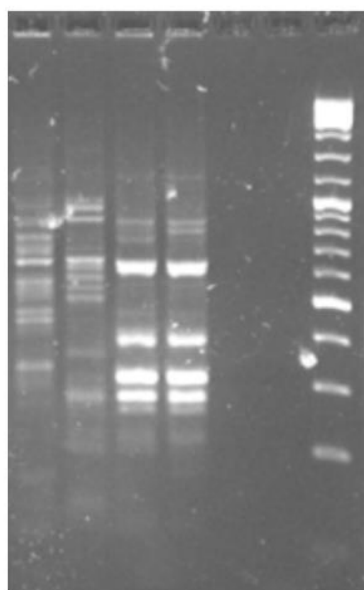

Figure 5.1: Robust PCR conditions still fail to detect the presence of the *Rosa26-TdTomato* reporter gene. *From left to right: 2 Td/wt mice with TdTomato mutant primers, 2 Td/wt mice with wt primers, 2 empty lanes, DNA ladder. TdTomato exp. product size: 196bp. WT exp. product size: 297bp.*

500bp
400bp

300bp

200bp

This prompted us to consider one of two possibilities: 1) our protocol (either the lysis or the PCR itself) was suboptimal; or, 2) the mice did not harbor the TdTomato reporter allele. A collaborator at University of Oslo (UiO) Cancer Center (Dr. Jens Henrik Norum's group) also used the same TdTomato reporter mice and routinely genotyped them in their lab. Therefore, we brought our old lysates from the original Ozgene TdT/Wt mice and fresh, unlysed ear samples from their offspring to UiO and ran them through our collaborators' lysis and genotyping protocol (same Jackson labs primer sequences, ampliTaq Gold polymerase, and the Alternative PCR thermal cycle conditions) alongside some lysates from their lab that they had previously confirmed were positive for TdTomato (Figure 4.2). The positive control samples were brought back to our lab and the results were confirmed in an independent experiment using the same protocol (data not shown).
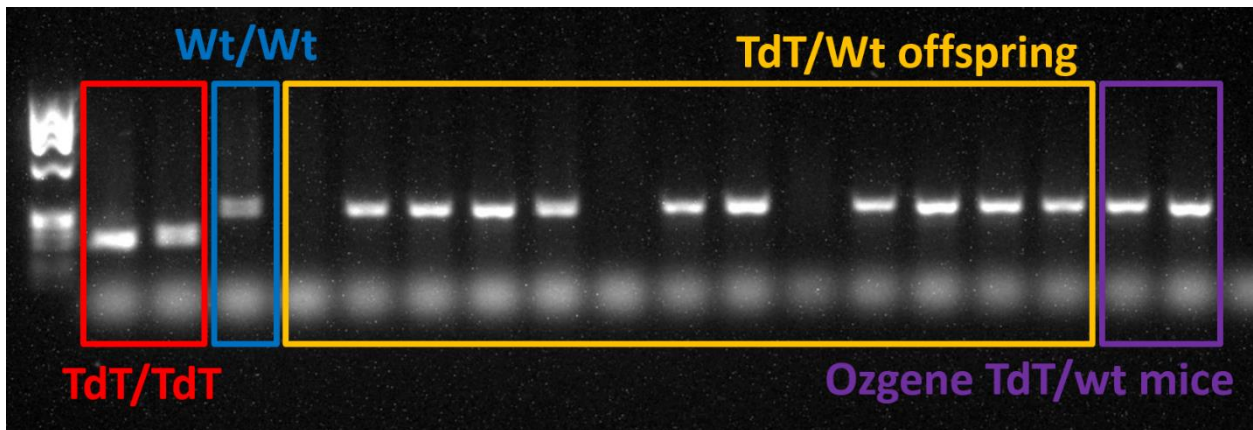
Figure 5.2: PCR genotyping results of Ozgene mice and their offspring run alongside positive controls for *Rosa26-Wt* and *TdTomato* at UiO. Samples were analyzed with both TdTomato and Wt primers in a single PCR reaction. Positive control samples from previously confirmed *TdTomato* (red) and *WT* (blue) homozygous mice show PCR products with distinctly different sizes corresponding to the expected product size from each primer set. Samples from the original Ozgene mice allegedly heterozygous for TdTomato (purple) only showed Wt product bands, while the offspring of these mice (yellow) showed only Wt bands or no band at all.

These data further confirmed the lack of TdTomato in the mice we received from Ozgene. However, the fact that some of the offspring lacked a Wt product was indicative of a cross between two heterozygous mutants, prompting us to consider if the identity of the samples taken from the original Ozgene mice were somehow mismatched (due to the complex earmarking codes used by Ozgene) and that the *Rosa26-FLP* mice were accidentally used for breeding. Therefore, all mice received from Ozgene were carefully resampled, lysed, and tested in Bergen using fresh TdTomato, Flp and Wt primers (Jackson) ordered through the same vendor that was used in Oslo (data not shown). This run confirmed that the samples were not mismatched. After communicating our concerns to Ozgene, they responded by noting that they have been successfully maintaining the *Axl-CreERT2-EGFP-Rosa26-Wt/TdTomato* strain at their facility using an in-house real-time PCR (rt-PCR) assay. Although this strategy measures the cumulative cleavage of a fluorescent reporter from a probe sequence targeting a midpoint region between the forward and reverse primers to quantify target amplification, these primers should still produce an end product detectable by gel electrophoresis. Therefore, these primers (last row in Table 3.2) were ordered and tested on the Ozgene and positive control lysates with endpoint PCR using the same protocol as the prior two runs (data not shown). Even using the primers that Ozgene recommended to genotype the strain, we could not detect TdTomato in any of the original mice received from Ozgene, while the primers clearly worked for the two positive TdTomato control samples from UiO. All of the aforementioned genotyping data was compiled into a report and sent to Ozgene in August, and all experiments regarding the *Axl-CreERT2-EGFP-Rosa26-Wt/TdTomato* mice, including lineage tracing and organoid studies, were put on hold.

5.2 Characterization of mouse models

While the genotyping optimization was taking place, the *Axl-CreERT2-EGFP-Rosa26-Wt* mice were used in experiments to measure and confirm Axl-GFP coexpression in various tissues. These experiments were performed to test the feasibility of the various analytical techniques required to evaluate the Axl-GFP strain and the planned lineage tracing study, while organoid experiments were rather conducted in the established Axl-LacZ strain.

5.2.1 Whole-mount mammary imaging

The whole-mounted mammary fluorescence image acquired in Section 4.1.3 from a 12-week-old female *Axl-CreERT2-EGFP* mouse was analyzed both subjectively and quantitatively to determine the presence of GFP+ cells. Visual inspection of the image in QuPath revealed two distinct patterns of expression: rare isolated GFP+ cells located in either the stroma or the mammary epithelia (Figure 5.3A), and ubiquitous GFP expression by endothelial cells lining the lymphatic ducts. These ducts drain to the lymph node at the center of the mammary gland, whose strong green fluorescence can be attributed to either the presence of Axl-GFP+ immune or endothelial cells in the node, or autofluorescence. It was difficult to ascertain the three-dimensional location of the rare GFP+ cells in relation to the mammary ducts, and therefore no conclusion could be drawn as to whether these cells were in fact the rare suprabasal Axl+ progenitor cells we were looking for in this strain. The QuPath analysis modules mentioned previously were used to quantify both the total number of cells (nuclei) and number of GFP+ cells, which were 496,179 and 828 cells, respectively, meaning the proportion of GFP-positive cells was ~0.17%. It is important to note that only discrete GFP+ cells were detected (like those in Figure 5.3A), while excluding endothelial cells.
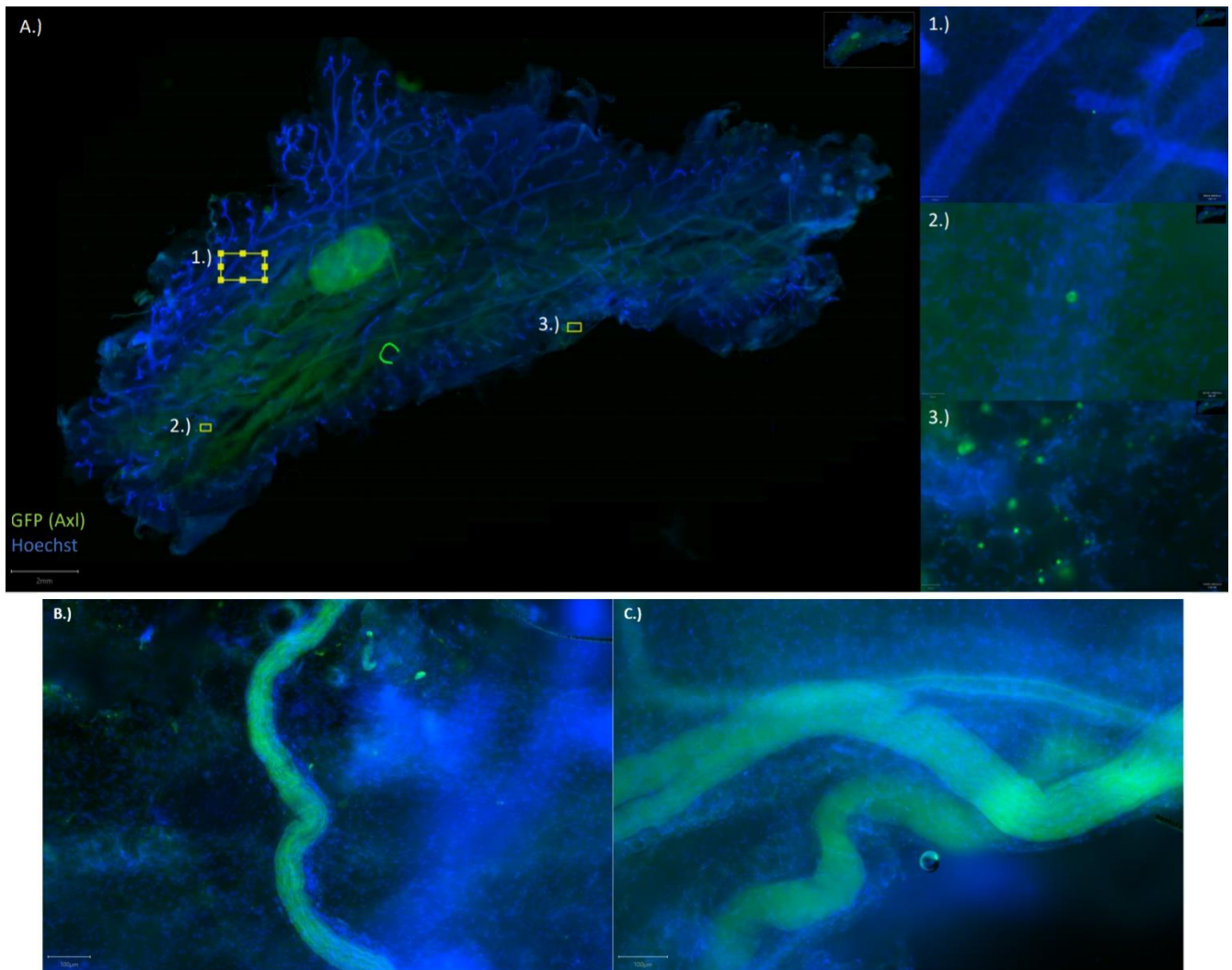
Figure 5.3: Fluorescent EFI scan of a whole-mounted *Axl-CreERT2-EGFP* mouse mammary gland. (A) Rare putative Axl-GFP+ cells located near or within mammary epithelial ducts (1-2) and at a cluster at the edge of the gland area (3). (B, C) GFP was ubiquitously expressed by lymphatic endothelial cells, which are well-visualized by the EFI technique. Blue: hoechst DNA stain; green: GFP.

5.2.2 Fluorescent cryosection imaging

Spleen and lung cryosections from the same mouse pictured above are shown in Figure 5.4A and B, respectively. Although GFP+ immune cells are clearly distinguishable in both pulps of the spleen, the expression of GFP was more uniformly scattered in the alveoli with some rare cells showing more intense, point-like GFP expression. Referencing basic lung histology (Figure 5.4C) [69] and prior X-gal staining of Axl-LacZ-HET mice in our group (Figure 5.4D) suggested that the GFP expression pattern was indicative of Axl+ type 2 lung cells and endothelial vessel cells.
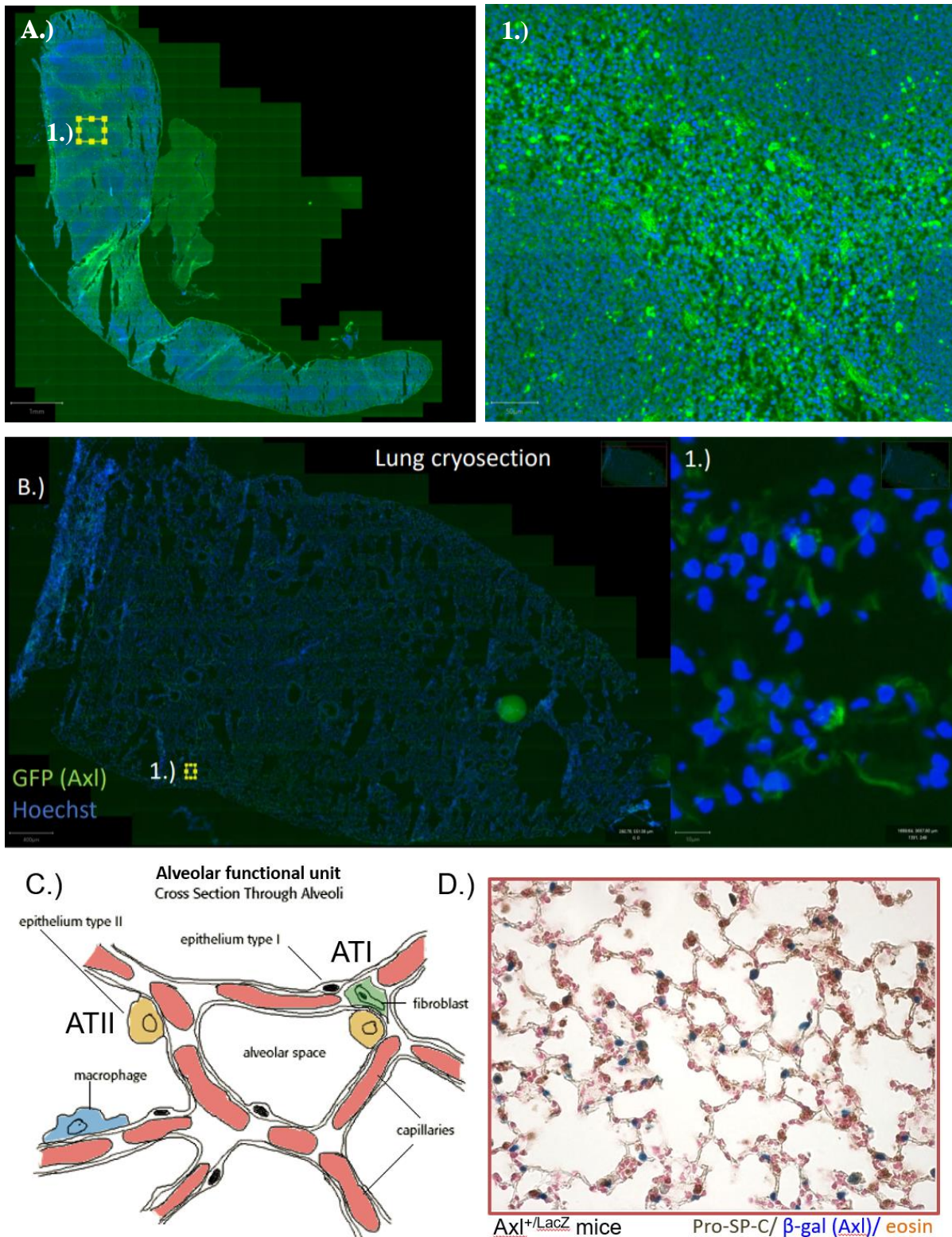
Figure 5.4: GFP expression in lung (A) and spleen (B) cryosections from an *Axl-CreERT2-EGFP* mouse. Magnified regions of whole-organ scans denoted with (1). (C) Reference illustration of the lung alveolar functional unit, comprising of thin type 1 (ATI) and secretory type 2 (ATII) epithelial cells with resident macrophages and fibroblasts. (D) Brightfield image of alveoli from Axl[+/LacZ] (Axl-LacZ-HET) mice immunohistochemically stained for Pro-SP-C (an ATI marker) and stained with X-gal to detect the β-gal Axl reporter and eosin counterstain. C adapted from [68] and D from Lorens lab.

5.2.3 Flow cytometry of mammary and lung cells

The ability to detect GFP+ cells from the same mouse in the preceding experiments was determined by flow cytometric analysis of dissociated mammary gland and lung cells. The quantification of GFP+ cells in both samples is shown in Figure 5.5.
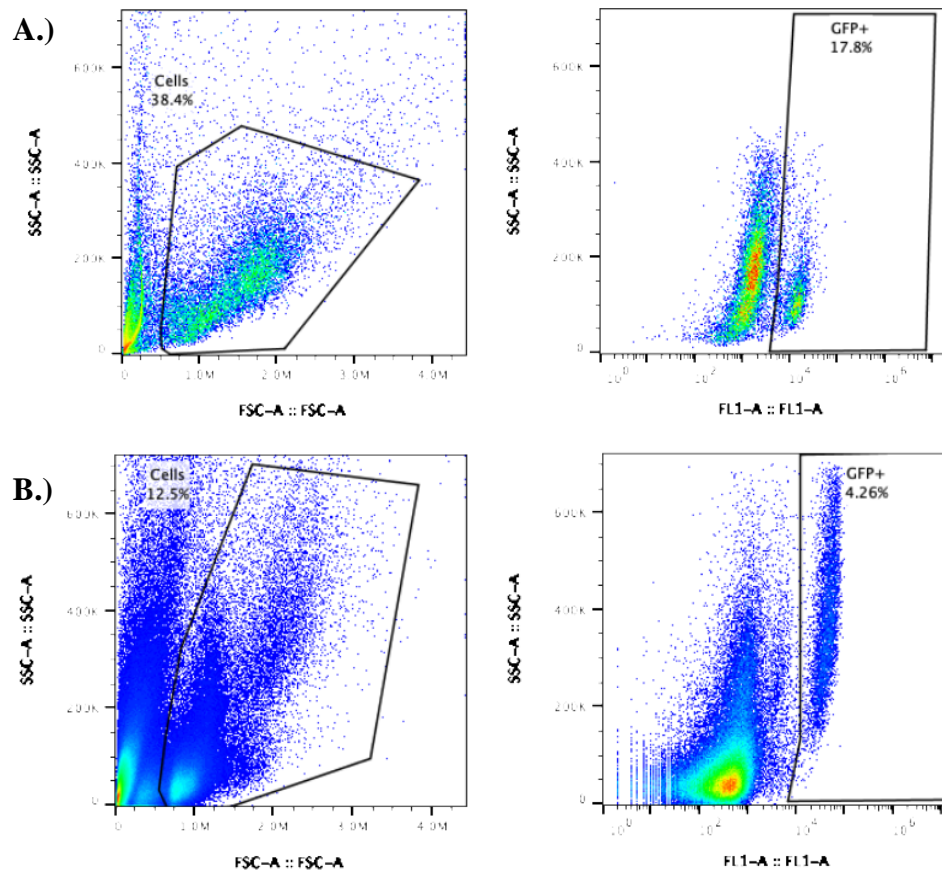
Figure 5.5: Gating and quantification of a subset of GFP+ cells from dissociated *Axl-CreERT2-EGFP* mouse mammary gland (A) and lung (B) tissue analyzed by flow cytometry. Single cells were separated from debris and doublets by gating on a plot of forward scatter area (FSC-A) versus side scatter area (SSC-A). A distinct GFP+ population was visible in both samples when plotting single cells on a graph of fluorescence channel 1 (FL1, detects GFP) area versus SSC-A. This population was gated and quantified as a percentage of total single cells (GFP+ %).

5.3 IMC

The results of each IMC experiment are systematically and chronologically presented below. For each run, the underlying rationale for the experiment will be briefly presented, followed by any supporting H&E or IF images that were used to guide ROI selection. Next, a table summarizing each antibody used in the experiment is provided, that states the purpose of each marker, the source of the antibody (referred to as a "clone" if it is monoclonal in origin) and which heavy metal it was conjugated with, the relative confidence that the antibody would work in the given sample type (on a scale of 1-3) and the reasoning supporting this rating, the concentration tested, whether the overall staining quality was unacceptable (-), acceptable (+), excellent (++), or not conclusive (NC) and in which tissues, possible reasons why the staining didn't work if the quality was (-) or (NC), and any issues observed in the particular channel either directly associated with the antibody staining or resulting from neighboring channels.

The confidence score was based on the following scale: 3, previously tested in-house showing strong staining or validated by Fluidigm on the Hyperion system; 2, indications from the literature or manufacturer that the antibody worked on the sample type being analyzed (frozen or FFPE) or previous testing showing weak staining; 1, no indication of successful application in the given tissue type from any source. All experiments were performed on mouse cells or tissue, and all antibodies were stated by the manufacturer to be reactive against the murine ortholog of the target protein. The concentrations of all pre-conjugated IMC/CyTOF antibodies from Fluidigm were initially unknown (since a standard volume of 1 µL per million cells is recommended for CyTOF), and some but not all of the concentrations were eventually obtained from Fluidigm. For those antibodies whose concentration was still unknown, a rough assumption was made based on the known range of Fluidigm conjugate concentrations and the general intensity of expression of a given target protein (which is inversely correlated with the conjugate concentration), and these assumed concentrations are marked in bold/italics. Any markers with (+) or (++) staining in a given tissue were included in downstream analysis. A general description is given of the outcome of the experiment, including any overarching issues encountered, and representative images of particularly notable combinations of marker staining are shown for each tissue (the black-and-white images of every channel recorded in each experiment for representative ROIs are listed in an appendix, see section 10). Finally, the data analysis steps performed for each tissue type are described with accompanying figures.

5.3.1 Run 1: FFPE cell pellets

In order to test several key antibodies on control samples that were either positive or negative for specific markers and to evaluate the Hyperion workflow for the first time, sections of FFPE 4T1 WT and AXL-KO-GFP cell pellets (from section 4.2.2) were stained with a 2-fold titration (dilution) series of the antibody cocktail described in Table 5.3.1 (the concentration column represents the starting concentrations in the dilution series, denoted T4, and the dilutions are denoted as T3-T1 in descending order of concentration). A section of each cell type was also stained with a solution containing no antibodies (T0) to observe background signal. No supporting H&E images were required to guide ROI selection, since the samples were homogenous and any region could be selected on the pellet area at random.

Heavy metal tag	Target	Cell type	Cellular Location	Antibody Clone ID	Vendor	Product #	Pre-stain Conf. Score	Reason	Cocktail Conc. (µg/mL)	staining result	If (+), which tissues, if (-)/NC, poss. reasons	staining issues (if any)
153Eu	PD-L1	4T1 WT/KO	LIG	10F.9G2	Fluidigm	3153016B	1	NI	5	**NC**	CTNP?	
169Tm	GFP	4T1 KO	CYT	5F12.4	Fluidigm	3169009B	1	NI	5	**NC**	CTNP?	
170Er	MerTK	4T1 WT/KO	MEM	2B10C42	BioLegend	151502	1	NI	5	**NC**	CTNP?	
176Lu	Axl	4T1 WT	MEM	175128/107332	R&D Systems	MAB854/MAB8541	2	LIT	5	**+**	4T1 WT and KO	NSB?

Table 5.3.1: List of antibodies used in Run 1. Cellular location refers to what part of the cell the marker should be found. LIG, ligand (cytosolic or extracellular); EC, extracellular; CYT, cytosolic; MEM, membrane. The staining confidence score is on a scale of 1-3. Reasons behind the confidence score are: LIT, from the literature; NI, no indication. For markers that did not show positive staining, possible reasons include: CTNP, cell type not present; NSB, non-specific binding. Refer to the HUGO guidelines for all target abbreviations.

DNA AXL   DNA AXL   PD-L1 MerTK GFP   PD-L1 MerTK GFP   DNA AXL PD-L1 MerTK GFP
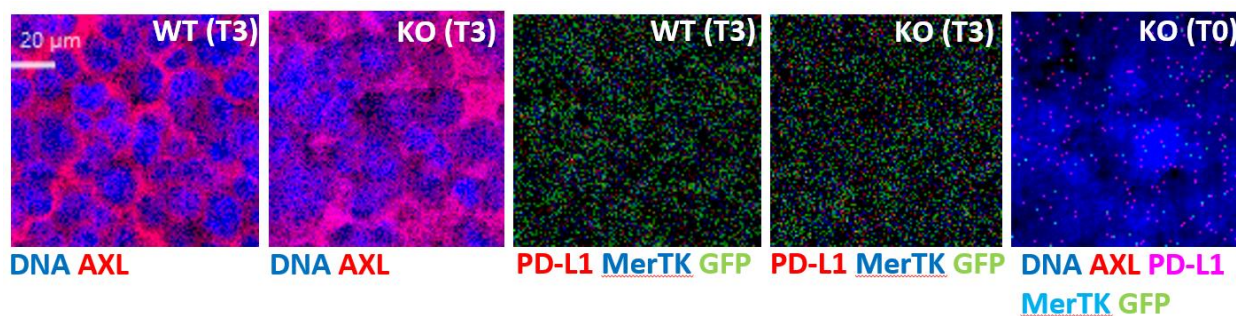
Figure 5.3.1A. IMC images of 4T1 Axl wild-type (WT) or -GFP+-knockout (KO) cell pellets stained with a cocktail of heavy metal-conjugated antibodies. Matching samples of KO and WT cell pellets (from the same cocktail titration) are shown, with DNA and Axl staining in one image and PD-L1, MerTK, and GFP in another image of the exact same ROI from left to right. The rightmost image shows another KO pellet section stained with PBS/BSA only (no antibody).

AXL staining was evident in both the WT and KO cells, while staining of all other markers was not detected, as only noise (random single antibodies not washed from the slides) was visible in these channels (Figure 5.3.1A). It is unclear whether the cells did not express these proteins or that the staining was ineffective.

When viewed and exported from MCD viewer, the default pixel intensity range of each channel in the IMC image is automatically set such that the maximum intensity corresponds

to the 95th percentile of pixel counts for the given heavy metal per image, known as "auto threshold counts". As a general rule of thumb, the conjugate staining quality can be considered too weak for recommended use if the auto threshold counts are below 5, since the positive signal from the antibody at this level usually cannot be distinguished from the noise resulting from random nonspecific antibody binding. This noise increases with increasing antibody concentration, as shown in Figure 5.3.1B.
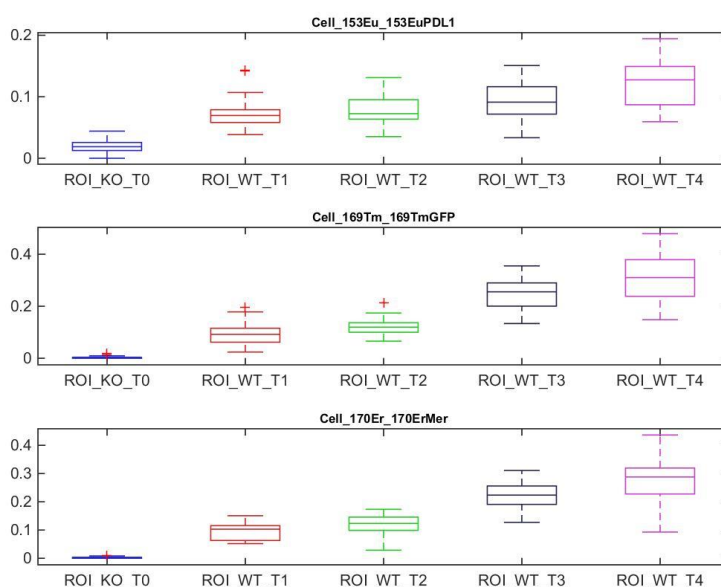

Figure 5.3.1B: Distributions of mean single-cell metal counts from 4T1 WT pellets stained with a titration series of conjugated antibody cocktail. The noise contributing to nonzero cell intensities is roughly correlated with increased antibody concentration (T1-T4). Data generated with HistoCAT.

The mean cell counts are zero or very close to zero for the T0-stained pellets, indicating that most of the random noise in each metal channel is due to the presence of residual conjugates and not from heavy metal contamination of the sample or instrument. In order for the single cell intensity to be measured, cell segmentation must be performed on the images, which was done using the default settings in the IdentifyPrimaryObjects function in CellProfiler to generate a cell mask for each image (Figure 5.3.1C). For such quantitation measurements to be proportional, the nuclei of the cell population being measured must be fairly homogenous, which was not the case with the 4T1 knockout cell pellet sections (Figure 5.3.1D).
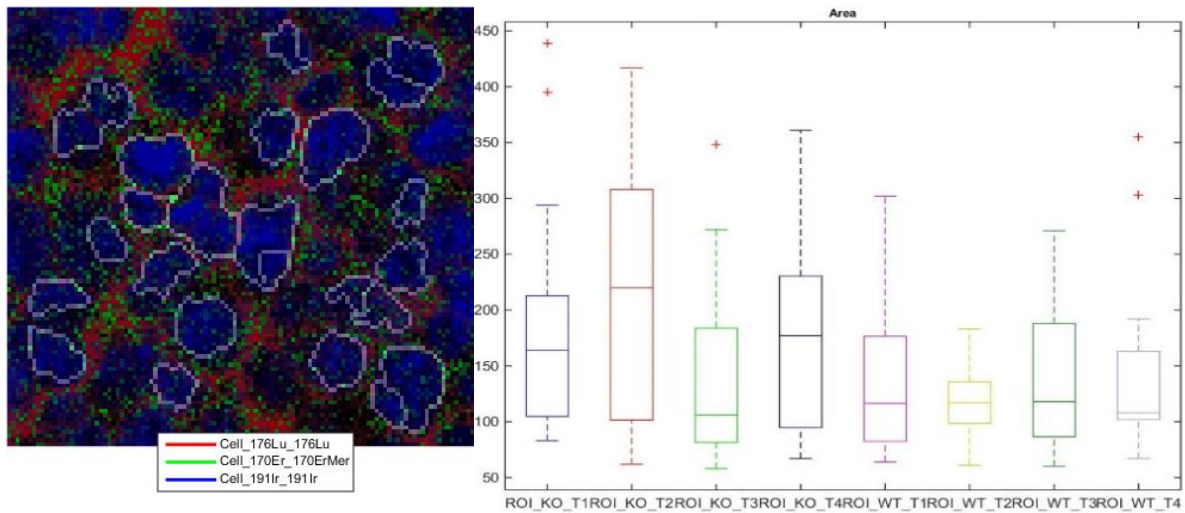
Figure 5.3.1 C&D. (C) (left) representative cell mask image generated from DNA stain images in CellProfiler overlaid on the sample image with several markers shown in color. (D) (right) Distribution of nuclear areas from cell segmentation in each sample (from left to right: KO T1-4, WT T-14). Data generated with HistoCAT.

The Axl cell staining intensity was also correlated with increased antibody concentration (Figure 5.3.1E), and since the auto threshold counts were above the cutoff value and a distinct staining pattern was observed, this can be considered as true antibody signal. However, this signal may arise from nonspecific binding of cellular regions since the same staining pattern was observed in the supposedly Axl-null cells. Moreover, since two Axl-targeting clones were tested in the same metal channel (a strategy often employed to enhance sensitivity to a low-abundance antigen), the performance of either individual antibody could not be distinguished.
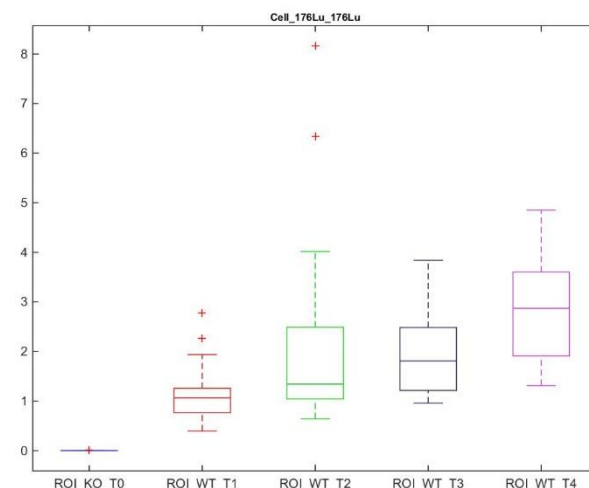

Figure 5.3.1E: Distributions of mean single-cell 176Lu-Axl counts from 4T1 WT pellets stained with a titration series of conjugated antibody cocktail. Data generated with HistoCAT.

5.3.2 Run 2: FFPE mammary gland and lung

Since the cell pellet experiments were inconclusive and likely not indicative of the staining quality in FFPE tissue, an IMC antibody cocktail was then tested on the target tissues of the intended stem cell panel: mouse mammary and lung. A list of all antibodies used in the cocktail and their staining results is shown in Table 5.3.2.

conjugate	Target	Purpose / Cell type	Cellular Location	Clone #	Supplier	Product #	Pre-stain Conf. Score	Reason	Cocktail Conc. (µg/mL)	staining result	If (+), which tissues, if (-)/NC, poss. reasons	staining issues (if any)
141Pr	K5/6	basal/MEP marker	CS	D5	millipore	MAB1620	2	LIT	10.0	++	lung/mam	NCA
142Nd	CD11c	DCs, NK cells, some activated T cells	MEM	N418	Fluidigm	3142003B	1	NI	2.5	NC	CTL/CTNP	DA
144Nd	CD115	monocytes, macs, EpC, tumors	MEM	AFS98	Fluidigm	3144012B	2	LIT	5.0	NC		DA
145Nd	CD4	Helper T cells	MEM	RM4-5	Fluidigm	3145002B	2	UV/LIT	5.0	-	CTL/CTNP	
146Nd	CD8a	Cytotoxic T cells	MEM	53-6.7	Fluidigm	3146003B	2	LIT	5.0	-	CTL/CTNP	DA
147Sm	CD45	Immune Cells	MEM	30-f11	Fluidigm	3147003B	2	UV/LIT	1.0	+	lung/mam	CTL/NCA
148Nd	PD-1	activated T/B lymphocytes	MEM	RMP1-30	Thermo	14-9981-82	1	NI	10.0	-	CTNP	DA
149Sm	CD83	mature DCs	MEM	Michel-17	Thermo	14-0831-82	1	NI	10.0	-	CTNP	DA
150Nd	CD24(a)	LPC & MPC	GR	M1/69	Fluidigm	3150009B	1	NI	4.0	++	lung/mam	
151Eu	CD64	monocytes, macs, DCs	MEM	X54-5/7.1	Fluidigm	3151012B	1	NI	2.5	-	CTL/CTNP	
152Sm	CD3e	T cells	MEM	145-2C11	Fluidigm	3152004B	2	UV	2.0	-	CTL/CTNP	
153Eu	PD-L1	Immune checkpoint inhibition	LIG	10F.9G2	Fluidigm	3153016B	2	SSA	6.0	-	CTNP	
156Gd	CD103	intra-Ep lymphocytes, binds E-cad	MEM	2E7	Thermo	14-1031-85	1	NI	10.0	-	CTNP	
158Gd	E-cadherin	Epithelial marker	MEM	24E10	Fluidigm	3158021A	3	HVA	5.0	++	lung/mam	
159Tb	F4/80	macrophages	MEM	BM8	Fluidigm	3159009B	2	LIT	6.0	-	NSB	
160Gd	Arginase-1	M2a macrophages	CYT	polyclonal	Novus Bio	NBP1-32731	2	SSA	5.0	NC	NSB/CTNP	
161Dy	pErk1/2	signaling	CYT	D13.14.4E	Cell Signaling	9101 / 4370	3	HVA	10	-	NSB	
162Dy	Ly6C	memory T cells, monocytes	MEM	HK1.4	Fluidigm	3162014B	2	LIT	2.0	NC	CTL/CTNP	DA?
163Dy	K19	LEP marker	CS	Troma III	DSHB	TROMA-III	2	LIT	1.1	++	mam	
164Dy	CD49b	regulatory T cells	MEM	HMa2	Fluidigm	3164011B	1	NI	5.0	-	CTL/CTNP	
167Er	YAP	Hippo pathway	CYT	H-9	santa cruz bio	sc-271134	2	SSA	2.5	NC	NSB	
168Er	CTLA4	Immune checkpoint inhibition	MEM	UC10-4B9	Thermo	14-1522-82	1	NI	5.0	-		DA++
169Tm	CD206	M2a macrophages	MEM	C068C2	Fluidigm	3169021B	1	NI	5.0	-		NCA
170Er	K14	myoepithelial marker	CS	polyclonal	Thermo	PA5-13672?	2	LIT	1.1	NC	CTL/NSB	
171yb	CD80	active DCs, monocytes, macs	MEM	16-10A1	Fluidigm	3171008B	1	NI	5.0	-	CTL/CTNP	
172Yb	CD86	early active DCs, monocytes, macs	MEM	GL1	Fluidigm	3172016B	2	UV/LIT	2.5	-	CTL/CTNP	
173Yb	CD44	cancer stem cell marker, basal cells	MEM	IM7	Fluidigm	3150018B	3	HVA	5.0	++	lung/mam	CTH
174Yb	Ly6G/C	polymorphonuclear neutrophils	MEM	RB6-8C5	Fluidigm	3174008B	2	UV/LIT	5.0	-	CTL/CTNP	
176 Lu	Axl	Stemness, immune evasion	MEM	175128	RnD	MAB854	3	PT-S	5.0	NC	CTL	
176 Lu	Axl	Stemness, immune evasion	MEM	107332	RnD	MAB8541	3	PT-S	5.0	NC	CTL	

Table 5.3.2: List of antibodies used in Run 2. Cellular location refers to what part of the cell the marker should be found. LIG, ligand (cytosolic or extracellular); EC, extracellular; CS, cytoskeleton; CYT, cytosolic; MEM, membrane. The staining confidence score is on a scale of 1-3. Reasons behind the confidence score are: NI, no indication; LIT, from the literature; UV, Hyperion user-validated; SSA, supplier-suggested application; HVA, Hyperion-validated antibody; PT-S, previously tested--strong staining. For markers that did not show positive staining, possible reasons include: CTNP, cell type not present; NSB, non-specific binding; CTL, concentration too low. Staining issues include: DA, direct aggregate (from antibody in channel); NCA, neighboring channel aggregate. "+" signs indicate the issue is more pronounced (2-fold increase per "+" sign). Refer to HUGO guidelines for all marker abbreviations.

Many pre-conjugated antibodies were available from our existing inventory of CyTOF clones and were evaluated for their feasibility in IMC. In order to guide ROI selection on the sample panoramas acquired by the Hyperion, serial (coming from the section directly above or below the IMC-stained section) H&E images of Axl-wild type and Axl-LacZ-KO mammary and wild-type lung tissue sections were acquired and are shown in Figure 5.3.2A.
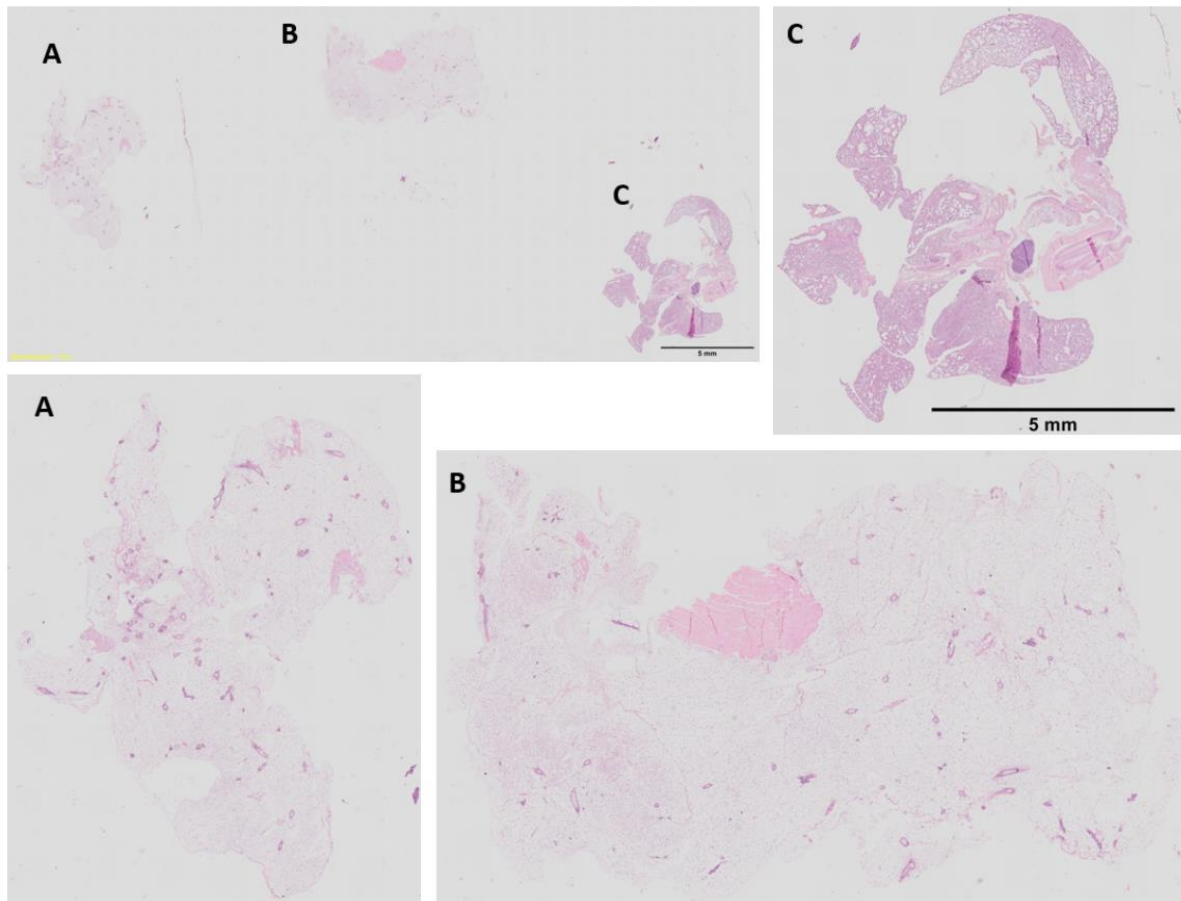
Figure 5.3.2A: Serial H&E images of Axl-Lac-KO mammary gland (A) and Axl wild-type mammary gland (B) and lung (C). ROIs for IMC ablation containing ducts and other tissue compartments were selected on mammary sections, while ROIs containing alveolar compartments and upper respiratory airway structures were selected on lung sections.

Representative IMC images of notable marker combinations in each tissue are shown in Figure 5.3.2B. In general, very few of the IMC antibodies showed positive staining in either of the tissues tested, which could be because many of the antibodies targeted antigens not highly expressed in either tissue due to the cell type not being present, particularly in the (relatively small) ~100 μm^2 ROIs selected. Another possibility is that the assumed concentrations of many of the antibodies were too low, and not enough was added to the cocktail. Additionally, many high-intensity aggregates were observed, some of which were a single pixel in diameter while others seemed to colocalize to specific points, indicative of dust contamination.
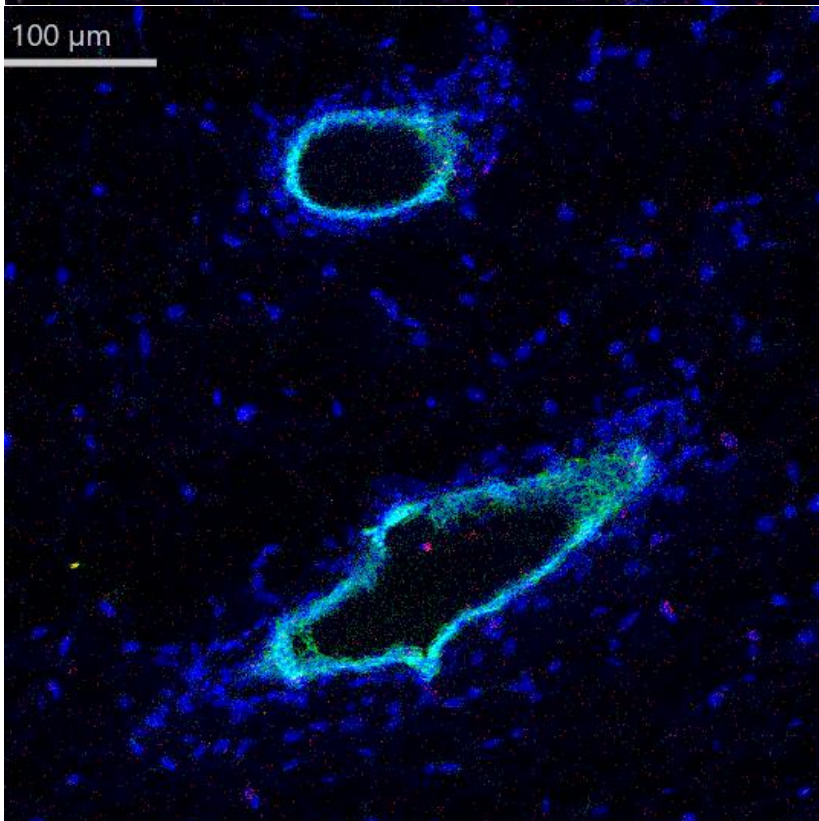
Blue = DNA, Lime = K5/6

Blue = DNA, Red = E-Cadherin, Yellow = CD44

Merged

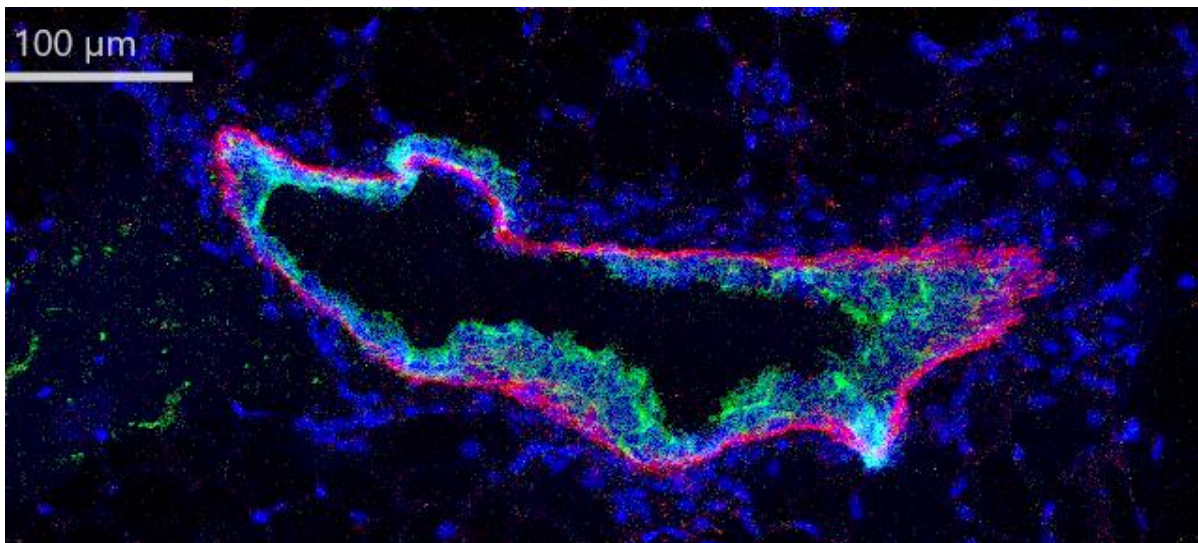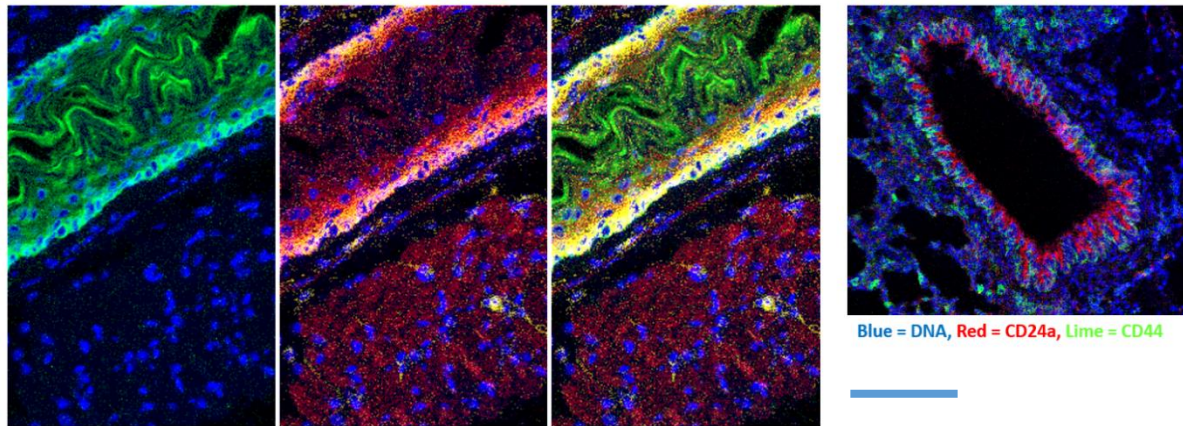Blue = DNA, Red = CD24a, Lime = CD44

100 µm

100 µm

Figure 5.3.2B: Representative IMC images of notable markers in each tissue type. Upper left: pulmonary vessel in lung, upper right: bronchioli structures with basal and epithelial markers. Middle: mammary duct with basal and luminal markers (red: K5/6, green: K19). Bottom: mammary duct with epithelial and immune markers (red: CD45, green: E-cadherin)

Despite the relatively low success rate of the antibodies tested, there were still an adequate number of successful markers for different cell types in each tissue to justify downstream data analysis and confront the challenges therein. In MCD viewer, multiple markers with nonconclusive staining results were also exported with the primary markers to see how their incorporation would affect the core tSNE/phenograph analysis. The first and often primary challenge in IMC data analysis is cell segmentation. Fluidigm suggests that Hyperion users start with the default/automatic settings in the IdentifyPrimaryObjects module (using a expected nuclei diameter range of 5-15 pixels), so this was tested first. Although this appeared to work reasonably well for lung alveoli, where epithelial nuclei of ATI/II cells are fairly well-separated, the epithelial nuclei in the mammary ducts are small and tightly packed together, making them difficult to segment. Indeed, many iterative adjustments of the various segmentation parameters such as min/max diameter, thresholding method, and threshold correction factors failed to successfully partition the two mammary cell types in regions of high DNA staining intensity. The only parameter recommended by Fluidigm to be adjusted from its default value is actually not located in the IdentifyPrimaryObjects module at all, but rather in the ImageMath module, where it is suggested to multiply the DNA image by a factor of 50 before using it to identify nuclei. Manipulation of this factor did not improve cell segmentation since it scales the pixel intensities proportionally and the *relative* difference in pixel intensities is utilized by thresholding algorithms. However, right next to this multiplication operator in ImageMath is an *exponential* operator, that raises the intensities of the pixels to the specified power. When this transformation was applied to the DNA images, significantly better segmentation was observed in the mammary ducts (Figure 5.3.2C).
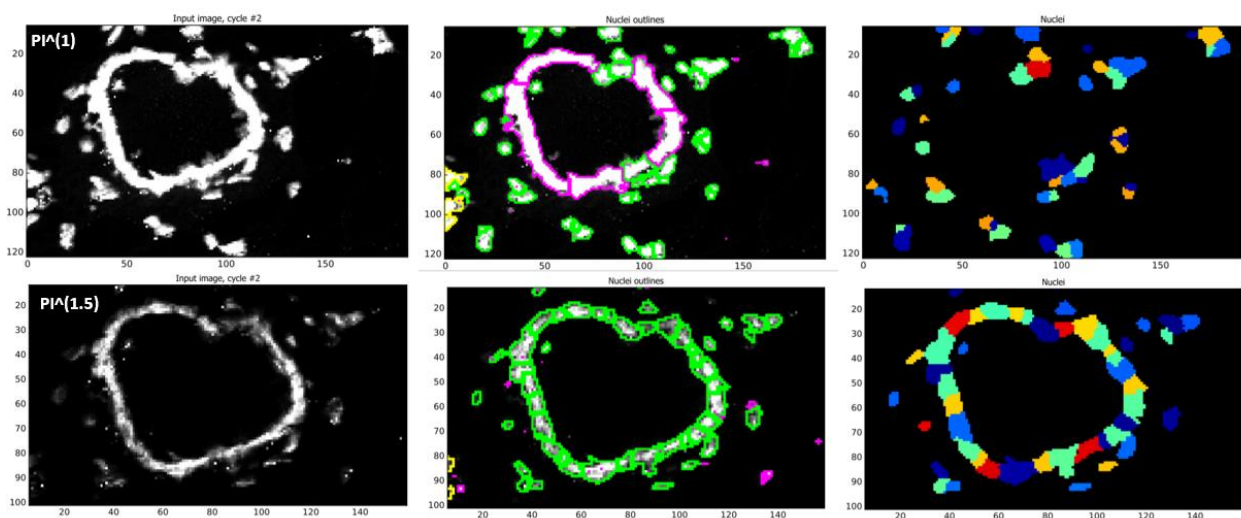
Figure 5.3.2C: Cell segmentation of mammary duct cells with or without exponential transformation of the DNA image. Segmentation of the untransformed DNA image (top) results in the inability to segment the majority of the epithelial cells in the mammary duct using many thresholding settings, resulting in large objects (purple) that are discarded because they are outside of the accepted size range. Raising the pixel intensity to a power of 1.5 (bottom) significantly enhances segmentation of these cells (green, accepted objects) while maintaining the ability to identify most of the dimmer cells outside of the duct. Data generated in CellProfiler.

Although some untested algorithmic manipulation may also accomplish this, an immediate solution was found to the cell segmentation problem using this transformation and was applied to future experiments where segmentation was an issue.

After generating an acceptable cell mask for the mammary and lung IMC images, they were imported into HistoCAT. From here, phenograph clustering was performed on all cells in a given tissue type using all imported markers and the default settings, and the quality of the clusters, and subsequently the staining, was evaluated. The results for lung are shown in Figure 5.3.2D.
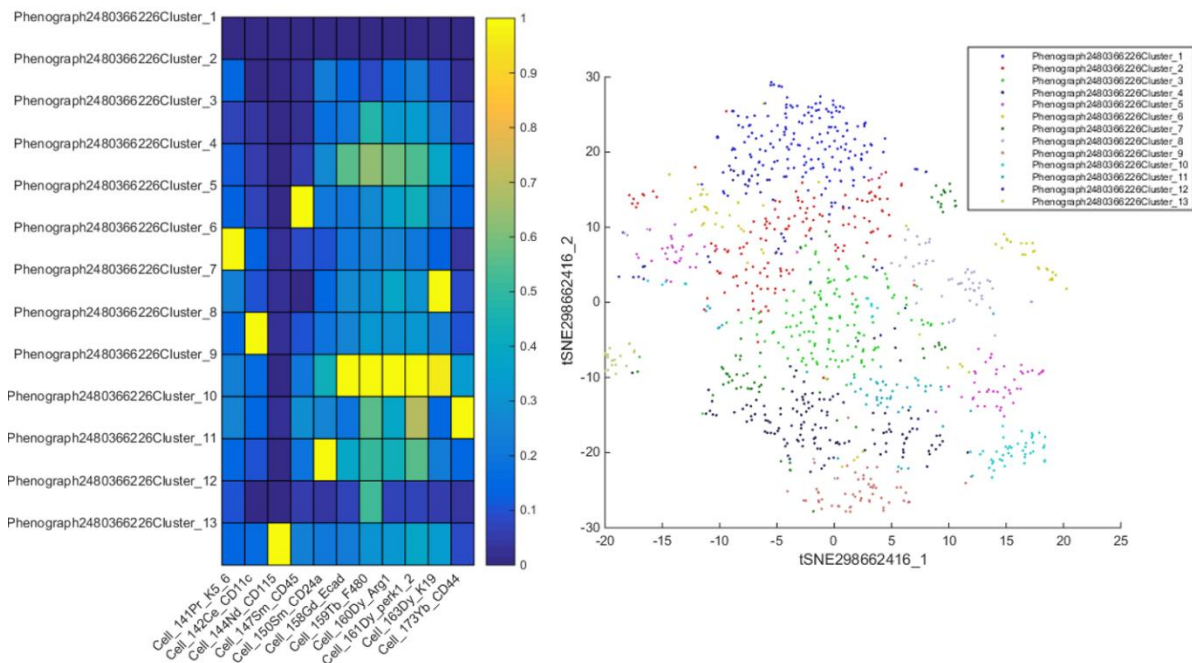

Figure 5.3.2D: HistoCAT analysis of FFPE lung tissue. Phenograph cluster heatmap (left) lists clusters (rows) from highest to lowest occurrence with their relative marker expression (columns). tSNE scatterplot (left) with phenograph clusters highlighted in different colors. Data generated in HistoCAT.

In the lung IMC staining analysis, none of the most populated clusters (top of the heatmap) showed distinct staining for any of the markers used in the analysis. Plotting all clusters on a tSNE scatterplot showed minimal distinction between the clusters. Many of the lower frequency clusters were highly positive for a single marker, indicating the presence of high-intensity antibody antibody aggregate pixels in these cells. Cluster 9 showed maximal intensity for many markers that should not be coexpressed in any cell type, indicative of antibody aggregation to dust particles. These aggregate properties were confirmed by re-examining the different channel images in MCD Viewer. When taken together, this indicated that the quality of data was quite low for this sample.

The mammary analysis is shown in Figure 5.3.2E. Here, it was clear that the clusters correlated to the expected basal and luminal cell types that comprised the majority of the cells in the image. This was physically confirmed by mapping the clusters back to the image.
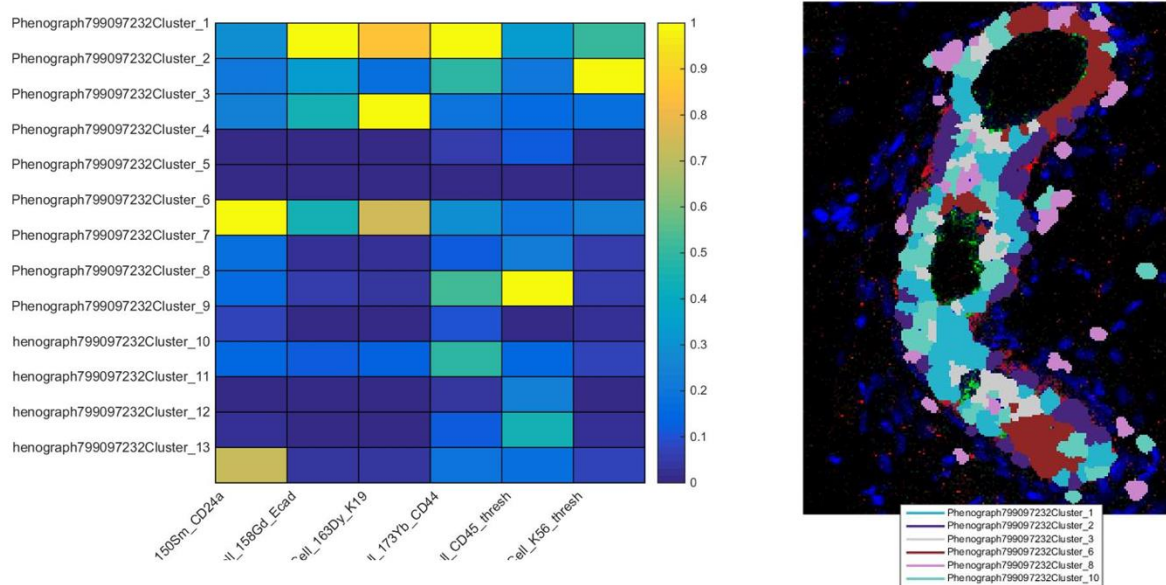

Figure 5.3.2E. Clustering and analysis of mammary IMC images. Phenograph cluster heatmap (left) lists clusters (rows) from highest to lowest occurrence with their relative marker expression (columns). Notable clusters (positive for a distinct combination of markers) were mapped back to the tissue ROIs (representative image of WT mammary duct ROI shown).

From the analysis, cluster 1, 3, and 10 are indicative of luminal cells, while cluster 2 represents myoepithelial cells, and cluster 10 denotes CD45+ immune cells. Cluster 6 may represent a unique subset of luminal cells based on their high CD24 expression. However, not enough cells (only 3 ducts per tissue) were analyzed to make a statistically significant comparison between the cluster frequencies in the Axl WT and KO mammary glands, and the quality of segmentation, although significantly improved, was still not entirely trustworthy. However, this "round-trip" analysis of clustering cells based on their staining intensities for each marker followed by visualizing them on the image proved to be a useful method to determine the relative success of staining, segmentation, and analysis.

5.3.3 Run 3: FFPE tumor, kidney and spleen

In the prior run, it was difficult to determine if an antibody failed because it wasn't suited for FFPE tissue or due to the lack of positive cells in any of the ROIs selected on the tissue. Therefore, other tissue types containing a broader diversity of cell types (particularly immune cells) were tested with a similar panel as before, including FFPE kidney, spleen, and 4T1 subcutaneous tumor samples. A list of all antibodies used in the cocktail and their staining results is shown in Table 5.3.3.

conjugate	Target	Protein/cell type	Cellular location	Clone #	Supplier	Product #	Pre-stain Conf. Score	Reason	Cocktail Conc. (µg/mL)	staining result	If (+), which tissues, if (-)/NC, poss. reasons	staining issues (if any)
141Pr	K5/6	basal/MEP marker	CS	D5	millipore	MAB1620	3	PT-S	10.0	++	tumor	NCA
142Nd	CD11c	DCs, NK cells, some activated T cells	MEM	N418	Fluidigm	3142003B	1	PT-NC	4.5	NC	NSB	DA++
144Nd	CD115	monocytes, macs, EpC, tumors	MEM	AFS98	Fluidigm	3144012B	1	PT-NC	10.0	-		
145Nd	CD4	Helper T cells	MEM	RM4-5	Fluidigm	3145002B	2	UV/LIT	5.0	-	CTL	
146Nd	CD8a	Cytotoxic T cells	MEM	53-6.7	Fluidigm	3146003B	2	LIT	10.0	-	CTL	DA
147Sm	CD45	Immune Cells	MEM	30-f11	Fluidigm	3147003B	3	PT-W	5.0	+		CTL
148Nd	PD-1	activated T/B lymphocytes	MEM	RMP1-30	Thermo	14-9981-82	1	PT-NEG	10.0	-		
149Sm	CD83	mature DCs	MEM	Michel-17	Thermo	14-0831-82	1	PT-NEG	10.0	+	tumor	DA/CTL
150Nd	CD24(a)	LPC & MPC	GR	M1/69	Fluidigm	3150009B	3	PT-S	5.3	++	tumor/spleen/kid	
151Eu	CD64	monocytes, macs, DCs	MEM	X54-5/7.1	Fluidigm	3151012B	1	PT-NEG	5.0	NC	NSB	CTL
152Sm	CD3e	T cells	MEM	145-2C11	Fluidigm	3152004B	2	UV	5.0	-		
153Eu	PD-L1	Immune checkpoint inhibition	LIG	10F.9G2	Fluidigm	3153016B	2	SSA	10.0	+	tumor	NCA
154Sm	Vimentin	mesenchymal marker	CS	D21H3	Cell signaling	5741	3	HVA	5.0	++	tumor/spleen/kid	DA
155Gd	FAT4	Hippo pathway	CYT	polyclonal	Bodenmiller	NA	1	NI	5.0	-		
156Gd	CD103	intra-Ep lymphocytes, binds E-cad	MEM	"2e7"	Thermo	14-1031-85	1	PT-NEG	10.0	-		
158Gd	E-cadherin	Epithelial marker	MEM	"24E10"	Fluidigm	3158021A	3	PT-S	10.0	++	tumor/spleen/kid	
159Tb	F4/80	macrophages	MEM	BM8	Fluidigm	3159009B	2	LIT	10.0	NC	NSB	
160Gd	Arginase-1	M2a macrophages	CYT	polyclonal	Novus Bio	NBP1-32731	2	PT-NC/LIT	10.0	+	tumor/spleen/kid	DA/NSB
162Dy	Ly6C	memory T cells, monocytes	MEM	HK1.4	Fluidigm	3162014B	2	PT-NC/LIT	5.0	-		
163Dy	CD40	B cells, DCs, Monocytes, macs, endo	MEM	1C10	RnD	MAB440-100	1	NI	10.0	-		DA
164Dy	CD49b	regulatory T cells	MEM	HMa2	Fluidigm	3164011B	1	PT-NEG	5.0	NC	CTL, NSB	NCA
167Er	YAP	Hippo pathway	CYT	H-9	santa cruz biotec	sc-271134	1	PT-NC	3.3	+	tumor/spleen/kid	NCA/NSB
168Er	CTLA4	Immune checkpoint inhibition	MEM	UC10-4B9	Thermo	14-1522-82	1	PT-NEG	10.0	-		DA
169Tm	CD206	M2a macrophages	MEM	C068C2	Fluidigm	3169021B	1	PT-NEG	10.0	-		NCA
170Er	MerTK	macrophages, DCs	MEM	polyclonal	RnD	AF591	2	SSA	10.0	+		DA+, CTH
171yb	CD80	active DCs, monocytes, macs	MEM	16-10A1	Fluidigm	3171008B	1	PT-NEG	5.0	NC	NSB	NCA
172Yb	CD86	early active DCs, monocytes, macs	MEM	GL1	Fluidigm	3172016B	1	PT-NEG	5.0	-		
173Yb	CD44	cancer stem cell marker, basal cells	MEM	IM7	Fluidigm	3150018B	3	HVA	5.0	++	tumor/spleen/kid	
174Yb	Ly6G/C	polymorphonuclear neutrophils	MEM	RB6-8C5	Fluidigm	3174008B	2	UV/LIT	10.0	-	CTL	
175Lu	pHistone H3	proliferation	NUC	HTA28	Fluidigm	3175012A	3	HVA	5.0	++	tumor/spleen/kid	
176 Lu	Axl	Stemness, immune evasion	MEM	107332	RnD	MAB8541	2	PT-NC/LIT	10.0	NC	NCA	

Table 5.3.3: List of antibodies used in Run 3. Cellular location refers to what part of the cell the marker should be found. LIG, ligand (cytosolic or extracellular); EC, extracellular; CS, cytoskeleton; CYT, cytosolic; MEM, membrane. The staining confidence score is on a scale of 1-3. Reasons behind the confidence score are: NI, no indication; LIT, from the literature; UV, Hyperion user-validated; SSA, supplier-suggested application; HVA, Hyperion-validated antibody; PT-S/W/NC/NEG, previously tested—strong/weak/non-conclusive/negative staining. For markers that did not show positive staining, possible reasons include: CTNP, cell type not present; NSB, non-specific binding; CTL, concentration too low. Staining issues include: DA, direct aggregate (from antibody in channel); NCA, neighboring channel aggregate. "+" signs indicate the issue is more pronounced (2-fold increase per "+" sign). Refer to the HUGO guidelines for all marker abbreviations.

Serial H&E images were again used to select ROIs for ablation, and are shown in Figure 5.3.3A and B.
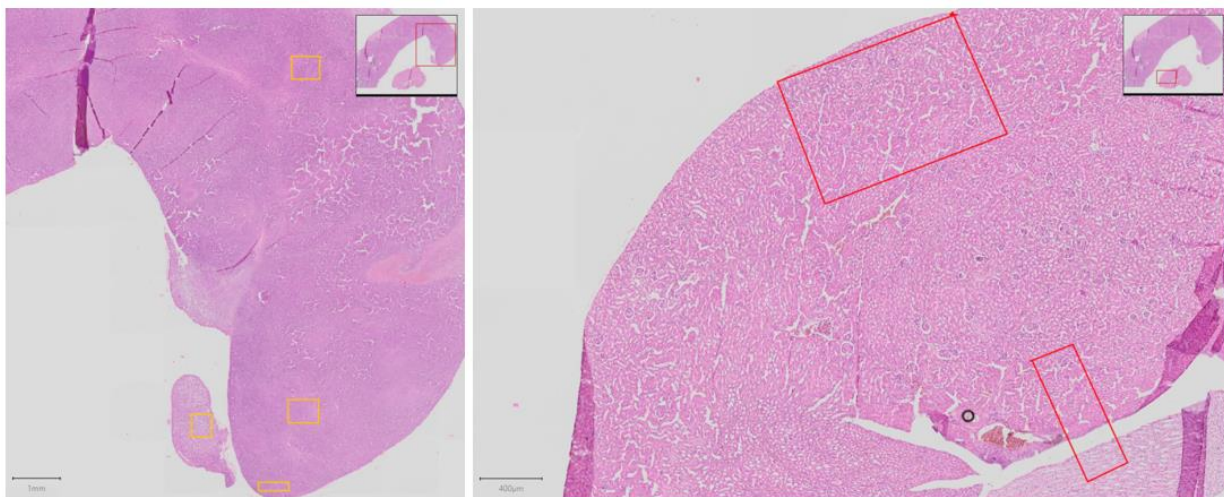

Figure 5.3.3A: ROIs selected for IMC ablation and analysis from serial H&E images of kidney and spleen. Highlighted regions roughly approximate the ROIs chosen in IMC. Left: spleen. Right: Kidney.
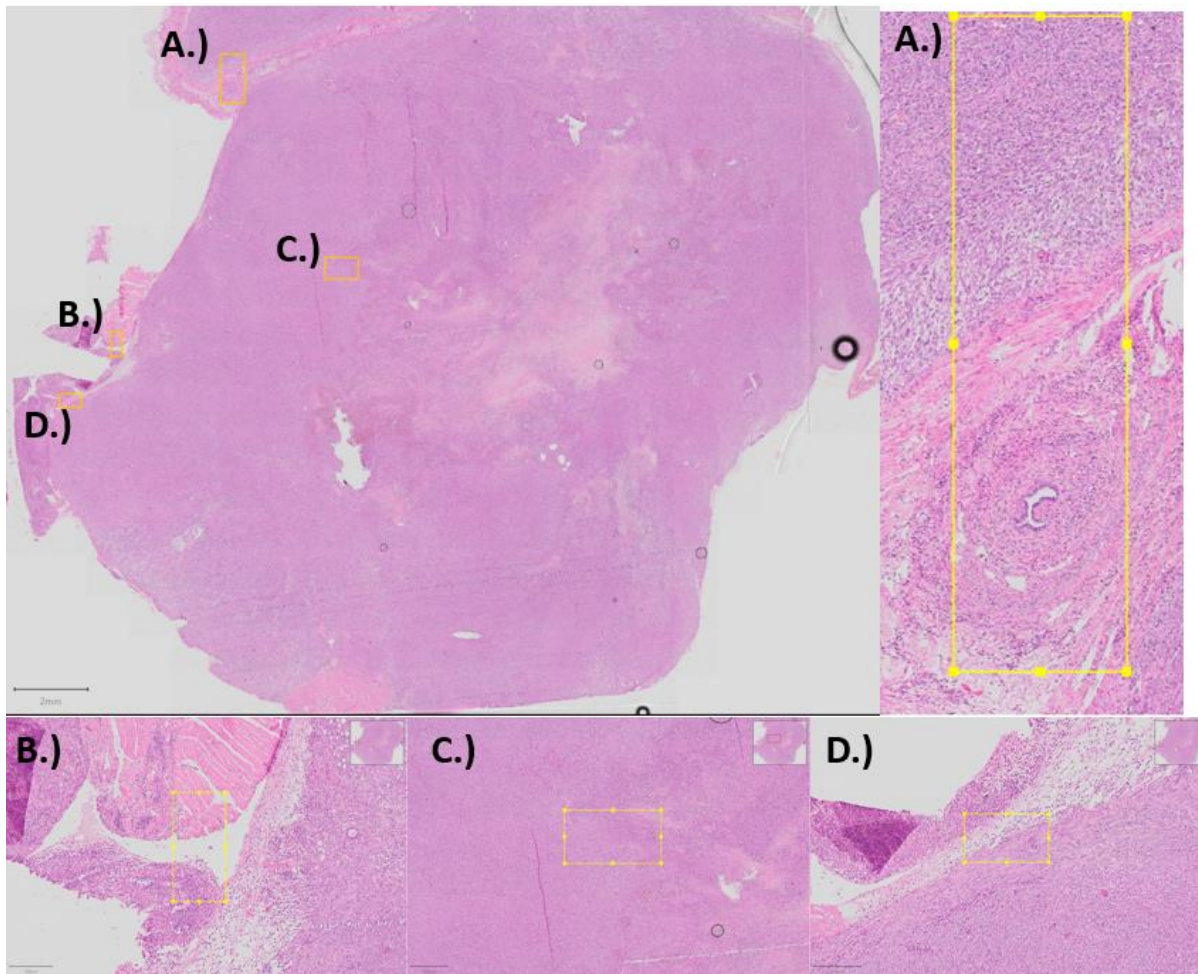
Figure 5.3.3B: ROIs selected for IMC ablation and analysis from serial H&E images of syngeneic 4T1 breast cancer tumor. Highlighted regions roughly approximate the ROIs chosen in IMC. (A) tumor layers. (B) muscle, gland, and tumor. (C) necrotic border. (D) boundary between gland and tumor.

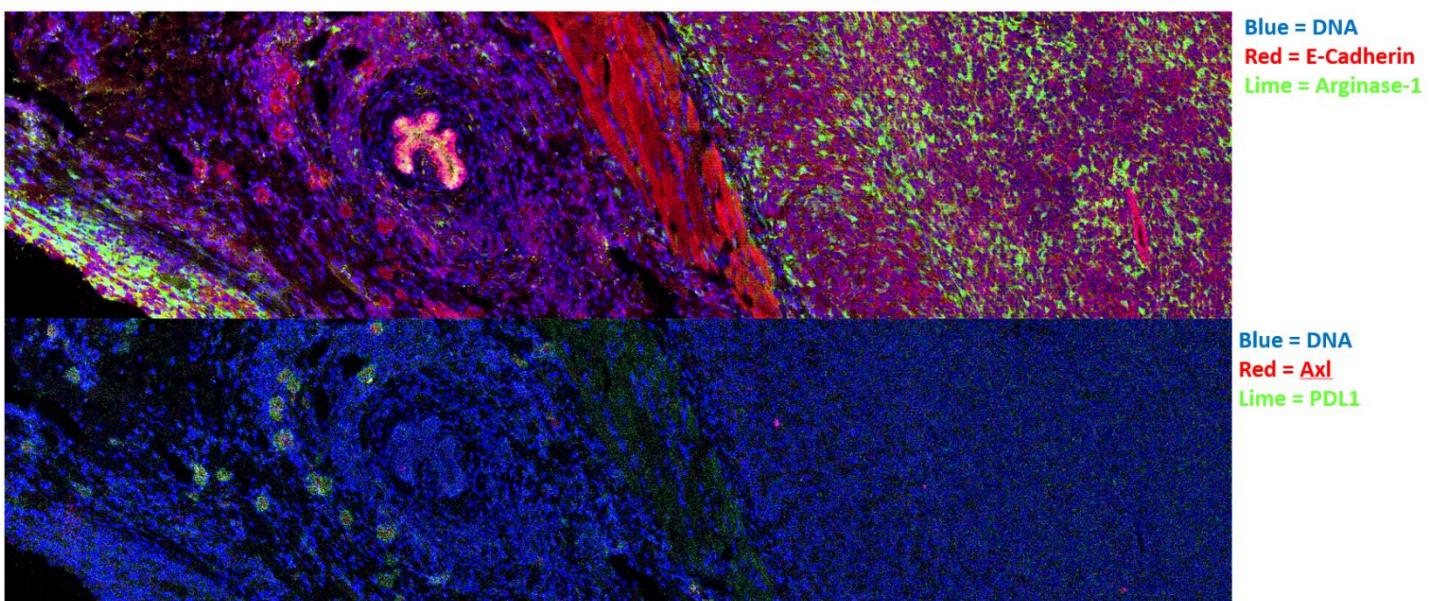Representative images of notable marker combinations in each tissue are shown in Figure 5.3.3C, D, and E.

Figure 5.3.3C: IMC images of notable markers at the boundary of a mouse 4T1 subcutaneous tumor.

DNA CD24a Arg-1

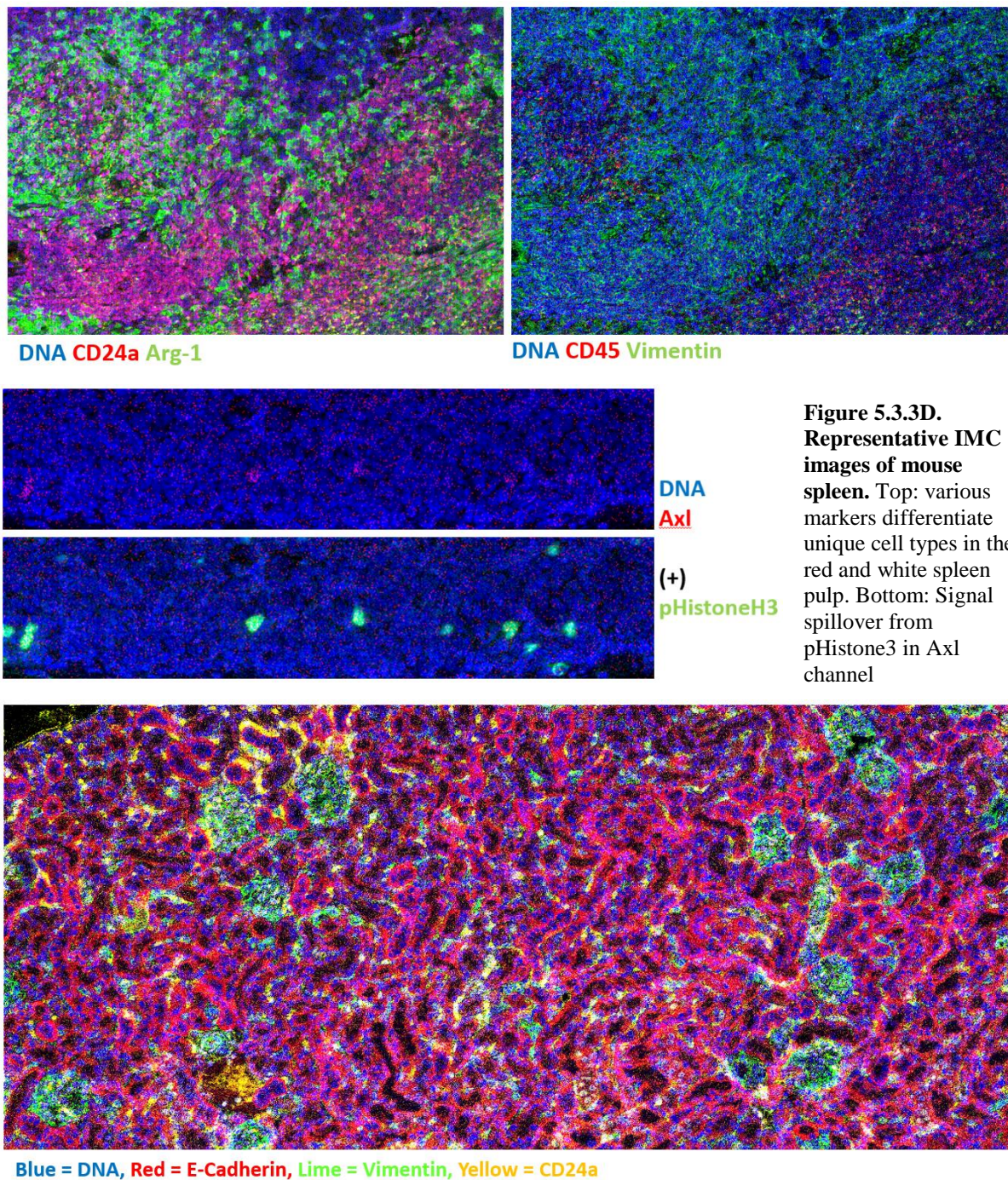DNA CD45 Vimentin

DNA
Axl

(+)
pHistoneH3

Figure 5.3.3D. Representative IMC images of mouse spleen. Top: various markers differentiate unique cell types in the red and white spleen pulp. Bottom: Signal spillover from pHistone3 in Axl channel

Blue = DNA, Red = E-Cadherin, Lime = Vimentin, Yellow = CD24a

Figure 5.3.3E: Representative IMC staining of mouse kidney. Numerous glomerular structures visible in the kidney cortex.

Since the Axl antibodies had exhibited varied staining results in prior runs and represent an important component in the IMC panel, a specific emphasis was placed on determining the quality of Axl staining in these tissues, using only one anti-Axl clone. Some Axl+ cells were noticed in the spleen, however this staining was found to result from neighboring channel

spillover (NCS) from very strong pHistoneH3 staining, and was the first time this phenomenon was noticed on the Hyperion. Axl/PD-L1+ cells were also found at the 4T1 tumor boundary that were not the result of NCS. To see if the Axl and PD-L1 staining could distinguish these cells in their own phenograph cluster, a "roundtrip analysis" was performed specifically on the ROI containing these cells, and is shown in Figure 5.3.3F. Default settings in the CellProfiler segmentation pipeline were sufficient in this tissue type.
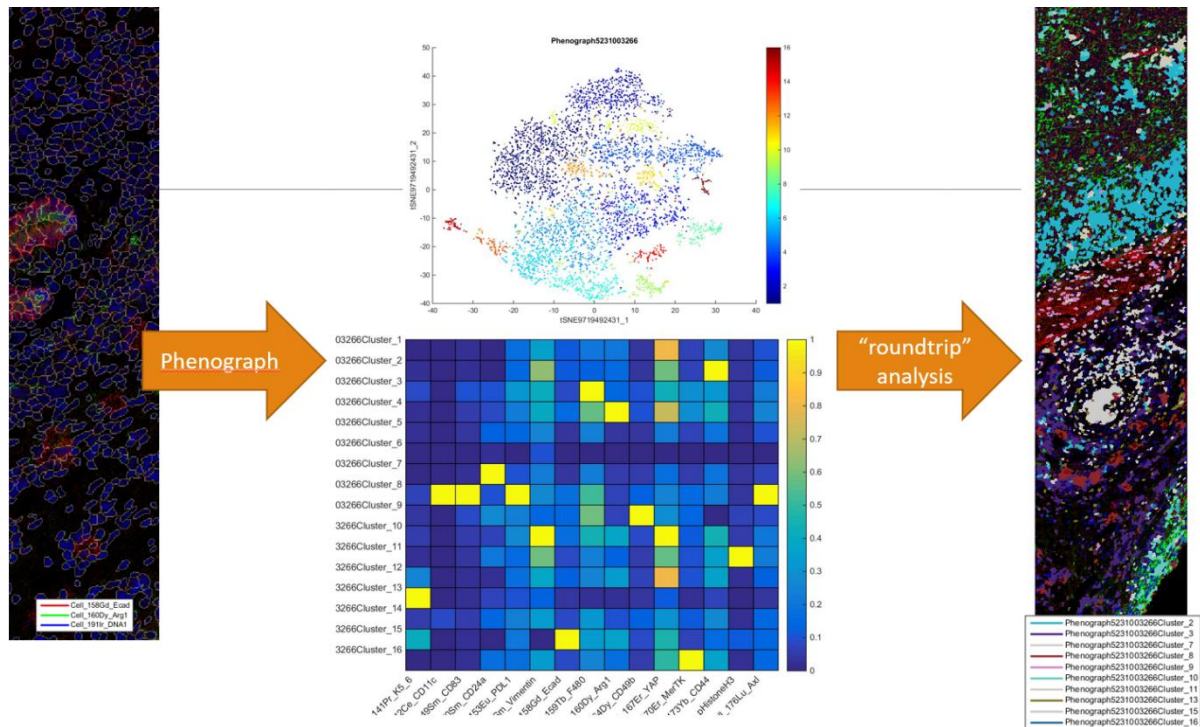

Figure 5.3.3F: Roundtrip analysis on 4T1 tumor ROI. Cell mask (left) and accompanying multiplex images are loaded into HistoCAT. Phenograph clustering is performed on all cells in the sample to produce a heatmap of cluster expression levels (bottom), and clusters are mapped onto a tSNE plot (top) of single cells to observe their relative similarity. Clusters of interest are then chosen to be mapped back onto the sample image (left).

Indeed, a unique Axl/PD-L1+ cluster was identified by phenograph and mapped back to the original cells spotted in the image. Additionally, more cells from the same cluster not initially noticed during visual inspection of the images were found to be deep in the tumor stroma (red-labeled cells in left image of Figure 5.3.3F). These cells were also positive for both CD11c and CD83, indicating that these cells were activated dendritic cells.

5.3.4 Run 4: FFPE lung, mammary gland and organoids

With the arrival of pre-conjugated and validated FFPE antibodies from Fluidigm, tissue specific markers that were conjugated in-house, and a backbone of pre-tested antibodies from our existing inventory, it was time to revisit the Axl WT/KO lung and mammary glands with the added sample type of organoids derived from mammary glands from these mice. A list of all antibodies used in the cocktail and their staining results is shown in Table 5.5.3.

Heavy metal tag	Target	Cellular Process / Phenotype / Purpose	Cellular Location	Antibody Clone ID	Vendor	Product #	Pre-stain Conf. Score	Reason	Cocktail Conc. (µg/m	staining result	If (+), which tissues, if (-)/NC, poss.	staining issues (if any)
89Y	CD45	Immune cells	MEM	30-f11	Fluidigm	3147003B	2	UV/PT-NC	7.5	-	see legend*	
141Pr	K5/6	MEP	CS	D5/16B4	Millipore	MAB1620	3	PT-S	10	++	mam/org	DA
143Nd	alpha-sma	myofibroblasts, VSMCs, MEP	CS	1A4	ThermoFisher	14-9760-82	2	SSA	5	++	mam/org/lung	CTH+++
145Nd	pan-laminin	basement membrane	ECM	polyclonal	ThermoFisher	PA1-16730	2	SSA	10	+	lung/org	NSB?
146Nd	CD31	vessels	MEM	390	ThermoFisher	14-0311-82	2	SSA	10	-	NEG	NCS
147Sm	SOX-9	lung morphogenesis, MaSC fate	TF	EPR14335	Fluidigm	3147022D	3	HVC	10	++	mam/org	NCA
148Nd	pan-keratin	epithelial marker	CS	C11	Fluidigm	3148020D	3	HVC	5	+	lung/mam	NSB/DA
150Nd	CD24(a)	LPC & MPC	GR	M1/69	Fluidigm	3150009B	2	PT-W	10	+	lung/mam	CTH
151Eu	p63	Basal TF	TF	polyclonal	Abcam	ab53039	2	SSA	10	+	lung/mam/org	CTH+
152Sm	CD3e	T cells	MEM	145-2C11	Fluidigm	3152004B	2	UV/PT-W	5	-	CTNP?	
154Sm	Vimentin	mesenchymal marker	CS	D21H3	Fluidigm	3154014A	3	HVC	5	++	lung/mam/org	CTH+
156Gd	p38	stress signaling, Lgr6+ LMPC	TF	D3F9	Fluidigm	3156002A	2	UV	5	+	lung/mam/org	NSB?
158Gd	E-cadherin	epithelial marker, segmentation	MEM	24e10	Fluidigm	3158021A	3	PT-S	10	++	lung/mam/org	CTH
159Tb	F4/80	pan-macrophage	MEM	BM8	Fluidigm	3159009B	1	PT-NC	5	-	NEG	NSB
160Dy	Arginase-1	M2a macrophages	CYT	polyclonal	Novus Bio	NBP1-32731	2	PT-S	3.3	+	lung	DA++
161Dy	Ki67	proliferation	Nucleus	B56	Fluidigm	3172024B	2	UV/HVC	10	++	lung/mam/org	
162Dy	Lgr5	stem cell marker in mam/lung	MEM	polyclonal	Abcam	ab75732	2	SSA	10	-	NSB	
165Ho	Beta-catenin	Wnt signaling/adhesion	CYT	D13A1	Fluidigm	3165032D	3	HVC	5	++	lung/mam/org	CTH
166Er	CD19	B cells	MEM	6D5	Fluidigm	3166015B	1	PT-NC	5	-	CTNP?	
168Er	CD29 (ITGB1)	Basal cell ECM adherence, MaSCs	MEM	3B6	ThermoFisher	MA5-17103	2	SSA	2.6	+	lung/mam	CTL/NCA
169Tm	Collagen-1	ECM deposition, fibrosis	ECM	polyclonal	Fluidigm	3169023D	3	HVC	2	++	lung/mam	CTH
171Yb	pErk1/2	signaling	CYT	D13.14.4E	Fluidigm	3171010A	2	HVA	5	++	lung/mam/org	NSB
172Yb	Cleaved caspase 3	apoptosis	CYT	5A1E	Fluidigm	3172027D	3	HVC	10	++	org	NSB
173Yb	CD44	EMT, lymphocyte activation	MEM	IM7	Fluidigm	3150018B	3	PT-S	5	++	lung/mam/org	NSB mam
174Yb	CD18 (ITGB2)		MEM	M18/2	ThermoFisher	14-0181-82	2	SSA	10	-	NSB	NCS
175Lu	Pan-Actin	structural marker for segmentation	CS	D18C11	Fluidigm	3175032D	3	HVC	10	++	lung/mam/org	CTH+
176Lu	Axl	Stemness, immune evasion	MEM	175128	R&D Systems	MAB854	2	PT-W	15	-	ARMM	NCS+
MAMMARY COCKTAIL ONLY												
164Dy	K7	luminal marker	CS	RCK105	Fluidigm	3164028D	3	HVC	10	+	mam/org	CTL
170Er	K14	myoepithelial marker	CS	polyclonal	ThermoFisher	PA5-13672?	1	NI	2.5	-	NSB	
LUNG COCKTAIL ONLY												
149Di	SFTPC	Lung secretory cells (mainly AT2)	MEM	polyclonal	ThermoFisher	PA5-76631	2	SSA	3	++	lung	CTH
164Dy	CD34	microvascular endothelial cells	MEM	MEC 14.7	Novus Bio	NB600-1071	2	supplier rec'd	10	++	lung	CTH
170Er	MerTK	macrophages, DCs	MEM	polyclonal	R&D Systems	AF591	1	ested, nonsp	5	+	lung	DA+++

Table 5.3.4: List of antibodies used in Run 5. Cellular location refers to what part of the cell the marker should be found. LIG, ligand (cytosolic or extracellular); EC, extracellular; CS, cytoskeleton; CYT, cytosolic; MEM, membrane. The staining confidence score is on a scale of 1-3. Reasons behind the confidence score are: NI, no indication; LIT, from the literature; UV, Hyperion user-validated; SSA, supplier-suggested application; HVA, Hyperion-validated antibody; PT-S/W/NC/NEG, previously tested—strong/weak/non-conclusive/negative staining. For markers that did not show positive staining, possible reasons include: CTNP, cell type not present; NSB, non-specific binding; CTL, concentration too low. Staining issues include: DA, direct aggregate (from antibody in channel); NCA, neighboring channel aggregate; NCS, neighbor channel spillover. "+" signs indicate the issue is more pronounced (2-fold increase per "+" sign). Refer to the HUGO guidelines for all marker abbreviations.

No guiding H&E images were required since large crossections taken from the lung sections and mammary ducts and organoids could be easily visualized and targeted for ablation on the Hyperion-acquired sample panorama. Representative images of notable marker combinations are shown in Figure 5.3.4A.
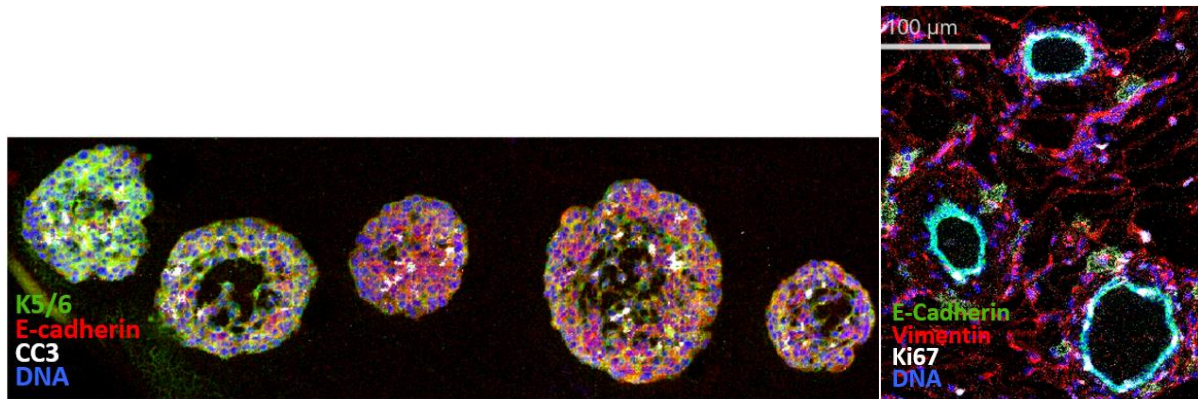

E-Cadherin Alpha-SMA DNA Collagen-1
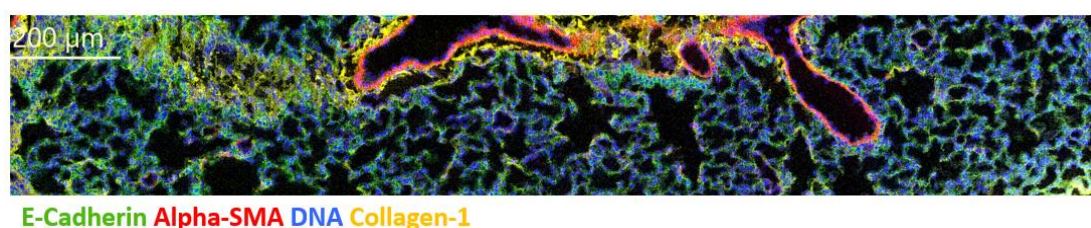
Figure 5.3.4A: Representative images of IMC staining in Axl WT lung (top), Axl+ mammary cell-derived organoids (bottom left), and WT mammary gland (bottom left).

With the addition of FFPE-validated and supplier-suggested antibodies, the number of markers exhibiting adequate or excellent staining was significantly higher than in any other experiment. However, several antibodies from the existing inventory were long past their shelf life and had developed aggregates during storage. These single high intensity pixels were highly undesirable in previous runs since they severely skewed the clustering analysis. Dealing with the high-outlier pixels by gating them out in HistoCAT was also a suboptimal method. Therefore, if these aggregate-containing channels were to be included in the analysis, a method had to be devised to eliminate them using image preprocessing in CellProfiler. Typically, to remove noise a threshold is applied to an image. However, these thresholding algorithms were designed to remove background noise from fluorescent images, not to remove high-outlier pixels like those encountered in IMC. Various inverse manual thresholding techniques were attempted in CellProfiler to try to eliminate these pixels, but were not scalable to batch image processing since they would over-threshold some images and under-threshold others when optimized for a single image (Figure 5.3.4B).
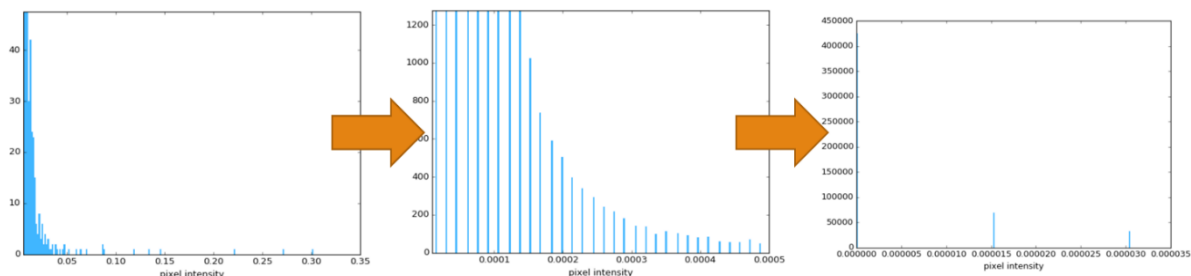

Figure 5.3.4B: Thresholding strategies cannot consistently remove outlier pixels resulting from aggregates in IMC images. The unprocessed image pixel intensity histogram of a representative MerTK IMC image containing high-outlier pixels. (left) Y-axis extends to 70,000 pixels but is cut off to visualize ultra-low occurring pixels. When manual threshold settings are optimized for this image, all of the outliers can be removed without discarding any stained pixels (middle). When the same algorithm is applied to the MerTK image from another ROI, the intensity cutoff is too low, resulting in the loss of many informative pixels (right).

Therefore, a different strategy was employed known as median filter smoothing (Figure 5.3.4C), which is ideal to eliminate discrete outlier pixels known as "salt-and-pepper" noise.
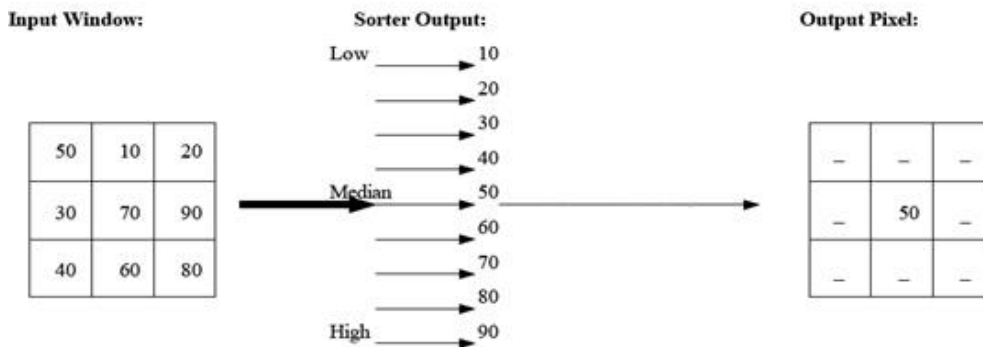

Figure 5.3.4C: Schematic of median filter smoothing. The values of all pixels within a specified diameter around the pixel being analysed are analysed for their median, which is assigned to the central pixel. This is repeated for all pixels in an image. Taken from [70].

When applied to the aggregate-containing images with an appropriate filter diameter (only 3-5 pixels due to the single-pixel nature of the aggregates), all aggregates were removed and the general shape of the positive cellular staining patterns was maintained for all ROIs in the batch of IMC images (Figure 5.3.4D). This was applied to all aggregate-containing channels.
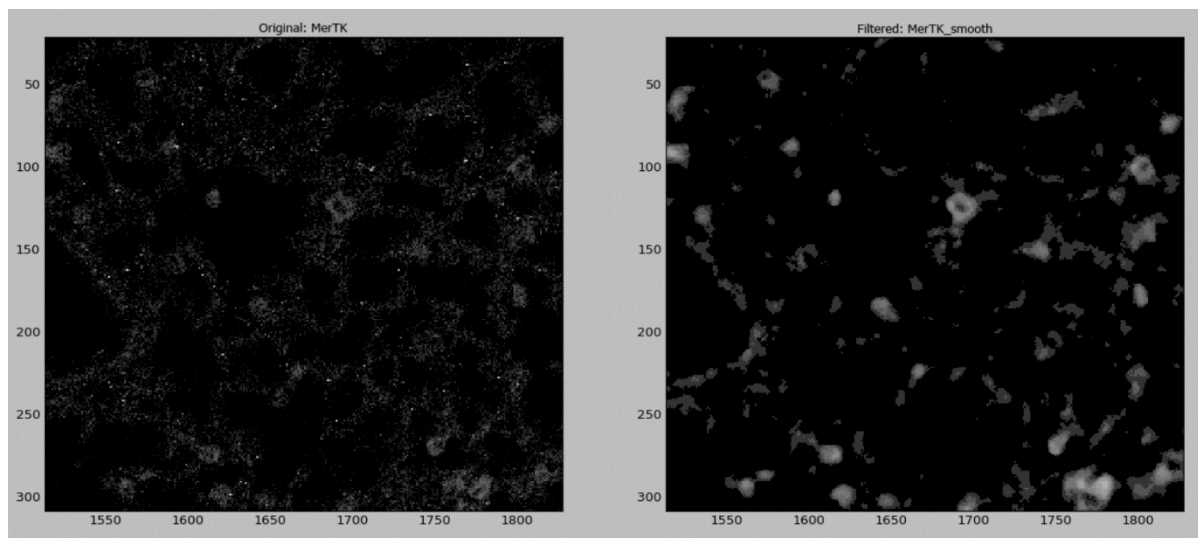

Figure 5.3.4D: Median filter smoothing applied to remove high-intensity aggregates from IMC images. (left) MerTK image before processing with log-normalized pixel intensity to simultaneously visualize the aggregates and positive cellular staining in the image. (right) image after median filter smoothing, where cell staining pattern is maintained but outliers are completely removed.

Next, visual inspection of pan-structural marker staining revealed that these channels were likely sufficient to incorporate into cell segmentation. These images were summed using ImageMath in CellProfiler into a "cellular image", which was used as the input image in IdentifySecondaryObjects (Figure 5.3.4E). This function, when set to "propagate" mode, identified cell boundaries based on the staining intensity of the combined cellular marker

image and segmented these outlines into cell objects based on the location of the nuclei objects previously identified using the DNA image. This resulted in a more morphologically accurate cell mask for the irregularly shaped lung alveolar epithelium (Figure 5.3.4F) but did not have a significant effect on the small and densely-packed cells in the mammary ducts (data not shown). Importantly, the advantage of this segmentation technique was only realized with the cellular image was square-root transformed (raised to a power of 0.5), otherwise the intensity of the "cellular" image is too high around the nuclei and doesn't indicate the distant cytoplasm which is stained less intensely.
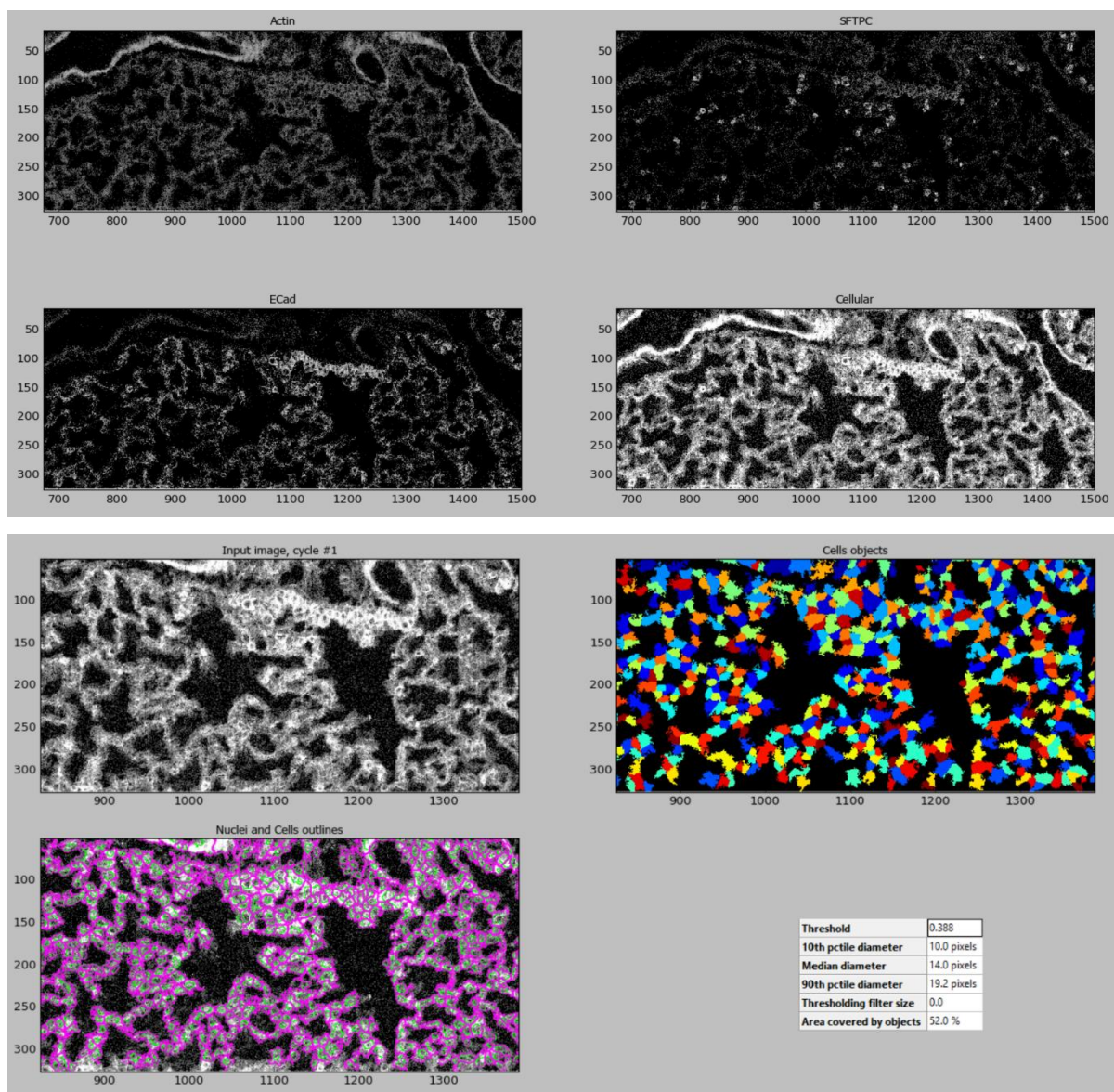

Figure 5.3.4E&F: Segmentation of cells using pan-structural markers in CellProfiler. (E) images staining cytoplasm of all cells or specific subsets of cells are summed into a single "cellular" image, which is square-root transformed to increase the relative signal of distant cytoplasm and (F) applied to cell segmentation.

After these new preprocessing steps, the exported markers from the lung IHC images were ready to be analysed in HistoCAT. Phenograph clustering and visualization of clusters on tSNE showed good separation of clusters (Figure 5.3.4G)
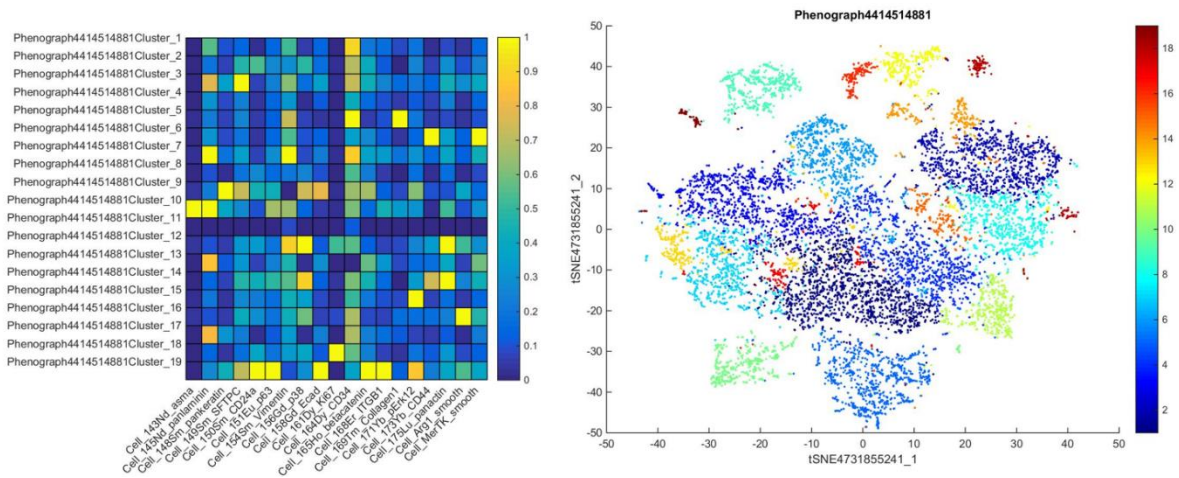

Figure 5.3.4G: Phenograph heatmap (left) and tSNE visualization of clusters from lung IHC images.

Next, the tSNE plots were visualized by condition: Axl WT vs. KO (Figure 5.3.4I)
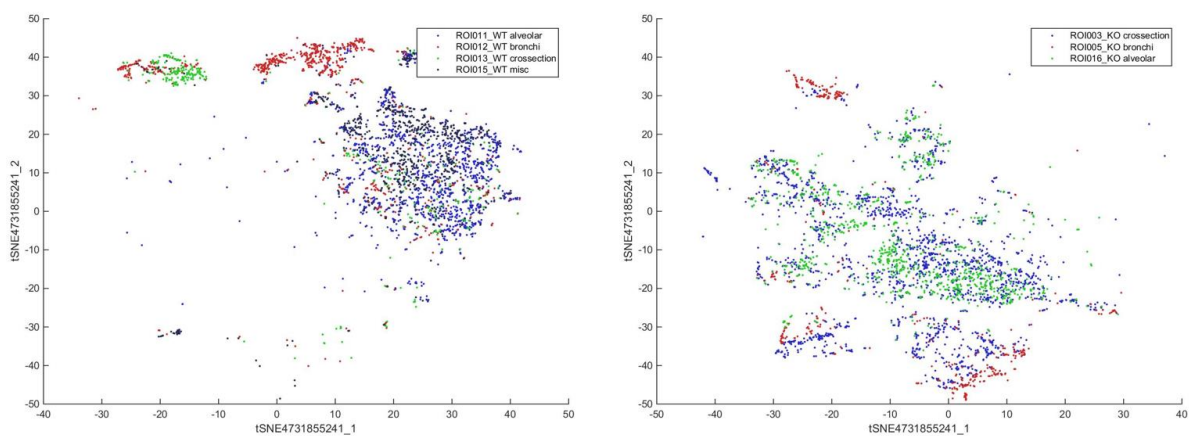

Figure 5.3.4I: tSNE plots of cells from WT (left) and (KO) mice showing different populations of cells present in the alveolar space.

Strikingly, the samples seemed to have entirely different populations of cells. tSNE plots were generated for each channel to determine which markers were most different between the cells from WT and KO lungs (Figure 5.3.4J)
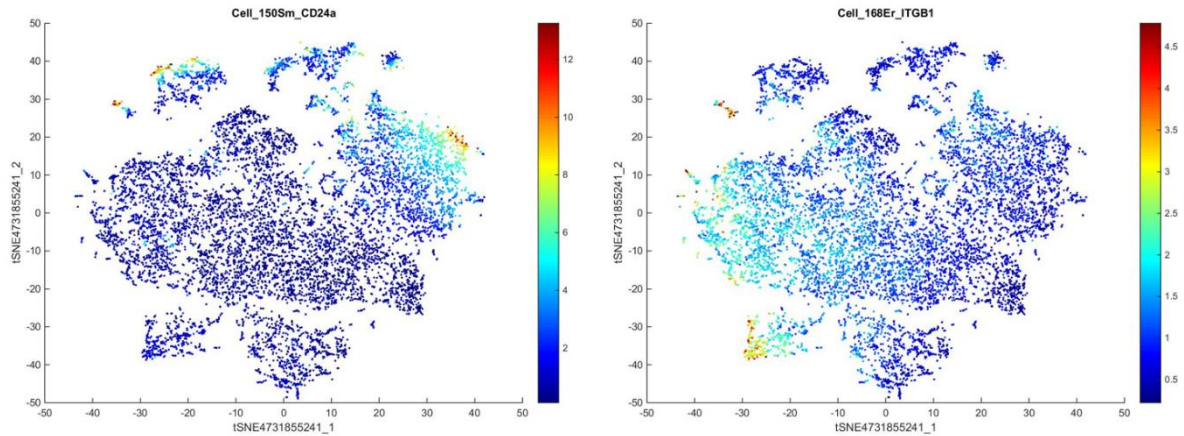
Figure 5.3.4J: t-SNE plots of CD24a and ITGB1 from lung IHC samples.

It was found that the main difference between the mutually exclusive cell populations was influenced the most by CD24a and integrin beta-1 (ITGB1). The differing cell clusters were mapped back onto the images of the WT and KO lungs (Figure 5.3.4K)
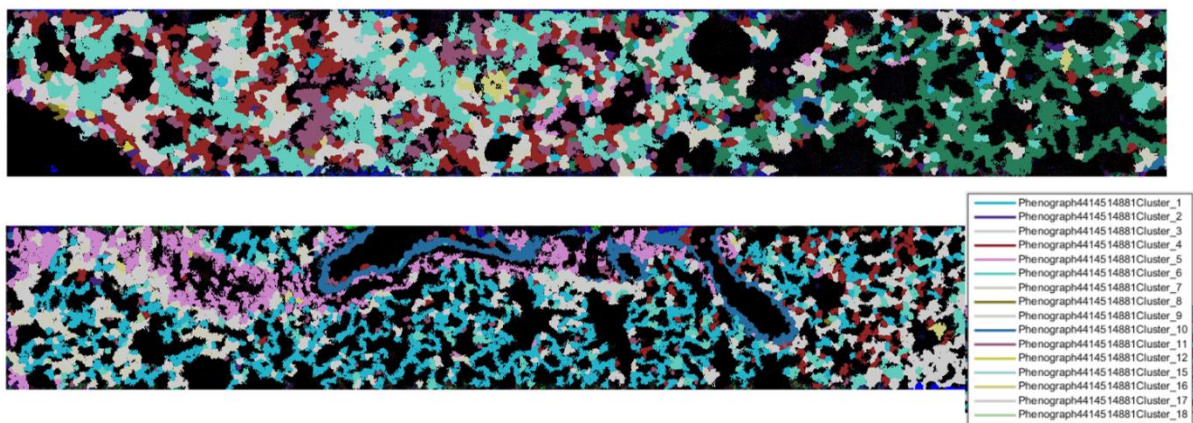
Figure 5.3.4K: Phenograph clusters mapped onto Axl WT (top) and KO (bottom) lung images.

The new panel of markers also worked quite well in the organoids, as compared with the original IF organoid images (Figure 5.3.4L).

Figure 5.3.4L: Axl-LacZ-KO mammary organoid images generated by IF (left) or IMC (right)

It is important to note that the antibodies and samples for Run 5 were obtained only two weeks before the submission of this manuscript, and thus there is still a wealth of information to be obtained from both this data and that of the previous runs.

6. Discussion

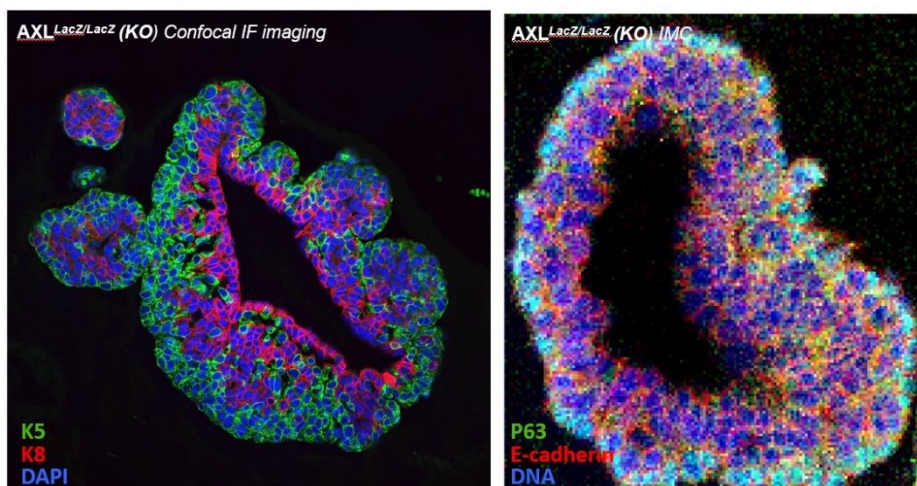The overall aim of this project was to examine Axl's role in cellular plasticity in normal tissues using a unique multifaceted experimental approach comprising genetically engineered mouse systems and high dimensional imaging mass cytometry. The *Axl-CreERT2-GFP* and *Axl-CreERT2-GFP/Rosa26-tdTomato* strains were genotyped, and the *Axl-CreERT2-GFP* strain was established and characterized by various fluorescence-based methods. As the status of the *Axl-CreERT2-GFP/Rosa26-tdTomato* strain was being determined, emphasis was placed on the development of an IMC stem cell panel by running multiple experiments on the Hyperion imaging system, refining the selection of antibodies used in the panel and the downstream image processing and data analysis. This study is the first report on the initiation and testing the UiB Hyperion system, and the Axl murine lineage tracing strain. The discussion therefore focuses on these methodologies and the biological insights gained.

6.1 Mouse Models

6.1.1 Current status of the Axl lineage tracing model

We recently received correspondence from Ozgene stating that it was likely the tdTomato reporter gene had been excised from the *Rosa26* locus in the offspring of the cross between the *Axl-CreERT2-EGFP* strain and the Jackson reporter strain. This was due to the *Axl-CreERT2-EGFP* mice still being heterozygous for the Flp recombinase gene since it was not an anticipated priority for them to conduct additional rounds of breeding to breed out the *Flp* gene, combined with the fact that the tdTomato reporter strain from Jackson Labs was flanked by Flp recognition sites used for reporter silencing when crossbred to other mouse models. As soon as the fertilized *Rosa26-Flp/tdTomato* zygotes from the cross are viable, they begin to express Flp from the *CAG* promoter in one *Rosa26* locus, which permanently excises the *tdTomato* gene from the same locus in the other allele, rendering these mice and their offspring absent of the *tdTomato* reporter. Although some mice from this initial cross may have been *Rosa26-Wt/tdTomato* due to the varying presence of the wild type allele in the *Axl-CreERT2-EGFP* parents, the subsequent inbreeding of the offspring to select for homozygous *Axl-CreERT2-EGFP* mice to send to our group likely introduced the *Rosa26-Flp* allele to all offspring. Although this validates all of our failed genotyping experiments, it was still peculiar

that Ozgene was supposedly able to successfully genotype and maintain the *tdTomato*-containing strain. As it turned out, they had been using a genotyping assay that specifically detected the *Rosa26-Wt* allele and would not amplify any transgenic modifications of that locus. Therefore, they genotyped these mice by simply inferring that they were *tdTomato+* based on the lack of detection of the wild-type allele. Since the *Rosa26* locus still had a modified sequence after Flp-mediation excision of *tdTomato*, it is not detected in this assay. Ozgene has indicated that they will breed out the *Rosa26-Flp* allele from the original *Axl-CreERT2-EGFP* strain at their facility, repeat the *tdTomato* cross, and send us valid lineage tracing mice as soon as possible. However, since we also bred and established the *Axl-CreERT2-EGFP* stock strain already in our group, we could cross it with commercially available *tdTomato* reporter mice ourselves in the interest of time.

6.1.2 The pros and cons of using an external vendor for transgenic mice

There are several advantages to contracting an external company to devise and create a transgenic mouse strain. Their experience in both designing and generating such models, usually associated with a good reputation, means that it is more likely to be successful and time/labor-efficient relative to attempting the same process in-house, if the expertise is even available in a given research group. Additionally, Ozgene in particular uses modern advances in mouse breeding research to increase efficiency. Typically, transgenic ES cells are injected into blastocysts from superovulated wild type mice and the offspring from the resulting male chimeras would be selected based on whether they contain a copy of the knock-in allele, which is a result of random chance that the transgenic ES cell genome is present in any particular sperm cell. However, Ozgene licenses a proprietary strategy (goGermline) which utilizes blastocysts from homozygous *Tsc22d3*-floxed females crossed with homozygous *Rosa26-Cre* males. The resulting blastocysts gain a homozygous *Tsc22d3* knock-out mutation which produces males devoid of any spermatocytes derived from the blastocyst lineage due to a cell-autologous defect in the first meiotic division. The ES cell-derived sperm cells are viable and have no competition, resulting in 100% germline transmission efficiency [57]. Considering that the ratio of blastocyst cells to injected ES cells is quite high, the efficiency of germline transmission using the traditional approach is very low and results in high numbers of collaterally born wild type offspring which are often sacrificed, raising ethical concerns.

Despite these advantages, there are certain practices adopted by high-throughput companies that can have serious consequences in some rare cases, as demonstrated by our experience with the Axl lineage tracing strain. Two examples of "cutting corners" by Ozgene led to the origin and further lack of acknowledgement of the *tdTomato*-defective mice; one, if the company had prioritized breeding of the *Axl-CreERT2-GFP-Rosa26-Wt* stock strain instead of leaving the breeding out of the *Flp* allele to the customer (us), the *tdTomato* deletion could have potentially been avoided (beyond the more straightforward way of avoiding this by due diligence); and two, by using only a wild-type genotyping assay to simultaneous test all of their transgenic mice (avoiding the extra effort of running individual positive-identification assays for each strain), it took much longer for our group to convince Ozgene that there had been an error. Thus, as a consequence all of the *tdTomato*-defective mice will likely have to be sacrificed since they do not provide any experimental value to our group (although perhaps they can be repurposed), completely negating any breeding efficiency that Ozgene provided and costing our group significant time delays and unnecessary labor. Nevertheless, the Axl lineage tracing strain when finally established will still provide valuable insights into our group's main research focus, and meanwhile we have gained experience with the methods required to analyze this strain in classical lineage tracing experiments and beyond.

6.2 Approaches to characterize mouse models

6.2.1 Whole mount mammary imaging

Although this was only a single experiment meant to evaluate the ability of the Olympus VS120 slider scanner to identify fluorescent populations of cells in 3D in the context of our new Axl-GFP mouse, some key takeaways were noted in the process. The EFI technique captures more detailed cell definitions from a broader depth range in a single image, which can be valuable when the number of positive cells is rare and thus more tissue needs to be surveyed than what is present in single tissue sections. However this approach did not enable the localization of positive cells to specific tissue compartments such as the mammary ducts. Additionally, the edge-finding algorithm used to select the Z-plane for autofocusing often showed a preference for stroma over mammary ducts, because this tissue compartment contains sparsely distritbuted cells connected by a web of adipocyte membranes that provides optimal objects for edge detection. A superior analysis could be performed by using virtual-

Z, another 3D imaging acquisition mode on the instrument, which saves the entire image at every Z-plane in the depth sampling range, allowing the user to viturally adjust the focus (Z) by scrolling through the stacked images in the output file. This option was not initially explored because the output file sizes are 1-2 orders of magnitude greater than a single EFI image, which is already ~1.5 GB. However, having this information could enable the 3D localization of positive cells by placing them in the same focal plane as the compartment of interest (mammary duct cells). Assuming this was possible, a better balance of DNA (Hoescht) staining intensity and GFP signal must be established, since the DNA stain was much brighter than the GFP in this experiment and likely masked the signal (through spectral emission spillover into the GFP channel) from the rare Axl-GFP+ basal cells in the nuclei-dense mammary eptihelia. This supports the assumption that the discrete GFP+ cells detected in this experiment were most likely macrophages, since these cells were most often found in the stroma and it is known that macrophages express high levels of TAMRs [26].

6.2.2 Fluorescent imaging of cryosections

These experiments were performed to profile GFP expression in tissues from the Axl knock-in strain, correlating this expression with known Axl+ cell types and our previous *in situ* Axl-staining images from the Axl-LacZ-HET mice to confirm Axl-GFP co-expression. This was indeed the case for both spleen and lung. Although the Axl-LacZ model already provided an adequate method for identifying Axl+ cells in tissue sections and flow cytometry, the Axl-GFP model provides a higher intensity signal which is much more convincing for publications, without the additional step of adding a β-gal substrate. However, two caveats to this fluorescent reporter system include the instability of the reporter signal, which necessitates the use of fresh or frozen samples, immediate processing, and protection from light, and the presence of autofluorescent artefacts in both imaging and cytometry applications.

6.2.3 Flow cytometry

This experiment was performed to gauge our ability to isolate GFP+ cells from *Axl-CreERT2-GFP* mice so that they can eventually be sorted and used in functional/organoid studies during lineage tracing experiments. Although this initial test was rudimentary in that it lacked additional markers for exclusion of other Axl+ cell types (Lin- staining panel: CD11b for monocytes, macrophages, and granulocytes; CD11c for most dendritic cells; CD45 for most hematopoietic cells; CD31 for endothelial cells), the primary goal was simply to identify and

quantify a distinct GFP+ population in organ-derived cell suspensions. These populations were indeed found in dissociated mammary and lung tissue, however some proportion of this population may be attributable to large autofluorescent chunks of cellular debris from dissociation, since many of the GFP+ events were in the upper size range of what could be considered a single cell (Fig 5.2.3). Ideally, a negative control (WT) mouse should be analyzed in parallel with the Axl-GFP mouse to observe if the GFP+ population is still present in GFP-dissociated cell suspensions. Additionally, the incorporation of a live/dead marker such as propium iodide (PI) could help identify some of the GFP+ events as cell debris. Gating threshold strategies and the appropriate choice of fluorescence tags for Lin- staining must be considered when both GFP and RFP will be used to sort Axl+ cells and their progeny.

6.3 IMC

Because IMC is such a novel technology, it has a very limited pool of expertise and literature available for new users. UiB acquired the first Hyperion in Scandinavia, and this project was the first usage of the system, therefore there was no infrastructure or guidance in place for how to go about developing a panel and analysing data, so the approach had to be carried out completely from scratch. A brief reflection on the progress made and the challenges encountered in this process is given below.

The greatest advantage of IMC over other imaging approaches is inarguably its unrivalled multiplexing capability. However, this comes with the challenge of testing and validating a panel of 40 antibodies. As the field grows, more pre-conjugated FFPE-compatible antibodies will become available, as well as more metals to expand the size of panels. Regardless of whether an antibody is conjugated in-house or pre-validated, it still must be titrated and visually assessed for staining quality in known sample types, which can be tedious and inconclusive. Although measuring cell intensity can be used as a surrogate quantitative approach to determine the ability of an antibody to distinguish cell populations, this is highly dependent on the quality of the cell segmentation, which is often inaccurate especially in early optimization experiments. This approach can be augmented and accelerated by testing the discriminative abilities of multiple antibodies simultaneously in round trip analyses, where successful identification of phenotypes using unsupervised clustering can be confirmed by mapping them back to the original sample image.

7. Future Perspectives

Axl MaSC lineage tracing study

When the *Axl-CreERT2-EGFP-Rosa26-Wt/TdTomato* is eventually established in our lab, our group will be ready and waiting to commence the mammary gland lineage tracing study described in this work. Although the dual-reporter lineage tracing system alone is likely sufficient to implicate Axl as a multipotent MaSC marker in homeostasis and/or remodeling (if our hypothesis is true) using conventional fluorescence-based approaches, this does not necessarily place Axl at the apex of the stem cell hierarchy nor fully elucidate its role in plasticity-induced dedifferentiation. Notably, a previous lineage tracing study demonstrated that ProCR+ basal cells produce both luminal and myoepithelial lineages during homeostasis and act as multipotent MaSCs, but at an insufficient rate to account for the entire cellular turnover in the mammary gland [71]. If this is indeed the case with Axl, then it is necessary to examine Axl+ cells and their progeny *in situ* with a higher level of informational context using IMC and under conditions that depart from normal physiology (such as inflammation and wound healing) which provide a stronger link to Axl signaling in the tumor microenvironment.

Combining transgenic mice with disease models

Both of the transgenic Axl-targeting models mentioned in this study can be further exploited by coupling them with disease models. In fact, this has already been done in our group; Axl-LacZ mice were crossed with a *Wnt1*-overexpressing strain that serves as a mammary tumorigenesis model by inducing dedifferentiation and expansion of the luminal cell compartment into stem-like pre-neoplastic progenitors [72]. Strikingly, the *Wnt1*-driven mammary tumor incidence was significantly reduced in Axl-null mice [51]. To unravel this phenomenon, creating a similar cross between this tumorigenesis model and the Axl-Cre lineage tracing strain would elegantly complement the initial study. Furthermore, Axl lineage tracing in other disease models such as bleomycin-induced pulmonary fibrosis and unilateral urethral obstruction-induced kidney fibrosis can validate the existing prognostic and therapeutic indications of Axl signaling in these diseases [73, 74].

8. References

1.   Dye, C., *After 2015: infectious diseases in a new era of health and development.* Philosophical Transactions of the Royal Society B: Biological Sciences, 2014. **369**(1645): p. 20130426.

2.   Weir, H.K., et al., *Peer Reviewed: Heart Disease and Cancer Deaths—Trends and Projections in the United States, 1969–2020.* Preventing chronic disease, 2016. **13**.

3.   Health, N.I.o.P. *Causes of Death, Norway.* [cited 2019 Aug 10]; Available from: http://statistikkbank.fhi.no/dar/.

4.   Bray, F., et al., *Global cancer statistics 2018: GLOBOCAN estimates of incidence and mortality worldwide for 36 cancers in 185 countries.* CA: A Cancer Journal for Clinicians, 2018. **68**(6): p. 394-424.

5.   Ferlay J, E.M., Lam F, Colombet M, Mery L, Piñeros M, et al. *Global Cancer Observatory: Cancer Today.* 2018 [cited 2018; Available from: https://gco.iarc.fr/today.

6.   Tomasetti, C. and B. Vogelstein, *Variation in cancer risk among tissues can be explained by the number of stem cell divisions.* Science, 2015. **347**(6217): p. 78-81.

7.   Tomasetti, C., L. Li, and B. Vogelstein, *Stem cell divisions, somatic mutations, cancer etiology, and cancer prevention.* Science, 2017. **355**(6331): p. 1330-1334.

8.   Hanahan, D. and R.A. Weinberg, *The Hallmarks of Cancer.* Cell, 2000. **100**(1): p. 57-70.

9.   Hanahan, D. and Robert, *Hallmarks of Cancer: The Next Generation.* Cell, 2011. **144**(5): p. 646-674.

10. Dan Anderson, K.A. *Understanding Cancer.* Cell Biology and Cancer: Teacher's Guide 1999 [cited 2019 Aug. 17].

11. Alsibai, K.D. and D. Meseure, *Significance of Tumor Microenvironment Scoring and Immune Biomarkers in Patient Stratification and Cancer Outcomes.* Histopathology: An Update, 2018: p. 11.

12. *About surgery.* Apr. 6 2016 [cited 2019 17 Aug.]; Available from: https://www.cancerresearchuk.org/about-cancer/cancer-in-general/treatment/surgery/about.

13. Curie, P. and M. Curie, *Sur la radioactivité provoquée par les rayons de Becquerel.* 1899: Gauthier-Villars.

14. Barker, H.E., et al., *The tumour microenvironment after radiotherapy: mechanisms of resistance and recurrence.* Nature Reviews Cancer, 2015. **15**: p. 409.

15. Brookes, P., *The early history of the biological alkylating agents, 1918–1968.* Mutation Research/Fundamental and Molecular Mechanisms of Mutagenesis, 1990. **233**(1-2): p. 3-14.

16. Falzone, L., S. Salomone, and M. Libra, *Evolution of Cancer Pharmacological Treatments at the Turn of the Third Millennium.* Frontiers in Pharmacology, 2018. **9**.

17. Yan, L., N. Rosen, and C. Arteaga, *Targeted cancer therapies.* Chinese journal of cancer, 2011. **30**(1): p. 1-4.
18. Schlessinger, J. and A. Ullrich, *Growth factor signaling by receptor tyrosine kinases.* Neuron, 1992. **9**(3): p. 383-391.
19. Pardoll, D.M., *The blockade of immune checkpoints in cancer immunotherapy.* Nature Reviews Cancer, 2012. **12**(4): p. 252-264.
20. Hargadon, K.M., C.E. Johnson, and C.J. Williams, *Immune checkpoint blockade therapy for cancer: An overview of FDA-approved immune checkpoint inhibitors.* International Immunopharmacology, 2018. **62**: p. 29-39.
21. Galon, J. and D. Bruni, *Approaches to treat immune hot, altered and cold tumours with combination immunotherapies.* Nature Reviews Drug Discovery, 2019. **18**(3): p. 197-218.
22. Lai, C. and G. Lemke, *An extended family of protein-tyrosine kinase genes differentially expressed in the vertebrate nervous system.* 1991. **6**(5): p. 691-704.
23. Geng, K., et al., *Requirement of Gamma-Carboxyglutamic Acid Modification and Phosphatidylserine Binding for the Activation of Tyro3, Axl, and Mertk Receptors by Growth Arrest-Specific 6.* Front Immunol, 2017. **8**: p. 1521.
24. Meyer, A.S., A.J. Zweemer, and D.A. Lauffenburger, *The AXL Receptor is a Sensor of Ligand Spatial Heterogeneity.* Cell Syst, 2015. **1**(1): p. 25-36.
25. Mayer, B.J. and J. Yu, *Protein Clusters in Phosphotyrosine Signal Transduction.* Journal of Molecular Biology, 2018. **430**(22): p. 4547-4556.
26. Lemke, G., *Phosphatidylserine Is the Signal for TAM Receptors and Their Ligands.* Trends Biochem Sci, 2017. **42**(9): p. 738-748.
27. Graham, D.K., et al., *The TAM family: phosphatidylserine sensing receptor tyrosine kinases gone awry in cancer.* Nat Rev Cancer, 2014. **14**(12): p. 769-85.
28. Tulchinsky, E., et al., *EMT: A mechanism for escape from EGFR-targeted therapy in lung cancer.* Biochim Biophys Acta Rev Cancer, 2019. **1871**(1): p. 29-39.
29. Zhao, G.J., et al., *Growth Arrest-Specific 6 Enhances the Suppressive Function of CD4(+)CD25(+) Regulatory T Cells Mainly through Axl Receptor.* Mediators Inflamm, 2017. **2017**: p. 6848430.
30. Lemke, G. and C.V. Rothlin, *Immunobiology of the TAM receptors.* Nat Rev Immunol, 2008. **8**(5): p. 327-36.
31. Rankin, E. and A. Giaccia, *The Receptor Tyrosine Kinase AXL in Cancer Progression.* Cancers, 2016. **8**(11): p. 103.
32. *Chemotherapy With Nab-paclitaxel/Germcitabine/Cisplatin +/- BGB324 With Pancreatic Cancer.* Available from: https://ClinicalTrials.gov/show/NCT03649321.
33. *BGB324 in Combination With Pembrolizumab or Dabrafenib/Trametinib in Metastatic Melanoma.* Available from: https://ClinicalTrials.gov/show/NCT02872259.
34. *A Study of BGB324 in Combination With Erlotinib in Patients With Non-Small Cell Lung Cancer.* Available from: https://ClinicalTrials.gov/show/NCT02424617.

35. *Bemcentinib (BGB324) in Combination With Pembrolizumab in Patients With Advanced NSCLC*. Available from: https://ClinicalTrials.gov/show/NCT03184571.

36. *A Phase Ib/II Multicenter Open-label Study of BGB324 in Patients With AML or MDS*. Available from: https://ClinicalTrials.gov/show/NCT02488408.

37. *Bemcentinib (BGB324) in Combination With Pembrolizumab in Patients With TNBC*. Available from: https://ClinicalTrials.gov/show/NCT03184558.

38. *Trial of Dose Escalated BGB324 in Previously Treated Non-small Cell Lung Cancer*. Available from: https://ClinicalTrials.gov/show/NCT02922777.

39. *AXL Inhibitor BGB324 in Treating Participants With Recurrent Glioblastoma Undergoing Surgery*. Available from: https://ClinicalTrials.gov/show/NCT03965494.

40. Dreesen, O. and A.H. Brivanlou, *Signaling Pathways in Cancer and Embryonic Stem Cells.* 2007. **3**(1): p. 7-17.

41. Paccez, J.D., et al., *The receptor tyrosine kinase Axl in cancer: biological functions and therapeutic implications.* Int J Cancer, 2014. **134**(5): p. 1024-33.

42. Levin, P.A., et al., *Axl Receptor Axis: A New Therapeutic Target in Lung Cancer.* J Thorac Oncol, 2016. **11**(8): p. 1357-1362.

43. Myers, S.H., V.G. Brunton, and A. Unciti-Broceta, *AXL Inhibitors in Cancer: A Medicinal Chemistry Perspective.* J Med Chem, 2016. **59**(8): p. 3593-608.

44. Waddington, C., *The strategy of the genes: a discussion of some aspects of theoretical biology. 1957*. London: Allen & Unwin.

45. Clevers, H. and F.M. Watt, *Defining adult stem cells by function, not by phenotype.* Annual review of biochemistry, 2018. **87**: p. 1015-1027.

46. Ben-Batalla, I., et al., *Axl, a prognostic and therapeutic target in acute myeloid leukemia mediates paracrine crosstalk of leukemia cells with bone marrow stroma.* Blood, 2013. **122**(14): p. 2443-52.

47. Buczacki, S.J., et al., *Intestinal label-retaining cells are secretory precursors expressing Lgr5.* Nature, 2013. **495**(7439): p. 65.

48. Muñoz-Cánoves, P. and M. Huch, *Definitions for adult stem cells debated.* Nature, 2018. **563**(7731): p. 328-329.

49. Taddei, I., et al., *β1 Integrin deletion from the basal compartment of the mammary epithelium affects stem cells.* Nature Cell Biology, 2008. **10**(6): p. 716-722.

50. Van Keymeulen, A., et al., *Distinct stem cells contribute to mammary gland development and maintenance.* Nature, 2011. **479**(7372): p. 189-193.

51. Katarzyna Wnuk-Lipinska, A.S.T.E., Crina Tiron, Fanny A. Vater, Sebastien Bougnaud Masaru Miyano Pouda Panahandeh, Sura M. Aziz, Silje Nord, Lars Herfindal, Gro Gausdal, Martha R. Stampfer, Therese Sørlie, Rolf A. Brekken, Oddbjørn Straume, Nils Halberg, Lars A. Akslen, Mark A. LaBarge, James B. Lorens, *Axl is required for phenotypic plasticity of normal and neoplastic breast epithelial stem cells*, U.o. Bergen, Editor.: In Review.

52. Blanpain, C. and E. Fuchs, *Stem cell plasticity. Plasticity of epithelial stem cells in tissue regeneration.* Science, 2014. **344**(6189): p. 1242281.

53. Mills, K.L., et al., *Gas6 is dispensable for pubertal mammary gland development.* PLoS One, 2018. **13**(12): p. e0208550.

54. Tata, P.R., et al., *Dedifferentiation of committed epithelial cells into stem cells in vivo.* Nature, 2013. **503**(7475): p. 218.

55. Jain, R., et al., *Plasticity of Hopx+ type I alveolar cells to regenerate type II cells in the lung.* Nature communications, 2015. **6**: p. 6727.

56. Maria L. Lotsberg, K.W.-L., Stéphane Terry, Tuan Zea Tan, Laura Trachsel-Moncho, Gro V. Røsland, Monica Hellesøy, Austin Rayford, Kirstine Jacobsen, Henrik J. Ditzel, Olav K. Vintermyr, Trever G. Bivona, John Minna, Rolf A. Brekken, Bruce Baguley, David Micklem, Lars A. Akslen, Gro Gausdal, Anne Simonsen, Jean Paul Thiery, Salem Chouaib, James B. Lorens, Agnete S.T. Engelsen, *AXL targeting abrogates autophagic flux and induces immunogenic cell death in drug resistant cancer cells* EMBO, 2019. **In review**.

57. Koentgen, F., et al., *Exclusive transmission of the embryonic stem cell-derived genome through the mouse germline.* genesis, 2016. **54**(6): p. 326-333.

58. Seldin, L., A. Le Guelte, and I.G. Macara, *Epithelial plasticity in the mammary gland.* Curr Opin Cell Biol, 2017. **49**: p. 59-63.

59. Mulvihill, D. *Other Plasmid Components*. [cited 2019 Aug. 15]; Available from: https://www.oxfordgenetics.com/SiteContent/TeamResources/Other_Plasmid_Components.

60. Wang, Y., et al., *2A self-cleaving peptide-based multi-gene expression system in the silkworm Bombyx mori.* Scientific reports, 2015. **5**: p. 16273.

61. Zhou, J., et al., *Stem Cells and Cellular Origins of Mammary Gland: Updates in Rationale, Controversies, and Cancer Relevance.* Stem Cells Int, 2019. **2019**: p. 4247168.

62. Giesen, C., et al., *Highly multiplexed imaging of tumor tissues with subcellular resolution by mass cytometry.* Nature Methods, 2014. **11**(4): p. 417-422.

63. Prager, B.C., et al., *Cancer Stem Cells: The Architects of the Tumor Ecosystem.* Cell Stem Cell, 2019. **24**(1): p. 41-53.

64. Meyers, E.N., M. Lewandoski, and G.R. Martin, *An Fgf8 mutant allelic series generated by Cre-and Flp-mediated recombination.* Nature genetics, 1998. **18**(2): p. 136.

65. Bankhead, P., et al., *QuPath: Open source software for digital pathology image analysis.* Scientific Reports, 2017. **7**(1): p. 16878.

66. Ran, F.A., et al., *Genome engineering using the CRISPR-Cas9 system.* Nature Protocols, 2013. **8**(11): p. 2281-2308.

67. Keirnan, J., in *Histological and Histochemical Methods: Theory and Practice*. 2008, Scion: UK.

68. Schapiro, D., et al., *histoCAT: analysis of cell phenotypes and interactions in multiplex image cytometry data.* Nature Methods, 2017. **14**(9): p. 873-876.

69. *Lung Toxicology Problem Set*. The Biology Project 1997 [cited 2019 Aug 15]; Available from: http://www.biology.arizona.edu/chh/problem_sets/lung_toxicology/02t.html.

70. Boateng, K., B. Weyori, and D. Sanka Laar, *Improving the Effectiveness of the Median Filter.* International Journal of Electronics and Communication Engineering, 2012. **5**: p. 85-97.

71.   Wuidart, A., et al., *Quantitative lineage tracing strategies to resolve multipotency in tissue-specific stem cells.* 2016. **30**(11): p. 1261-1277.

72.   Vaillant, F., et al., *The mammary progenitor marker CD61/beta3 integrin identifies cancer stem cells in mouse models of mammary tumorigenesis.* Cancer Res, 2008. **68**(19): p. 7711-7.

73.   Espindola, M.S., et al., *Targeting of TAM Receptors Ameliorates Fibrotic Mechanisms in Idiopathic Pulmonary Fibrosis.* Am J Respir Crit Care Med, 2018. **197**(11): p. 1443-1456.

74.   Landolt, L., et al., *AXL targeting reduces fibrosis development in experimental unilateral ureteral obstruction.* Physiological reports, 2019. **7**(10): p. e14091-e14091.

9. Appendix: Thumbnail images from IMC experiments

For environmental purposes, the thumbnail images have been moved to the following online folder: [Thumbnail Images from IMC Experiments](#)